NEW TECHNOLOGIES FOR SPECTROSCOPY OF MATERIALS UNDER STATIC AND SHOCK COMPRESSION

BY

KATHRYN E. BROWN

DISSERTATION

Submitted in partial fulfillment of the requirements
for the degree of Doctor of Philosophy in Chemistry
in the Graduate College of the
University of Illinois at Urbana-Champaign, 2012

Urbana, Illinois

Doctoral Committee:

Professor Dana D. Dlott, Chair
Professor Martin Gruebele
Professor Gregory S. Girolami
Professor Catherine J. Murphy

Abstract

Two novel techniques for spectroscopically studying materials under static and shock compression are described. The first known spectra of self-assembled organic monolayers under static pressure up to 10 GPa were obtained by the novel combination of surface-enhanced Raman scattering spectroscopy with diamond anvil cell technology. The samples used were benzenethiol (BT) and benzene methane thiol (BMT) adsorbed onto photonic substrates composed of silver films over polystyrene nanospheres. Results indicated that the thiols were mobile, not fixed, on the silver surface. Also reported is an application of this technique in which the high pressure vibrational response of an energetic material simulant is characterized. Second, a technique to simultaneously monitor the global and local responses of shocked materials with mesoscale inhomogeneities is discussed, using a dye (rhodamine 640) embedded in a polymer matrix (poly(methyl-methacrylate)) shocked to 15 GPa as a model system. The dye/polymer thin film was shocked using simplified laser-driven flyer plates, also described here. The local dynamics were probed using fluorescence emission of the dye, and the global dynamics were probed with a photon Doppler velocimeter. The results indicated that within the 8-15 ns duration of the imparted shock, the polymer was not able to fully compress and reach its highest density, which is implied by the leveling off of the dye fluorescence redshift with applied pressure over 7 GPa.

Acknowledgments

The research presented in this work was supported by the US Army Research Office under award W911NF-10-1-0072, the US Air Force Office of Scientific Research under award FA9550-09-1-0163, the Defense Threat Reduction Agency under award HDTRA1-12-1-0011, the Office of Naval Research award N00014-11-1-0418, and the Stewardship Sciences Academic Alliance Program from the Carnegie-DOE Alliance Center, under grant number DOE CIW 4-3253-13. I especially want to acknowledge CDAC, as they not only funded my research and time here, but through annual reviews and conferences I attended, I have been able to present my work, talk to amazing scientists in the high pressure field, and make friends.

Beyond the funding, I first and foremost wish to thank my graduate advisor, Dana Dlott. He pushed me to learn and figure out how to make things work, which has been invaluable experience. I also want to thank the Dlott research group, who through the years have been great help in the lab and great fun outside.

Finally, I want to acknowledge my friends and family, especially my husband, Tjett. Thank you for your patience, your willingness to move to the middle of nowhere Illinois and now to the middle of nowhere New Mexico, and for your love and support. Grad school would have been much different and much worse without you to come home to. I love you.

Table of Contents

Chapter 1: Introduction[1]

This thesis will be broken up into two distinct but related sections, both covering sets of experiments that I started in this research group. The first section (chapters 2 and 3) is comprised of work that I did examining the vibrational response of statically-compressed self-assembled monolayers. The second portion (chapters 4 and 5) covers the experimental design and results of a novel technique for probing the local environments of shocked inhomogenous materials.

1.1 Static Pressure

I combined surface-enhanced Raman scattering with diamond anvil cell technology to obtain the first known spectra of self-assembled organic monolayers under high pressures up to 10 GPa. This technology could be useful for developing a fundamental molecular-level understanding of metal-lubricant[1,2,3] interactions and spontaneous self-assembly processes.[4,5] Additionally, this technique can be used to study energetic materials simulants monolayers, *i.e.* monolayers containing functional groups found in energetic materials. This capability was demonstrated by studying a monolayer with nitro functional groups under pressure.

High, hydrostatic pressure (GPa to Mbar, where 1 GPa=10^4 bar and 1 Mbar=100 GPa) research spans several areas of science, including chemistry, physics and geology. Since its inception in the early 1900s by P.W. Bridgman, the field has greatly expanded and there are now several techniques and research teams studying materials under high pressure.[6] High pressure research is often focused on either synthesizing novel compounds using high pressure, such as superhard materials,[7] semiconductors,[8] polymeric nitrogen[9,10] or the elusive metallic hydrogen[11,12,13] for energy storage, or identifying high pressure phases and phase change

[1] Portions of this chapter have previously been published in the following article: Brown, K. E. and Dlott, D. D. *J. Phys. Chem. C* **2009,** *113,* 5751–5757.

boundaries of minerals or other materials, often relevant to planetary interiors.[14,15,16] Another area of high pressure research is investigating material properties by studying the hydrostatic compression of organic materials, including simple molecules (*e.g.* methane[17]), polymers[18] and energetic materials.[19,20,21,22] High pressure techniques most commonly include diamond anvil cells (described in detail later in this chapter and in chapter 2) or multi-anvil presses, and characterization spans several techniques and scales, from vibrational or fluorescence spectroscopy in a small laboratory setting, to x-ray diffraction at a synchrotron beam source. Recent advances in growing chemical vapor deposition diamonds have also allowed researchers to embed filaments in the diamonds themselves (deemed "designer diamonds") for *in situ* resistivity[23] and conductivity measurements.[24]

Self-Assembled Monolayers

Self-assembly of monolayers exploits a strong preferential affinity of a molecule or atom on a substrate for one functional group of another molecule. One of the most common types of self-assembled monolayers (SAMs) is a thiol bonded to a silver or gold substrate through the sulfur atom.[4]

The three SAMs that I worked on were benzenethiol (BT), benzene methanethiol (BMT), and 4-nitro benzenethiol (NBT). All three bind to Ag or Au surfaces in the form of thiolates, either Ph-S-Ag for BT, Ph-CH_2-S-Ag for BMT, or NO_2-Ph-S-Ag for NBT (Ph = phenyl), as determined by a number of methods[4,25] including the disappearance of the characteristic SH-stretching transitions ν_{SH} in the SERS spectrum[26]. The structures of BT and BMT molecules believed to be adopted when these molecules form SAMs on noble metal surfaces at ambient pressure[25,27,28] are depicted in Fig. 1.1, where the bond angles are those expected for sp^3 sulfur hybridization. It is reasonable to assume that NBT would adopt a structure similar to that of BT.

It is believed that the sulfur atoms are located at the 3-fold hollow sites of the (111) surfaces,[27] although there is still quite a bit of discussion about other motifs.[29] When sulfur has the most common and lowest-energy sp^3 hybridization, the BT phenyl groups will be upright but tilted at an ~104° angle from the surface normal.[27] The BMT phenyl groups will be upright and nearly parallel to the surface normal (Fig. 1.1).[27] Raman studies of BT and BMT SAMs provide strong evidence that the phenyl moieties are upright such that their π-electrons are not strongly perturbed by interactions with the metal surface.[25]

When permitted by the constraints imposed by the anchoring bonds, the phenyl groups try to adopt the lower-energy herringbone lattice consisting of "T-shaped" phenyl dimers.[27] The formation of a close-packed lower-energy herringbone structure is more difficult for BT due to the phenyl tilt unless the molecules adopt the higher-energy sp hybridization form which has not been observed.[27] For this reason the BT SAM is lower-density and possibly less ordered than the BMT SAM. On Au, for instance, the surface area per molecule is 20.5 $Å^2$ for BMT and 37.8 $Å^2$ for BT.[30]

When BT and BMT are adsorbed on a noble-metal surface, most of the vibrations show a negligible frequency shift relative to the solid but a few vibrations nevertheless shift by up to 25 cm^{-1}. These shifts have been explained as arising primarily from a mass effect resulting from binding to a heavy Ag atom. The similarity of the spectrum of the Ag-S-Ph salt to a BT SAM on an Ag surface supports this interpretation.[26,31]

SAMs under pressure (albeit pressures much lower than used here) have been previously studied by mechanical, optomechanical, electrochemical and spectroscopic techniques. Mechanical methods included atomic force microscopy (AFM)[32,33,34] and frictional force microscopy (FFM)[35,36]. Alkanethiol SAMs with even numbers of carbon atoms were compressed

to static pressures of <1 GPa using an AFM tip. At a critical load of ~0.2 GPa, the SAM surface became disrupted.[37] With even greater strain, an AFM tip was actually able to scratch the metal surface, indicating that SAM molecules could be uprooted and driven out of the compressed region.[37] The electrochemical charge transfer processes of SAMs were studied at pressures up to 0.6 GPa.[38] Infrared spectroscopy was used to study Langmuir-Blodget films (long-chain molecules floating on water) as a faction of compression in the plane.[39] Vibrational sum-frequency generation spectroscopy (SFG) was used to study alkane SAMs under static uniaxial pressure produced by a transparent anvil, and under dynamic pressure created by laser-driven shock waves. SFG is sensitive only to the CH-stretch transitions of the terminal methyl groups, and can be used to determine the angle of methyl tilting. The resonant SFG intensity of the terminal methyl groups decreased when SAMs were compressed above 10 MPa [40,41,42,43,44]. This SFG signal returned elastically when the pressure was released. In ultrafast shock compression experiments,[45,46,47,48] SFG was used to study the methyl tilt of alkane SAMs subjected to 4 GPa laser-driven shock waves. When the shock arrived, the SFG signal decreased dramatically within a few picoseconds. The signal disappearance was attributed to the formation of *gauche* defects having large methyl tilt angles.[46,47]

One of the biggest challenges associated with studying vibrational spectra of monolayers is the simple fact that, by definition, there are much fewer molecules than there are in a bulk material. This challenge can be overcome using surface-specific techniques such as sum frequency generation (SFG) or surface-enhanced Raman scattering spectroscopy (SERS).

Surface-Enhanced Raman Scattering Spectroscopy

One of the major mechanisms by which SERS enhances the Raman signal is by electromagnetic (EM) enhancement.[49] Typical SERS substrates consist of nano-textured metallic

surfaces to which a molecule is adsorbed, or, in the case of SAMs, chemisorbed. The sample type that we use is a silver film-over-nanospheres (AgFON), developed by the van Duyne group at Northwestern University, that consists of a thin layer of silver deposited over a layer of nanospheres.[50,51] Incident laser light interacts with the particles that are much smaller than the wavelength of light, leading to a localized, oscillating surface plasmon with a certain frequency, termed the localized surface plasmon resonance (LSPR). The excited plasmons, which in the case of an AgFON substrate have amplitudes ~30 times greater than the incident electric field, enhance the electric field of the incident laser and also the Stokes SERS scattering.[52]

The LSPR can be tuned based on the shape and size of the nanoparticles. The enhancement is greatest when the plasmon resonance is tuned to overlap the laser frequency and the Raman-shifted light.[53] It is worth noting that in the example of the AgFON, the "particle size" does not refer to the actual diameter of the nanosphere, but to the nano-textured feature that is responsible for the greatest enhancement, or "hot spot". In an AgFON substrate, the "hot spots" are believed to be located in the crevices between nanospheres, and are responsible for 24% of the overall enhancement, despite only accounting for 63 of 1,000,000 molecules.[54] The SERS enhancement for an AgFON system tends to be on the order of 10^6. Practically, this means that the SERS spectrum from a single, 1 nm thick monolayer can be equivalent in intensity to a Raman spectrum of the bulk material that is 1 mm thick.

Diamond Anvil Cell

Diamond anvil cells are perhaps the most commonly used tools to study materials under high, quasi-hydrostatic pressure (between 1-300 GPa). A diamond anvil cell consists of two opposing diamonds that exert force on a sample surrounded by a pressure-transmitting medium (PTM) within the sample chamber of a gasket (*c.f.* Figure 3.1).[55] Pressure-transmitting media

provide a quasi-hydrostatic environment as they do not support shear stresses.[56,57] A quasi-hydrostatic environment is necessary to minimize the existence of a pressure gradient across the sample. Typical media include a methanol-ethanol-water mixture, argon or other noble gases, or salts such as NaCl. Pressure calibrants, the most common of which is ruby chips, are placed inside the sample chamber. The wavelength of the ruby fluorescence R_1 line is related to pressure by the equation:[58]

$$P = \frac{A}{B}\left\{\left[1 + \left(\frac{\Delta\lambda}{\lambda_0}\right)\right]^B - 1\right\} \quad (1)$$

where P is the pressure in Mbar, λ is the wavelength of the ruby R_1 line, A=19.04 Mbar, B=7.665. An example of the ruby fluorescence as it shifts with increasing pressure is shown on Fig. 1.2.

The highest quasi-hydrostatic pressure attainable in any individual DAC is dependent upon a combination of diamond type, culet size, gasket material, PTM, and cell type used. The culet is the flat face of the diamond that is in contact with the PTM; generally, the smaller the culet the higher pressure can be applied without the diamond breaking. For ultra-high pressure experiments (Mbar), beveled diamonds have been used successfully to sharpen the pressure gradient on the solid gasket.[59] Additionally, higher pressures are obtained with harder gaskets, such as stainless steel or beryllium, beryllium having the added advantage of being transparent to x-rays for x-ray diffraction experiments.[60] Conversely, a larger culet lowers the attainable pressure, but allows for a larger sample size. As softer gasket will also lower the attainable pressure, but the pressure can be applied in smaller increments.

1.2 Shock Pressure

When a material is shocked, it is irreversibly and adiabatically compressed.[61] There are several techniques for attaining shock compression of a material, including *via* explosives, lasers, or mechanical impactors. Like static compression, shock compression of condensed matter is an expansive field with a multitude of applications,[62] with shock initiation and detonation measurements at the forefront of the field. One common type of energetic materials is plastic bonded explosives (PBX) that contain molecular explosive crystals and a polymer binder. Probing the *in situ* local environments of shocked structured materials such as PBX can lend insight into their shock initiation and detonation mechanisms, as well as aid in future PBX design.

I designed a method to simultaneously probe the local and global environments of shocked inhomogeneous materials. As a model system I used a thin film of poly(methyl methacrylate) (PMMA) with embedded rhodamine dye aggregates. Global dynamics of the polymer were measured with photonic Doppler velocimetry (PDV), a type of Mach-Zehnder displacement interferometer. Local dynamics were spectroscopically interrogated by time-resolved fluorescence emission of the embedded dye molecules.

Shock Characterization: Principal Hugoniot

A shock can be characterized by two variables, the shock velocity (U_s) and the particle, or material, velocity (U_p). The shock velocity is the velocity of the shock wave of the material being impacted.[63] The particle velocity is the velocity of the face of the impacted material. In the case that the impactor and the impacted object are the same material, the particle velocity will be half of the velocity of the impactor. If they are not the same material, the particle velocity depends on how fast the impactor is moving as well as the impedance of each material. The relation between

several points of U_s vs. U_p is that material's principal Hugoniot. It is nominally linear, with the form $U_s=mU_p+b$. Using the following Rankine-Hugoniot relations, derived from conservation of mass, momentum and energy, respectively, the shock pressure, volume, density, and energy can be calculated:

$$\frac{V}{V_0} = \frac{(U_s - U_p)}{U_s} \tag{2}$$

$$P - P_0 = \rho_0 U_s U_p \tag{3}$$

$$E - E_0 = \frac{1}{2}(P - P_0)(V_0 - V) \tag{4}$$

where U_s is the shock velocity, P is pressure, V is volume, ρ is density, E is energy and the initial states of the material at rest are indicated by subscript zeros.[63] The principal Hugoniot can be described as any combination of these parameters for a material. It is important to note that the Hugoniot is not a path that a shocked sample takes, but a curve consisting all of the possible states the material can be shocked to from its initial state.[62]

Laser driven flyer plates

An in-depth treatment of laser-driven flyer plates is given in chapter 4. Briefly, one popular type of mechanical impactor is the laser-driven flyer plate. A high power laser is incident onto a metal foil. The laser ablates a portion of the foil, creates a plasma, and launches a foil disc (the "flyer plate") forward, and the flyer plate impacts a material of interest. Generally, thin (0.5-10 μm thick) flyers are used to impart short (~1 ns), high energy shocks to initiate energetic materials.[64,65,66,67] Thick (0.1-1 mm) flyers are often used in equation of state measurements,[68] as their shock durations are up to 300 ns. In our research group, we wanted the capability to launch fast flyer plates that could initiate energetic materials, but also were thick enough to have several ns shock durations.

1.3 Complementarity of static and shock pressure experiments

Static and shock pressure experiments are frequently used to complement one another, especially in the field of energetic and reactive materials research. For example, pentaerythritol tetranitrate (PETN) is known to have different shock sensitivities on different crystal axes. Static high pressure experiments on PETN have elucidated available high pressure conformers of the crystal, which may lend insight to its shock-initiation mechanism.[69] Formic acid, whose behavior under static high pressures[70] indicated that it may be linked to origins of life, was recently studied under shock compression[71] to try to further characterize its high pressure polymerization behaviors. As I describe in chapter 5, the static high pressure response is useful as a point of comparison to shock experiments.

1.4 Figures

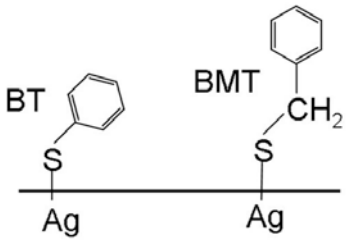

Figure 1.1: Expected conformations for benzenethiolate (BT) and benzenemethlythiolate (BMT) molecules adsorbed on Ag(111).

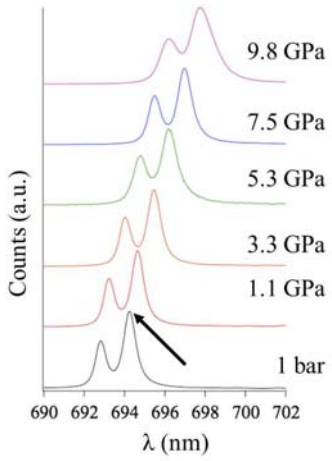

Figure 1.2: Ruby fluorescence at increasing pressures in a DAC. Arrow indicates ruby R1 peak.

1.5 References

(1) Mikulski, P. T. and Harrison, J. A. *J. Am. Chem. Soc.,* **2002,** *123,* 6873.

(2) Brewer, N. J.; Foster, T. T.; Leggett, G. J.; Alexander, M. R.; McAlpine, E. *J. Phys. Chem. B* **2004,** *108,* 4723.

(3) Houston, J. E.; Doelling, C. M.; Vanderlick, T. K.; Hu, Y.; Scoles, G.; Wenzl, I.; Lee, T. R. *Langmuir,* **2005,** *21,* 3926.

(4) Schreiber, F. *Prog. Surf. Sci.* **2000**, *65*, 151.

(5) Tao, Y.-T.; Wu, C.-C.; Eu, J.-Y.; Lin, W.-L.; Wu, J.-C.; Chen, C. *Langmuir* **1997,** *13,* 4018.

(6) Hemley, R. J. *High Press. Res.* **2010,** *30,* 581.

(7) Solozhenko, V. L. and Gregoryanz, E. *Mat. Today,* **2005,** *8,* 44.

(8) Sorb, Y. A.; Subramanian, N.; Ravindran, T. R.; Sahu, P. Ch. *AIP Conf. Proc.: Solid State Phys.-2010,* **2011,** *1349,* 1305.

(9) Eremets, M. I.; Gavriliuk, A. G.; Trojan, I. A. *Appl. Phys. Lett,* **2007,** *90,* 171904.

(10) Trojan, I. A.; Eremets, M. I.; Medvedev, S. A.; Gavriliuk, A. G.; Prakapenka, V. B. *Appl. Phys. Lett,* **2008,** *93,* 091907.

(11) Zha, C.-S.; Liu, Z.; Hemley, R. J. *Phys. Rev. Lett.* **2012,** *108,* 146402.

(12) Lebègue, S.; Araujo, C. M.; Kim, D. Y. *Proc. Nat. Acad. Sci.* **2012,** *109,* 9766.

(13) Mao, H.-K. and Hemley, R. J. *Rev. Modern Phys.* **1994,** *66,* 671.

(14) Machida, S-I.; Hirai, H.; Kawamura, T.; Yamamoto, Y.; Yagi, T. *Phys. Earth Planet. Int.* **2006,** *155,* 170.

(15) Prescher, C.; Dubrovinsky, L.; McCammon, C.; Glazyrin, K.; Nakajima, Y.; Kantor, A.; Merlini, M.; Hanfland, M. *Phys. Rev. B* **2012,** *85,* 140402.

(16) Mao, Z.; Armentrout, M.; Rainey, E.; Manning, C. E.; Dera, P.; Prakapenka, V. B.; Kavner, A. *Geophys. Rev. Lett.* **2011,** *38,* L22303.

(17) Chen, J.-Y. and Yoo, C.-S. *J. Chem. Phys.* **2012,** *136,* 114513.

(18) Dreger, Z. A.; Zhou, J.; Dang, N. C.; Gupta, Y. M. *J. Appl. Phys.* **2011,** *109,* 083507.

(19) Stevens, L. L.; Velisavljevic, N.; Hooks, D. E.; Dattelbaum, D. M. *Propellants, Explosives, Pyrotech.* **2008,** *33,* 286.

(20) Glascoe, E. A.; Zaug, J. M.; Burnham, A. K. *J. Phys. Chem. A* **2009,** *113,* 13548.

(21) Zheng, X.; Zhao, J.; Tan, D.; Liu, C.; Song, Y.; Yang, Y. *Propellants, Explosives, Pyrotech.* **2011,** *36,* 22.

(22) Gruzdkov, Y. A.; Dreger, Z. A.; Guptta, Y. M. *J. Phys. Chem. A* **2004,** *108,* 6216.

(23) Hamlin, J. J.; Jeffries, J. R.; Samudrala, G.; Vohra, Y. K.; Weir, S. T.; Zocco, D. A.; Maple, M. B. *Phys. Rev. B – Cond. Matt. Mat. Phys.* **2011,** *84,* 033101.

(24) Velisavljevic, N.; Vohra, Y. K.; Weir, S. T. *High Pressure Res.* **2005,** *25,* 137.

(25) Szafranski, C. A.; Tanner, W.; Laibinis, P.; Garrell, R. L. *Langmuir* **1998**, *14*, 3570.

(26) Joo, S.-W.; Kim, Y.-S. *Colloids and Surfaces A: Physicochem. Eng. Aspects* **2004**, *234*, 117.

(27) Jung, H. H.; Won, Y. D.; Shin, S.; Kim, K. *Langmuir* **1999**, *15*, 1147.

(28) Wan, L.-J.; Terashima, M.; Noda, H.; Osawa, M. *J. Phys. Chem. B* **2000**, *104*, 3563.

(29) Cossaro, A.; Mazzarello, R.; Rousseau, R.; Casalis, L.; Verdine, A.; Kohlmeyer, A.; Floreano, L.; Scandolo, S.; Morgante, A.; Klein, M. L.; Scoles, G. *Science* **2008**, *321*, 943.

(30) Tao, Y.-T.; Wu, C.-C.; Eu, J.-Y.; Lin, W.-L.; Wu, J.-C.; Chen, C. *Langmuir* **1997**, *13*, 4018.

(31) Joo, T. H.; Kim, M. S.; Kim, K. *J. Raman. Spectrosc.* **1987**, *18*, 57.

(32) Salmeron, M.; Neubauer, G.; Folch, A.; Tomitori, M.; Ogletree, D. F.; Sautet, P. *Langmuir* **1993**, *9*, 3600.

(33) Barrena, E.; Ocal, C.; Salmeron, M. *Journal of Chemical Physics* **2000**, *113*, 2413.

(34) Lee, S.; Puck, A.; Graupe, M.; Colorado, R., Jr.; Shon, Y.-S.; Lee, T. R.; Perry, S. S. *Langmuir* **2001**, *17*, 7364.

(35) Wong, S.-S.; Takano, H.; Porter, M. D. *Anal. Chem.* **1998**, *70*, 5209.

(36) Salmeron, M. *Tribol. Lett.* **2001**, *10*, 69.

(37) Carpick, R. W.; Salmeron, M. *Chem. Rev.* **1997**, *97*, 1163.

(38) Cruañes, M. T.; Drickamer, H. G.; Faulkner, L. R. *Langmuir* **1995**, *11*, 4089.

(39) Elmore, D. L.; Dluhy, R. A. *Appl. Spectr.* **2000**, *54*, 956.

(40) Du, Q.; Xiao, X.; Charych, D.; Wolf, F.; Frantz, P.; Shen, Y. R.; Salmeron, M. *Phys. Rev. B* **1995**, *51*, 7456.

(41) Fraenkel, R.; Butterworth, G. E.; Bain, C. D. *J. Am. Chem. Soc.* **1998**, *120*, 203.

(42) Beattie, D. A.; Haydock, S.; Bain, C. D. *Vibr. Spectrosc.* **2000**, *24*, 109.

(43) Berg, O.; Klenerman, D. *J. Appl. Phys.* **2001**, *90*, 5070.

(44) Berg, O.; Klenerman, D. *J. Am. Chem. Soc.* **2003**, *125*, 5493.

(45) Lagutchev, A. S.; Patterson, J. E.; Huang, W.; Dlott, D. D. *J. Phys. Chem. B* **2005**, *109*, 5033.

(46) Patterson, J. E.; Dlott, D. D. *J. Phys. Chem. B* **2005**, *109*, 5045.

(47) Patterson, J. E.; Lagutchev, A. S.; Huang, W.; Dlott, D. D. *Phys. Rev. Lett.* **2005**, *94*, 015501.

(48) Patterson, J. E.; Lagutchev, A. S.; Hambir, S. A.; Huang, W.; Yu, H.; Dlott, D. D. *Shock Waves* **2005**, *14*, 391

(49) Willets, K. A. and Van Duyne, R. P. *Annu, Rev. Phys. Chem.* **2007,** *58,* 267.

(50) Dick, L. A.; McFarland, A. D.; Haynes, C. L.; Van Duyne, R. P. *J. Phys. Chem. B.* **2002,** *106,* 853.

(51) Litorja, M.; Haynes, C. L.; Haes, A. J.; Jensen, T. R.; Van Duyne, R. P. *J. Phys. Chem. B.,* **2001,** *105,* 6907.

(52) Moskovits, M. in *Surface-Enhanced Raman Scattering: Physics and Applications,* vol. 103 of *Topics in Applied Physics,* K. Kniepp, M. Moskovits, H. Kniepp, Eds. (Springer-Verlag, Berlin, 2006), pp 1-17.

(53) Campion, A. and Kambhampati, P. *Chem. Soc. Rev.* **1998,** *27,* 241.

(54) Fang, Y.; Seong, N.-H.; Dlott, D. D. *Science,* **2008,** *321,* 388.

(55) Jayaraman, A. *Rev. Mod. Phys.* **1983,** *55,* 65.

(56) Klotz, S.; Chervin, J-C.; Munsch, P.; Le Marchand, G. *J. Phys. D: Appl. Phys.* **2009,** *42,* 075413.

(57) Angel, R. J.; Bujak, M.; Zhao, J.; Gatta, G. D.; Jacobsen, S. D. *J. Appl. Cryst.* **2007,** *40*, 26.

(58) Mao, H. K.; Xu, J.; Bell, P. M. *J. Geophys. Res.* **1986**, *91*, 4673.

(59) Goettel, K. A.; Mao, H.-K.; Bell, P. M. *Rev. Sci. Instrum.* **1985,** *56,* 1420.

(60) Hemley, R. J.; Mao, H-K.; Shen, G.; Badro, J.; Gillet, P.; Hanfland, M.; Häusermann, D. *Science,* **1997,** *276,* 5316.

(61) Zel'dovich, Y. B. and Raiser, Y. P. *Physics of Shock Waves and High-temperature Hydrodynamic Phenomena* (Academic Press, New York, 1966).

(62) Dlott, D. D. *Annu. Rev. Phys. Chem.* **2011,** *62,* 575.

(63) Marsh, S. P. *LASL Shock Hugoniot Data*. (University of California Press, Berkeley, CA, 1980).

(64) Watson, S.; Gifford, M. J.; Field, J. E. *J. Appl. Phys.* **2000,** *88,* 65.

(65) Bowden, M. D. and Drake, R. C. *Proc. Of SPIE*, **2007,** *6662,* 66620D-1.

(66) Bowden, M. D.; Drake, R. C.; Maisey, M. P.; Richardson, J.; Whitehorn, L. J.; Williams, A. R. *13th International Detonation Symposium,* **2006,** IDS014.

(67) Greenaway, M. W.; Gifford, M. J.; Proud, W. G.; Field, J. E.; Goveas, S. G. *Shock Compression of Condensed Matter-2001.* M. D. Furnish, N. N. Thandhani, Y. Horie, Eds. (American Institute of Physics, 2002) pp 1035-1038.

(68) Paisley, D. L.; Luo, S.-N.; Greenfield, S. R.; Koskelo, A. C. *Rev. Sci. Instrum,* **2008,** *79,* 023902.

(69) Gruzdkov, Y. A.; Dreger, Z. A.; Gupta, Y. M. *J. Phys. Chem. A.,* **2004,** *108,* 6216.

(70) Trunin, R. F.; Zhernokletov, M. V.; Kuznetsov, N. F.; Radchenko, O. A.; Sychevskaya, V. V.; Shutov, V. V. *Sov. J. Chem. Phys.,* **1992,** *11,* 606.

(71) Manner, V. W.; Sheffield, S. A.; Dattelbaum, D. M.; Stahl, D. B. *Shock Compression Cond. Matt.-2011,* **2012,** *1426,* 201.

Chapter 2: Static Pressure Experimental[1]

2.1 Diamond Anvil Cell

A Merrill-Bassett type diamond anvil cell (DAC) was used, based on a design provided by Prof. E. L. Chronister of the University of California. In this design, the diamonds are affixed and held in place onto the backing plate through a collet that is press-fit over the diamond and into the plate. A thin piece of copper foil fills the gap between the collet and the diamond, preventing the diamond from slipping out. The diamonds were aligned for overlap as well as parallelism, indicated by wide Fresnel fringes that span the surface of the culet interface (diamonds that are not parallel will have thin fringes on one edge only). The DAC had two opposing type IA Raman ultra-low fluorescence diamonds (Almax) with 0.80 mm culets. Beryllium-copper gaskets 0.016 in. thick were pre-indented to approximately 7 or 8 GPa,[1] and a 235 μm hole was drilled in the gasket center using an electronic discharge milling machine.

The highest quasi-hydrostatic pressure attainable in a DAC is dependent upon a combination of culet size, gasket material, PTM, and cell type used[2,3]. While some configurations allow pressures of several hundred GPa, our configuration only allowed pressures under ~10 GPa. The thickness and softness of the gasket was chosen to allow pressure variation in sub-GPa increments for maximum data points. Ruby chips were used as the pressure calibrant. Argon was used as the pressure-transmitting medium (PTM) for the monolayer and NBT solid experiments and was cryogenically loaded into the DAC in the following manner: the DAC was placed into a brass chamber and the chamber was filled with Ar gas. The chamber was partially submerged in liquid nitrogen. When the system reached equilibrium, Ar gas was slowly flowed

[1] Portions of this chapter have previously been published in the following article: Brown, K. E. and Dlott, D. D. *J. Phys. Chem. C* **2009,** *113,* 5751–5757.

into the chamber. As the boiling point of N (77.4 K) is lower than the boiling point of Ar (87.3 K), Ar gas condensed in the cold chamber and filled the DAC. Once the liquid Ar line was above the sample chamber of the DAC, the three DAC screws were tightened to slightly beyond the gasket pre-indentation tightness (indicated by a marker) to trap the Ar in the sample chamber.

For the NBT experiments, we used Moissanite (SiC) anvils instead of diamond anvils, as the diamond Raman transition overlaps the $\nu_{NO_2}^{S}$ symmetric stretching transition near 1345 cm^{-1}.

2.2 Sample Preparation

For neat liquid BT or BMT (Aldrich) studies, the DAC was loaded with a drop of the liquid with no further purification, along with a few ruby chips. No additional pressure-transferring medium was used. For neat solid powder NBT (Aldrich) studies, the powder was loaded in the DAC with no further purification, along with a few ruby chips, and Ar was used as the PTM.

The SERS substrates, consisting of a silver film over nanospheres (AgFON) with BT or BMT adsorbates, were prepared by well-known methods[4,5,6] developed by the van Duyne group of Northwestern University. We modified the procedure to make samples small enough to fit into the DAC. Ordinarily, AgFON substrates are prepared on the hydrophilic surfaces of glass microscope cover slips 100 μm thick (or even thicker glass slides) treated with piranha solution, but for our DAC the substrate is preferably no thicker than ~10 μm. We used a thin, tough polymer sheet of 12.5 μm thick polyester cut into 1-inch squares. Since the polyester surface was not hydrophilic, a <1 μm thick layer of *poly*-vinyl alcohol (PVA) was spin-coated on the surface using 0.5 mL of a 20 μM aqueous solution. The PVA-coated surface was rinsed with distilled water and then drop-coated with 2 μL of an aqueous suspension of 330 nm polystyrene nanospheres (Duke Scientific, functionalized to be hydrophilic), sufficient to produce a colloidal

monolayer on a 1 cm^2 surface. Once dried, 150 nm of silver was deposited on the sample using an electron beam evaporator. The sample was submerged overnight in a solution of 1mM BT or BMT in hexanes or NBT in ethanol to create a self-assembled monolayer. The samples were rinsed in ethanol to remove and un-bound thiol molecules. Fig. 2.1 shows a cartoon of the SERS substrate.

Unfortunately, the SAM-coated SERS substrates were imperfect. The imperfections were manifest in spatial nonuniformities, and electron microscopy revealed that the nanospheres did not form a well-ordered monolayer on the surface but instead created defect-laden multilayer patches and nominally bare patches (Fig 2.2). This presumably occurred due to insufficient hydrophilicity of the PVA surface. For this reason, the SERS intensity was 5-10 times less than expected from a well-formed AgFON substrate[4,7] . The one inch square sample was mounted in the Raman apparatus, and the sample was translated until a region providing the best Raman signal was identified. Then a scalpel was used to cut out a small piece of this region approximately 150 μm in diameter. The DAC was loaded with the sample and a few ruby chips, and was then cryogenically loaded with argon. Fig 2.3 shows the interior of the loaded DAC.

2.3 Raman Measurements

The homemade Raman apparatus, depicted in Fig 2.4, consisted of a coaxial white-light video microscope and 532 nm Raman microscope. The sample could be imaged in white light and translated with the microscope stage to direct the laser beam to the sample or to any of the ruby chips. A ¼ m spectrograph with CCD (Andor) with a 200 μm slit and a resolution greater than 10 cm^{-1} was used as the Raman detection system. The laser beam intensity was 5 mW for BT and BMT experiments and 1 mW for NBT experiments, and the beam was focused to a

diameter ($1/e^2$) of ~15 μm. Spectra were recorded with an acquisition time of 1 minute. The pressure-dependent spectra of neat BT, BMT and NBT and their respective SAMs were each taken multiple times and good consistency was obtained. Spectra were obtained by incrementally increasing the pressure, allowing the cell to equilibrate for about 10 min at each pressure.

2.4 Figures

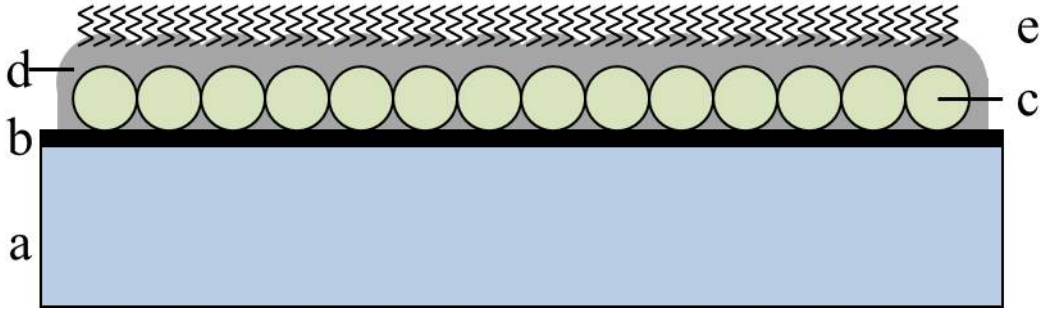

Figure 2.1: A cartoon of the photonic SERS substrate. a) 12.5 μm polyester film (Mylar); b) PVA layer to increase hydrophilicity; c) 300 nm polystyrene nanospheres; d) 150 μm layer of Ag; e) SAM

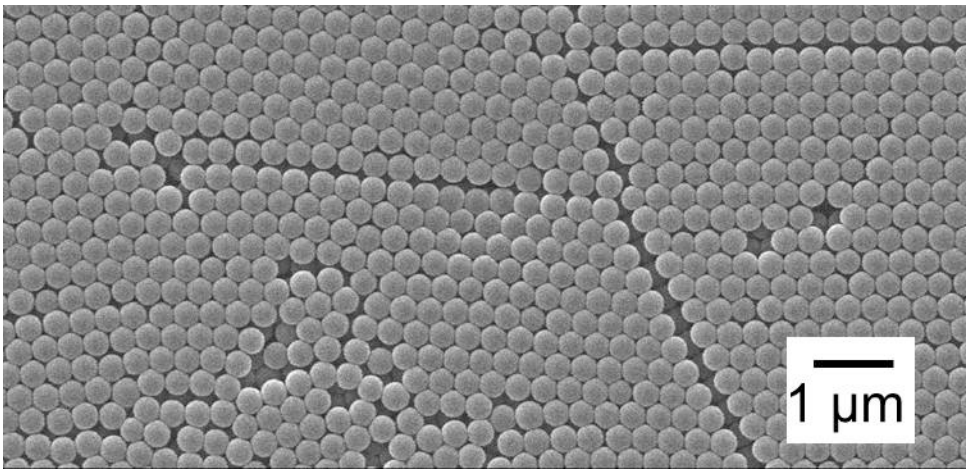

Figure 2.2: SEM image of defect-laden SERS substrate. While some areas are hexagonally close-packed, there are several point and line defects, as well as the nanospheres forming a multilayer.

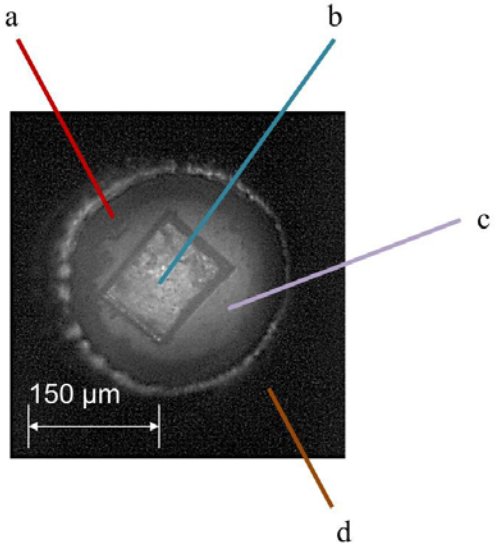

Figure 2.3: White light microscope image of the interior of the loaded DAC. a) ruby chip for pressure calibration; b) photonic SERS chip with SAM; c) Ar pressure medium; d) Be-Cu gasket

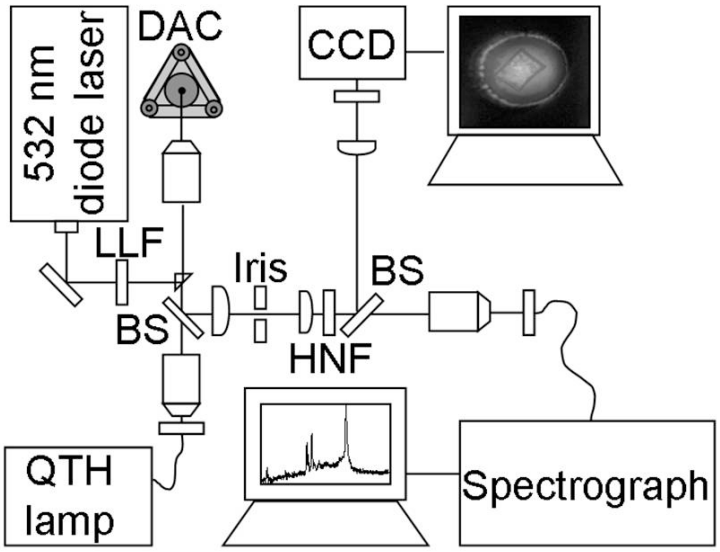

Figure 2.4: Block diagram of DAC Raman microscopy apparatus. QTH: quartz-tungsten halogen lamp; LLF: laser line filter; BS: beam splitter; HNF: holographic notch filter; CCD: charge-coupled device sensor.

2.5. References

(1) Dunstan, D. J. *Rev. Sci. Instrum.* **1989,** *60,* 3789.

(2) Eremets, M. I. *J. Raman Spectrosc.* **2003,** *34*, 515–518.

(3) Jayaraman, A. *Rev. Mod. Phys.* **1983,** *55,* 65-108

(4) Haynes, C. L.; Van Duyne, R. P. *J. Phys. Chem. B* **2001**, *105*, 5599.

(5) McFarland, A. D.; Young, M. A.; Dieringer, J. A.; Van Duyne, R. P. *J. Phys. Chem. B* **2005**, *109*, 11279.

(6) Yonzon, C. R.; Zhang, X. Y.; Zhao, J.; Van Duyne, R. P. *Spectroscopy* **2007**, *22*, 42.

(7) Fang, Y.; Seong, N.-H.; Dlott, D. D. Measuring the distribution of Raman enhancements on a nanoparticle lattice. In *Proceedings of the XXIst International Conference on Raman Spectroscopy*; Withnall, R., Chowdhry, B. Z., Eds.; IM Publications LLP: Charlton, Chichester, **2008**; p 469.

Chapter 3: Surface-Enhanced Raman Spectroscopy of Molecular Monolayers under High Static Pressure[1]

3.1 Benzenethiol and Benzenemethanethiol

In this study, we compare the high pressure (0-10 GPa) vibrational responses of organic molecules in self-assembled monolayers (SAMs) on metal surfaces and in bulk solids. The molecules studied were benzenethiol (BT) and benzenemethylthiol (BMT). For the SAM studies the molecules were adsorbed on a periodically nanostructured photonic substrate having a surface layer of polycrystalline Ag(111). The substrate was engineered to increase the Raman cross section by a factor of $\sim 10^5$ via surface enhanced Raman scattering (SERS)[1,2] so that similar Raman intensities were observed from monolayers and solids. We employed diamond anvil cell (DAC) technology to exert pressure on the solids and quasi-hydrostatic pressure on the SAMs (Figure 3.). We believe the present work to be the first study of molecular monolayers in a high-pressure DAC and the first demonstration of SERS technologies at high pressures. This technology is potentially a useful tool for the development of a fundamental molecular-level understanding of metal-lubricant[3,4,5] interactions and spontaneous self-assembly processes.[6,7]

Depending upon how the organic molecules are anchored to the substrate, compression of a SAM could be similar to or very different from compression of a bulk material. Based on studies of bulk materials similar to BT and BMT such as crystalline benzene,[8,9] naphthalene[10] and anthracene[10,11] , at the highest pressures used here an overall volume compression of $\Delta V = 1\text{-}V/V_0 \approx 0.3$ might be expected.[12] Molecular compression in this regime is ordinarily presented

[1] Portions of this chapter have previously been published in the following articles: (1) Brown, K. E. and Dlott, D. D. *J. Phys. Chem. C* **2009,** *113,* 5751–5757. (2) Fu, Yuanxi; Friedman, Elizabeth A.; Brown, Kathryn E.; Dlott, Dana D. *Chem. Phys. Lett,* **2011,** *501,* 369-374.Yuanxi Fu and Elizabeth Friedman took the 4-nitrobenzenethiol data, and Christopher Berg took the SFG data.

primarily as a decrease of intermolecular coordinates,[13,14,15] with solid-solid phase transformations possible or even likely. Actual molecular deformation ordinarily plays minor roles at these pressures unless something special happens such as charge transfer, dimerization, polymerization or large-scale conformational change.[10]

With a SAM, a more compressible organic layer is anchored to a comparatively incompressible metal substrate. Pressure will also compress the polymer nanospheres which support the metal thin film. However, the nanosphere compression will not change the metal layer volume, but will instead cause only a small change in the metal film curvature.

For SAM compression we will consider two limiting cases, keeping in mind that the real situation may lie between these extremes. If the adsorbates were *firmly anchored* to their attachment points, compression would be uniaxial, along the surface normal, as illustrated in Figure 3. (the adsorbate molecules are represented by cylinders for simplicity). A 30% compression would create 30% strain along the surface normal and zero strain in the plane. If the adsorbates were *mobile* and could diffuse on the surface, then compression would be much more isotropic. There would be a component parallel to the surface normal and a component parallel to the plane. Roughly speaking a 30% compression would create much less strain, e.g. 10% strain along three axes. (Here we are assuming isotropic compression. Although aromatic molecular solids ordinarily do not compress isotropically, the directional compressibilities will usually not vary by more than a factor of about two.[13,14,16])

For a SAM with a fixed number of mobile adsorbates, compression in the plane would be expected to cause a phase separation into denser regions and comparatively bare regions (Figure 3.). SAMs of the type studied here form with domains on the 10-100 nm scale,[17] so phase

separation at domain boundaries seems more likely than separation into two macroscopic patches.

Vibrational spectroscopy ought to be capable of distinguishing between these two limiting cases, although intermediate cases might be difficult to distinguish. Because the intermolecular potential is anharmonic and anisotropic, the molecular deformation needed to compress an organic layer of oriented molecules by a large factor in one direction *versus* a compression by a smaller factor in all directions, would be quite different and should be readily distinguishable in the Raman spectrum.

Results

Raman spectra

The vibrational modes and Raman spectra of substituted benzenes such as BT and BMT are well-known and have been discussed and catalogued in a comprehensive monograph.[18] We will use the conventional notation and assignments throughout. Figure 3. andFigure 3. compare the pressure-dependent Raman spectra of BT and BMT SAMs and solids. In the figures we blanked out the diamond Raman band. The data were obtained by increasing the pressure in increments, and there was no observed hysteresis in the pressure response for data acquired in the reverse direction. Our zero-pressure SERS spectra are consistent with the many such spectra in the literature[2,19,20,21,22], although the absolute intensity is lower than results obtained from the best SERS materials. The SERS spectra exhibit a structured background which is well-known, and absent from the neat BT and BMT spectra. The wavelength-dependent structure of this background depends on the architecture and construction of the SERS substrate. The prominent SH-stretch transitions in BT and BMT near 2570 cm^{-1} are missing in the SERS spectra, confirming that the SAMs are bound to Ag as the thiolate form.

Pressure dependent frequency shifting

All observed spectral transitions blueshifted with increasing pressure. Figure 3. andFigure 3. summarize the pressure-dependent blueshifts of prominent Raman transitions of BT and BMT solids and SAMs. Since benzene (mp 5.5°C) crystallizes at 298K at a low pressure of 0.07 GPa,[8] we expected BT (mp -15°C) and BMT (mp -29°C) also to crystallize at relatively low pressures. Unfortunately our DAC apparatus did not let us obtain spectra in the liquid state in the low-pressure regime <<1 GPa, since the liquids tended to leak from the gasket at the lowest pressures, so we were not able to investigate the freezing point in detail. The pressure-shift data we did obtain from neat BT and BMT do appear to evidence a discontinuity between ambient pressure and the lowest attainable pressure in the DAC, suggesting the freezing point is below 0.2 GPa.

In Figure 3. andFigure 3., the data for SAM vibrations that were significantly shifted relative to the solid were plotted with wavenumber offsets, as indicated, chosen to facilitate comparisons between SAMs and solids. In Figure 3. the BT SAM $\nu_{CS} + \nu_{6a}$ data were *blueshifted* by 10 cm^{-1} and the BT SAM ν_1 data were *blueshifted* by 20 cm^{-1}. In Figure 3., the BMT ν_{CS} SAM data were *blueshifted* by 25 cm^{-1} and the BMT ν_{CH_2}SAM data were *redshifted* by 20 cm^{-1}.

As seen in Figure 3. andFigure 3., the phenyl ν_{CH} data (~3060 cm^{-1}) of BT and BMT SAMs were of poor quality due to the weak signals and structured optical backgrounds. It might be possible to fine-tune our SERS fabrication to produce better results in this region by redshifting the plasmon resonance to better overlap with the ν_{CH} Raman emission. For completeness we plotted our best attempt at extracting the CH-stretch frequency shift in Figure 3. andFigure 3., but the CH-stretch data should be regarded as the least reliable and will not be interpreted in detail. The methylene ν_{CH_2}-stretch data (~2930 cm^{-1}) of BMT almost completely

disappears in the SAM, again partly due to structured optical backgrounds and poor plasmon resonance overlap, but the weak signal is largely due to the parallel orientation of the mode to the surface,[20] and so is not discussed.

Figure 3. andFigure 3. show that, once one accounts for the few vibrations that evidence a noticeable frequency shift upon forming a SAM, there is not much difference between the pressure responses of the molecules in a SAM and in a solid. In other words, the pressure response is significant but the differential pressure response between molecules in the solid or adsorbed on a surface is small. But there are a few cases where the data are suggestive of a differential pressure response that might be significant beyond the data scatter. These cases, which we will now examine in detail, are ν_{CS}, ν_{18a} and ν_{8a} for BT and ν_{18a} for BMT. The ν_{18a} mode is described as originating from symmetric in-plane CH bending and the ν_{8a} mode as a symmetric in-plane rocking of the CH units.[28] The vibrational transitions not discussed in detail below, to the best of our ability to discern, have the same pressure-shift behavior in SAM and solid.

Pressure dependent spectra

In the case of the BT ν_{CS}, Figure 3. suggested that as the samples were compressed, the solid and monolayer shifted together up to ~4 GPa, but above 4 GPa the SAM blueshift lagged behind the solid. The spectra shown in Figure 3. confirm that this effect is real. In Figure 3., at lower pressures of 2.7 GPa, the solid and monolayer shifts appear identical, but at higher pressures of 7 and 7.7 GPa the SAM spectra were clearly redshifted from the solid.

In the case of BT ν_{18a}, Figure 3. suggested that as the samples were compressed, the solid-state blueshift always lagged behind the monolayer blueshift. The spectra in Figure 3. confirm that this effect is also real.

For BT mode 8a, the pressure-shift data in Figure 3. do not suggest much difference between the SAM and solid, but a closer examination of the spectra show this is not the case. There is a dramatic pressure effect on the transition width for the SAM that is not observed in the solid. As seen in Figure 3., in the SERS spectrum the ν_{8a} vibration broadens significantly with increasing pressure to about twice its low pressure width whereas the solid-state spectrum does not.

In contrast to the BT ν_{CS} data, which shows clear differences in pressure shift in the SAM above 4 GPa, in the case of BMT there appears to be no difference in the pressure shift. Note that in BMT there is a zero-pressure blueshift for the SAM of 25 cm^{-1} compared to the solid, so in Figure 3. as in Figure 3., we blueshifted the SERS data by 25 cm^{-1} to align the low pressure solid and monolayer transitions. Figure 3. shows that once this static blueshift is taken into account, the ν_{CS} pressure shift is the same in the BMT SAM and solid.

For BMT ν_{18a}, Figure 3. suggested the pressure-shift behavior is different in SAM and solid and opposite the behavior of BT ν_{18a}. In BT the SAM pressure-blueshift is faster than in the BT solid, but for BMT the SAM pressure-blueshift seems slower than the BMT solid. In Figure 3., the 6 GPa and 7 GPa data appear to indicate this effect is also real.

Discussion

We have studied the pressure response of the BT and BMT molecules in order to investigate the differential pressure responses in solids and a self-assembled monolayer. The vibrational transitions all blueshift in response to increasing pressure. The pressure responses in the solid and the SAM are significant and quite similar. The similarity between these responses is incompatible with the anchored SAM model discussed previously.

The similarity between the solid and SAM data suggest that the mobile adsorbate scenario is the more reasonable description. Although we do not directly observe the phase separation, this suggestion is entirely compatible with what is known about SAM mobility on noble-metal surfaces and with the observation that SAMs can be pushed around on the surface with an AFM tip.[23] Most of what is known about organothiol motion on metal surfaces is based on studies of the self-assembly process that creates the SAM.[6,24,25] In-plane diffusion of thiols on noble metal surfaces allows the molecules to first adsorb at random sites and then diffuse along the surface to create densely-packed layers.

It is interesting that we do not see dramatic pressure-dependent variations in the SERS signal intensities due to physical changes in the dimensions of the SERS substrate, or due to the proposed phase segregation process. Recently it was shown[26] that most of the SERS signal is generated by just a small fraction of the SAM molecules residing in limited regions of space, primarily the crevasses between adjacent spheres. More than one-half of the Raman signal is generated by less than 1% of the SAM molecules in these regions,[26] so as long as empty patches do not form in the crevasses, the overall SERS intensity will not be much affected by compression.

Differences in the response of BT or BMT in the SAM and solid are relatively small. Nevertheless, we have identified two clear examples of differential responses:

1. Mode ν_{18a}, a symmetric in-plane CH-bending vibration has a clearly different pressure dependence in SAMs and solids. Interestingly, in BT the pressure-dependent blueshift is *larger in the SAM* than in the solid but in BMT the blueshift is *smaller in the SAM* than in the solid.

2. In ν_{CS}, which should be viewed as a phenyl-S stretching vibration in BT and a CH_2-S stretching vibration in BMT, the pressure-dependent blueshift in BT is *smaller in the SAM* than in the solid. This difference appears only in the P > 4 GPa region. In BMT the ν_{CS} blueshift is no different in the solid or the SAM.

The other significant effect we observed involved ν_{8a} of BT, where the SAM spectra show a large pressure-dependent broadening not seen in the solid. Typically such broadening effects are associated with a pressure-dependent Fermi resonance. In this type of interaction, an overtone or combination transition close to the observed band but not easily observed due to its smaller cross-section becomes pressure-tuned into resonance. A Fermi resonance ordinarily arises as the result of a coincidence, so it is no surprise that the same resonance is not observed in the BT solid. A Fermi resonance can result in a linewidth determined by the intramolecular anharmonic coupling, which is frequently greater than the ordinary linewidth caused by vibrational dephasing.[27] Since Fermi resonance arises primarily via intramolecular coupling, the effect is not a sensitive probe of intermolecular interactions, and it will not be discussed further in that context.

The pressure-dependent vibrational frequency shift $\Delta\nu_i(P)$ for a mode with ambient pressure transition frequency $\nu_i(0)$ can be described as resulting from a density-dependent shift characterized by the mode Grüneisen parameter γ_i and the compressibility,[11]

$$\Delta\nu_i(P) = \nu_i(0)\left[\frac{V_0}{V(P)}\right]^{\gamma i} \qquad (1)$$

where V(P) is the volume. For mode ν_{18a}, a localized deformation of a monosubstituted benzene moiety, there is no reason to think that γ_i should be any different in BT or BMT--in the solid or SAM forms--so differential pressure shifts in the present experiments should be interpreted as

resulting primarily from differences in compressibility, i.e. the more compressible material will evidence the larger pressure blueshift. In this view the fact that the greatest blueshift is observed in the BT SAM is a reflection of the lower density of the BT SAM, which, on Au, self-assembles with a coverage density 37.8 $Å^2$/molecule that is about one-half the 20.5 $Å^2$/molecule for BMT.[7] A similar coverage disparity would also be expected for Ag surfaces.

To understand the differential pressure shift of ν_{CS} in BT not seen in BMT, we note that changing the packing of the phenyl rings in BT necessarily results in strain, probably bending, of the phenyl-S-Ag bond in BT, but a similar phenyl ring motion in BMT would introduce minimal strain due to the greater degree of conformational freedom in the phenyl-CH_2-S-Ag linkage of BMT. Straining or bending a bond causes a vibrational level to move to higher energy in the anharmonic potential, resulting in a redshifting of the transition frequency, so the ν_{CS} transition in the BT SAM has a smaller blueshift than in the solid.

Conclusion and Summary

We have measured, for the first time, the vibrational spectra of organic molecules in a self-assembled monolayer under static high pressure by arranging the molecules on a nanotextured photonic substrate that provides a greatly enhanced Raman intensity. Our most significant observation is that the pressure-shift behavior of BT and BMT in a SAM and in a pure solid are remarkably similar, and this is true for all the observed Raman bands including the few that shift significantly in going from solid to SAM. The similarity between the pressure shift behavior in the solids and in the SAMs indicates that SAM compression should not be viewed as a uniaxial compression of molecules anchored on a surface. We propose instead that the compressed molecules phase separate into densely packed and comparatively bare regions on the surface.

When we look at the pressure shift differences between these two environments, i.e. the differential pressure shift, some small but significant differences emerge. The ν_{18a} band appears to be the most sensitive probe of the structural distortion created by high pressure. The pressure blueshift of ν_{18a} is larger in the SAM than in the solid with BT and larger in the solid than the SAM with BMT. The pressure shift results from a combination of compressibility and Grüneisen parameter that determines the sensitivity of the vibrational frequency to density changes. Since the Grüneisen parameter for mode ν_{18a} is expected to be similar in BT and BMT SAMs and solids, we attribute the larger blueshift in the BT SAM to its larger compressibility, which is a result of the low surface density of BT molecules. The ν_{CS} transition for BT has a slightly different pressure dependence in the solid and in the SAM whereas this transition has the same behavior in BMT. We notice that displacements of the phenyl groups would be expected to cause more strain in the C-S-Ag bonds in BT than in BMT, since BMT anchor has more conformational degrees of freedom.

3.2 Nitro-benzenethiol

Nitro groups are a key functionality of most high-performance energetic materials, and vibrational spectroscopy of nitro groups under dynamic shock compression can be an important method for understanding fundamental mechanisms of energetic material (EM) initiation. Here, we used the same methods as previously described in this thesis (chapter 2) to investigate the vibrational spectra of nitro groups of the EM simulant 4-nitro-benzenethiol (NBT) under static high-pressure (to 8 GPa), as well as use laser flash-heating and sum frequency generation to examine the high-temperature (to ~600°C) response of the vibrational spectra of NBT.

Interpreting vibrational spectra under shock conditions can pose several problems. For example, a shock-induced frequency shift may result from opposing pressure blueshift and temperature redshift.[28]

The NBT EM simulant was studied in both the crystalline form ("solid") and as a SAM on polycrystalline Au or Ag (111) surfaces. The relevance of SAMs for ultrafast shock compression measurements stems from the fact that shock velocities in EM are a few nanometers per picosecond. The time resolution of shock compression measurements is limited by the shock front transit time across the sample layer being probed, so only monolayers will yield the highest possible time resolution.[29]

Additional Experimental Considerations

As part of this study, we investigated the effects of high temperature on a NBT monolayer. High temperature data can be complementary to static high pressure information, and can lend insight into the shock-compression behavior of the monolayer. A pertinent difficulty in studying EM at high temperature is their fast thermochemical reactivity. We have overcome this difficulty by employing the use of femtosecond laser-flash heating, where the SAM's metallic substrate is heated by many hundreds of K. Due to the thin film geometry, the temperature jump decays by thermal conduction on the nanosecond time scale. The nanosecond duration of the heat pulse applied to the SAM effectively suppresses chemical decomposition. The NBT SAM response to a temperature jump was probed by sum frequency generation (SFG), a surface-specific nonlinear coherent vibrational spectroscopy.

The flash-heating apparatus with nonresonant suppression[30,31] has been described in detail previously.[32] On a glass substrate, a Cr–Au thin film with adsorbed NBT SAM was flash-heated to a high temperature in the 600 °C range by femtosecond pulses. A femtosecond IR pulse

centered near 1345 cm^{-1} and a picosecond 800 nm pulse were used to obtain SFG spectra as a function of time delay after flash-heating. The spectroscopic resolution was 11 cm^{-1}. Because neither laser flash-heating nor SFG were central aspects of my thesis work, their theories and methods will not be discussed further.

Results

Figure 3. shows Raman spectra of the NBT SAM and solid at a lower pressure of 0.2 GPa, with some selected peak assignments. Four transitions were studied in detail, selected because they were not spectrally congested and had sufficient Raman intensities. These were the CS-stretch ν_{CS}, the CN-stretch ν_{CN}, the symmetric nitro stretch $\nu^{s}_{NO_2}$, and the totally-symmetric in-plane ring stretch ν_{8a}. Figure 3. compares SERS and solid-state spectra up to 7 GPa. Figure 3. shows the pressure-dependent blueshifts. Except for ν_{CS}, the shifting behavior was almost identical for SAM and solid, which was also the case in a previous study of benzenethiol (BT).[33]

It is useful to know the mode Grüneisen parameter γ for each transition, where γ is the relative change in wavenumber $\bar{\nu}$ with respect to the relative change in volume V,

$$\gamma = \frac{\delta \ln \bar{\nu}}{\delta \ln V} \qquad (2)$$

However, the quantity we can determine is the relative rate of energy change with pressure, $d\ln\bar{\nu}/dP$, and to convert this quantity to γ would require a knowledge of the isothermal compressibility $\kappa = -(d \ln V/dP)_T$ for the SAM, which we do not know. The values in Table 3.1 for a single substance, however, should be indicative of the relative magnitudes of the mode Grüneisen parameters. For the ν_{CS} determination we used the lower-pressure (<3 GPa) slope of the SERS data in Figure 3.a. The important conclusion is that $d\ln\bar{\nu}/dP$ is about the same for ν_{CN}, $\nu^{s}_{NO_2}$ and ν_{8a}, but it is about 10 times larger for ν_{CS}. A comparison to other SAMs is also possible.

The ν_{8a} transition was studied in BT (Fig. 3.9) and benzene-methyl-thiol (BMT) SAMs, and its pressure-dependent blueshift was almost identical to the NBT results in Figure 3.d. As seen in Figure 3., the Raman linewidths are narrower in the solid. Figure 3. compares the pressure-dependent Raman linewidths of $\nu^{s}_{NO_2}$ and ν_{8a}. The ν_{8a} linewidth does not change appreciably with pressure in the solid or the SAM. The $\nu^{s}_{NO_2}$ linewidth increases significantly, in both solid and SAM but the pressure dependences are quite different. In the SAM the linewidth increases by about a factor of three up to 3 GPa and then levels off. In the solid the linewidth does not increase much until ~4 GPa. Figure 3. compares the $\nu^{s}_{NO_2}$ transition of the NBT SAM with hydrostatic compression and with flash-heating. The ambient spectra were obtained with both SERS and SFG. In the SFG spectra the nonresonant signal from the Au substrate was suppressed using time-gating.[30,31]

The NBT flash-heating data are in good agreement with a previous study surveying many SAM structures.[32] Although SFG and Raman are quite different techniques, the $\nu^{s}_{NO_2}$ spectra are similar. The peak locations are close but the Raman has an ~15% greater width. The SFG spectrum is narrower because the SFG cross-section is the product of the IR and Raman cross-sections,[31] in the dipole approximation with nonresonant susceptibility suppressed. Figure 3. shows that flash-heating to 600 °C causes a small redshift of ~1 cm^{-1} that is quite reproducible, and negligible broadening. This is true at shorter (2 ps) time delay when nonequilibrium vibrational populations are present,[32] and at longer (80 ps) time delay when NBT and the substrate are in equilibrium at 600 °C. High pressure causes a significant blueshift of ~15 cm^{-1} and a FWHM increase from 25 to 70 cm^{-1}.

Discussion

Pressure-dependent spectra

Besides the usual pressure-dependent blueshifts, there are three features in Figure 3., 3.Figure **3.**, andFigure **3.** worth noting. The first is the similarity between the pressure shift of SAM and solid for ν_{CN}, $\nu^{s}_{NO_2}$ and ν_{8a} (Figure 3.b-d). The second is the unusual behavior of ν_{CS} in Figure 3.a. In the SAM, ν_{CS} blueshifts up to 3 GPa and then stops, whereas in the solid there is almost no shift at all. Since the CS linkage is part of the SAM anchor to its substrate, the pressure shift is suggestive of an adlayer structural relaxation in the 0–3 GPa range not present in the solid. The third is the behavior of the solid NBT ν_{8a} ring stretch mode in Figure 3.. A relatively sharp (FWHM 14 cm−1) band at lower pressures, at ∼5 GPa a weaker broader (FWHM ∼100 cm−1) feature appears on its red edge. With increasing pressure this broader feature blueshifts on top of the ν_{8a} peak, stealing its intensity. We suggest the broader feature is the asymmetric nitro stretch transition $\nu^{a}_{NO_2}$ which would be expected to be weak in the Raman spectrum. In this view, pressure tuning creates a Fermi resonance with ν_{8a}, leading to intensity redistribution and broadening.

Structural relaxation

The similarities of the pressure shift data for NBT SAM and solid can be viewed as surprising, since the SAM is anchored to a metal substrate. The same result was obtained in an earlier comparison of BT SAM and solid at high pressure.[33] This pressure shift result can be explained as follows.

Solid NBT in the Ar pressure medium would be expected to undergo a hydrostatic but somewhat anisotropic compression, based on static compression measurements of the closely-related solid, NB.[34] At the higher pressures used here (e.g. 6 GPa), NB solid undergoes volume

compression of ~25%.[34] According to X-ray data, NB crystals at 6.1 GPa compress by 14%, 4% and 10% along the a, b and c-axes respectively.[34]

NBT SAMs consist of molecules adsorbed on a comparatively incompressible metal substrate. Consider the possibility of sudden ~6 GPa hydrostatic compression, faster than the surface relaxation described below, a SAM would first be compressed only along the surface normal, as depicted in Figure 3.b. (With dynamic diamond anvil technology, samples could be loaded to 6 GPa in ~10 ms.[35]) This uniaxial response could, in principle, occur on a molecular time scale (picoseconds),[29] and the uniaxial strain would be ~25% at 6 GPa. Because molecular force constant tensors are highly anisotropic, the Raman spectrum of a solely uniaxial-compressed SAM would be quite different from an isotropically compressed solid. However, organic thiolates on noble metal surfaces are known to have a sluggish surface mobility, which is necessary for them to form highly-ordered monolayers.[6] Thiolate SAMs can also be pushed around a metal surface by an AFM tip.[23] Thus, we propose that the initial uniaxial strain undergoes a gradual shear relaxation when the shear stress overcomes the SAM adhesion to the substrate. The adhesion determines σ_{cr}. As illustrated in Figure 3.b, the shear relaxation resulting from hydrostatic compression would be a compression process, as opposed to the shear expansion (Figure 3.a) that would result from shock compression. We do not see the proposed uniaxial state or the shear relaxation because the relaxation apparently occurs faster than the several minutes needed for us to compress the sample and obtain spectra. It might be observable in the future using dynamically-actuated[35] DACs.

The CS-stretching transition ν_{CS} should be especially sensitive to the nature of SAM packing on surface. The ν_{CS} shift is minimal in the solid (Figure 3.a), but in the SAM there is a blueshift of ~7 cm−1GPa−1 up to ~3 GPa. Thus the shift data is suggestive of a shear-induced

rearrangement on the surface up to ~3 GPa. Above 3 GPa the SAM becomes practically incompressible for stress parallel to the surface plane.

Doorway modes

A steep shock front preferentially pumps energy into molecular vibrations[16,36,37,] at a rate proportional to the mode Grüneisen parameter (*c.f.* Eqs. (6) - (8) of Ref. [37]). Looking at the data in Table 3.1, in the SAM the CS-stretch transition ν_{CS} would be expected to be shock-excited an order of magnitude more efficiently than the nitro stretch or ring vibrations. Thus the ν_{CS} vibration can be considered a doorway mode for shock-to-molecule energy transfer in the SAM. This is apparently not true for solid NBT where the CS-linkage does not serve as a molecular support.

Nitro SAM spectra at high pressure and temperature

Figure 3. shows that flash-heating results in small thermal redshifts and broadening of the SAM $\nu^{s}_{NO_2}$ transition. In condensed media, the thermal redshift and broadening are frequently dominated by thermal expansion[38], but these flash-heating measurements are faster than thermal expansion. Another likely mechanism involves quartic anharmonic coupling between a higher-frequency vibration being observed, such as $\nu^{s}_{NO_2}$, and unobserved lower-frequency vibrations near kT.[39] Energy exchange between the lower-frequency vibrations and the bath cause a fluctuating anharmonic shift of the observed vibration that results in the redshift and broadening having identical temperature dependences proportional to the thermal occupation number of the lower-frequency mode.[39]

Figure 3. also shows that static high pressure causes the SAM $\nu^{s}_{NO_2}$ transition to blueshift, and this blueshift is about the same as in the solid. Thus it is reasonable to associate the $\nu^{s}_{NO_2}$ pressure blueshift with intra molecular anharmonicity. Increasing strain causes the

$\nu^{s}_{NO_2}$ ground-state ν = 0 to move up in energy, but the excited-state ν = 1 energy moves up to an even greater extent.

The SAM $\nu^{s}_{NO_2}$ transition broadens significantly in a pressure range (0–3 GPa) where the solid NBT linewidth is insensitive to pressure. At similar pressures the SAM phenyl ν_{8a} broadening is minimal. These observations lead us to associate the broadening with the nitro group location at the interface between the SAM and the Ar pressure medium. A likely hypothesis, supported by the similarity between the ν_{CS} pressure blueshift (Figure 3.a) and the $\nu^{s}_{NO_2}$ broadening (Figure 3.a), involves the proposed shear relaxation process described in Figure 3.b. During shear relaxation, the SAM molecules move in the plane to become more tightly packed, which requires the surface nitro groups to be dragged through the Ar pressure medium. This rearrangement creates disorder in the nitro groups via the dragging process, which in turn results in static inhomogeneous broadening. Another possibility, suggested by the observation that vacuum deposition of metal films on top of SAMs can lead to metal atoms being embedded within the SAM,[40,41] is that the inhomogeneous broadening is caused by Ar atoms in the SAM lattice. However we regard this as less likely[33] because, although there are strong interactions between organic molecules and metal atoms, organic molecules such as benzene are totally immiscible in Ar.

Relationships between static and dynamic shock-compression spectra

The flash-heating results show that the $\nu^{s}_{NO_2}$ transition of the SAM, on shorter time scales relevant to shock compression, is insensitive to high temperatures up to 600 °C and additionally insensitive to the nonequilibrium vibrational distributions created at the earlier stages of flash-heating. Thus we would expect the static and shock blueshifts to be similar at a given pressure, since the shock pressure blueshift will not be appreciably offset by a temperature

redshift. This could potentially be a useful simplification, since the shock pressure could then be determined in situ with reference to static high-pressure calibration measurements.

According to our hypothesis for the origin of the pressure broadening for $\nu^{s}_{NO_2}$ of the SAM, the broadening is associated with the shear relaxation process. This could be another potentially useful simplification where the initial uniaxial compression would be associated with a sudden blueshift with minimal broadening and the subsequent shear relaxation by a subsequent gradual broadening.

3.3 Figures and Tables

Table 3.1: Rate of pressure blueshift for nitrobenzenethiol SAM on Ag(111).

Vibrational transition	Ambient (cm^{-1})	$d\bar{\nu}/dP$ (cm^{-1} GPa^{-1})	$d\ln\bar{\nu}/dP$ (GPa^{-1})
ν_{CS} [a]	538	7.0	0.013
ν_{CN}	856	2.0	0.0023
$\nu^{s}_{NO_2}$	1331	2.1	0.0016
ν_{8a}	1574	3.4	0.0021

[a] The ν_{CS} data used the lower-pressure slope of the data in Figure 3.14a.

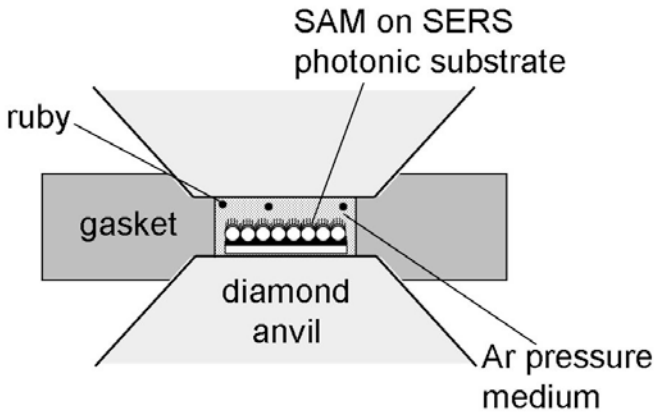

Figure 3.1: Schematic of diamond anvil cell (DAC) apparatus with self-assembled monolayer (SAM) on a nanofabricated surface-enhanced Raman (SERS) substrate in hydrostatic Ar pressure medium.

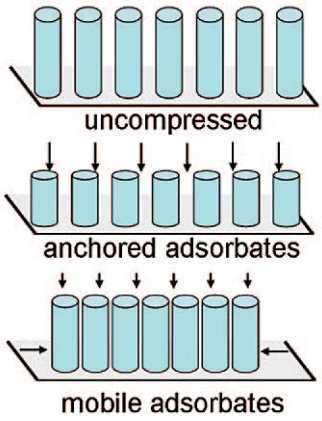

Figure 3.2: Two models for SAM compression at a fixed strain. If the SAM molecules (depicted as cylinders) are anchored to their attachment sites, the only strain will be uniaxial strain along the surface normal. If the SAM molecules are mobile, some of the strain will be along the surface normal and some will be in the plane, resulting in the creation of denser patches and comparatively bare patches.

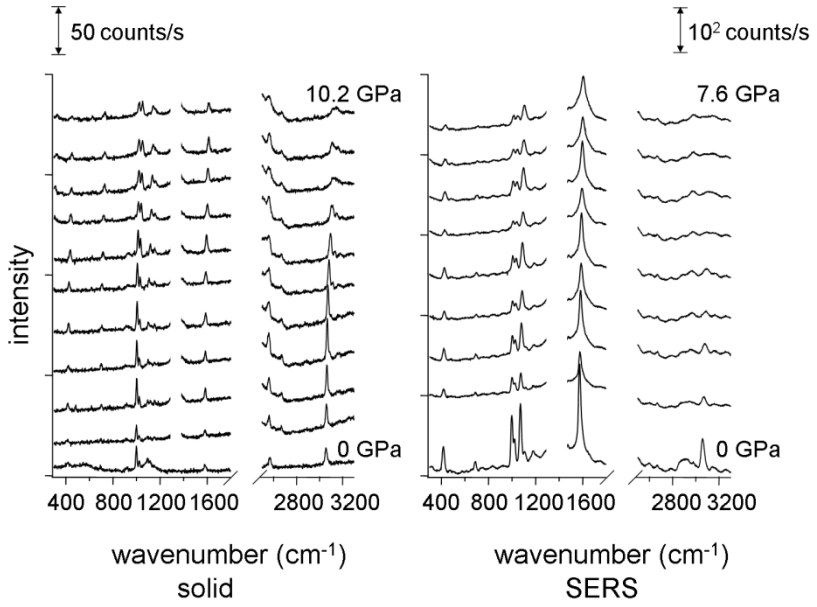

Figure 3.3: Pressure-dependent Raman spectra from solid BT (left) and BT SAM (right). From bottom to top, the pressures in GPa were (left) 0, 0.3, 0.6, 1.1, 2.0, 3.5, 5.5, 7.8, 9.0, 9.5, 10.2 and (right) 0, 0.6, 1.6, 2.6, 3.5, 4.9, 5.7, 6.6, 7.6.

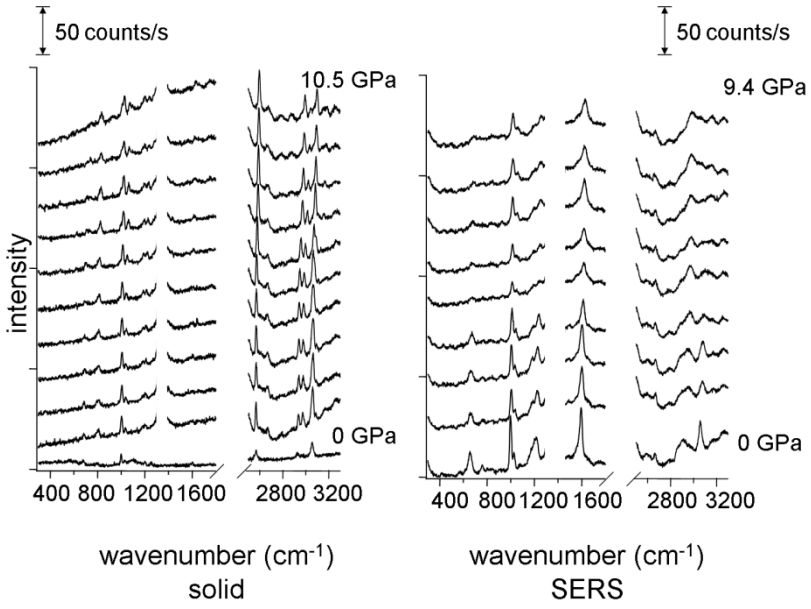

Figure 3.4: Pressure-dependent Raman spectra from solid BMT (left) and BMT SAM (right). From bottom to top, the pressures in GPa were (left) 0, 1.2, 1.6, 1.9, 2.3, 3.0, 4.6, 6.9, 8.4, 9.3, 10.5 and (right) 0, 1.7, 2.1, 4.2, 6.0, 6.8, 7.4, 8.7, 9.4.

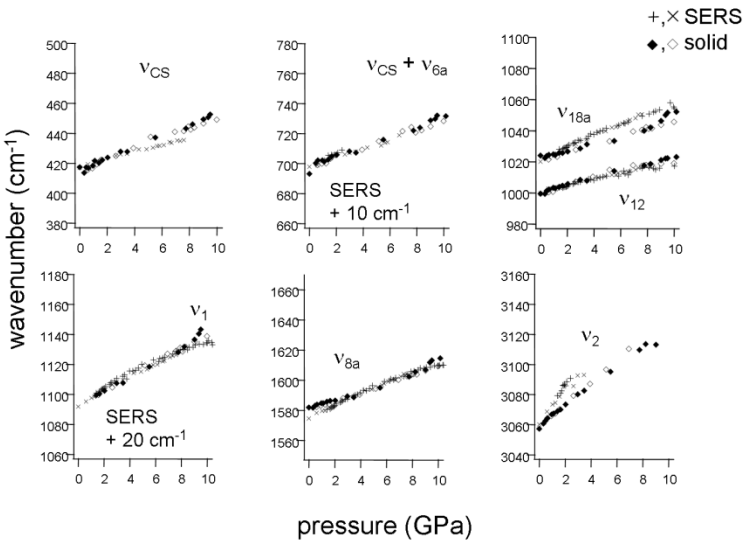

Figure 3.5: Comparison of pressure blueshifts of BT as a SAM (SERS data) and a solid. The ν_2 (CH-stretch) data are of low quality, and differences between SAM and solid are not regarded as significant.

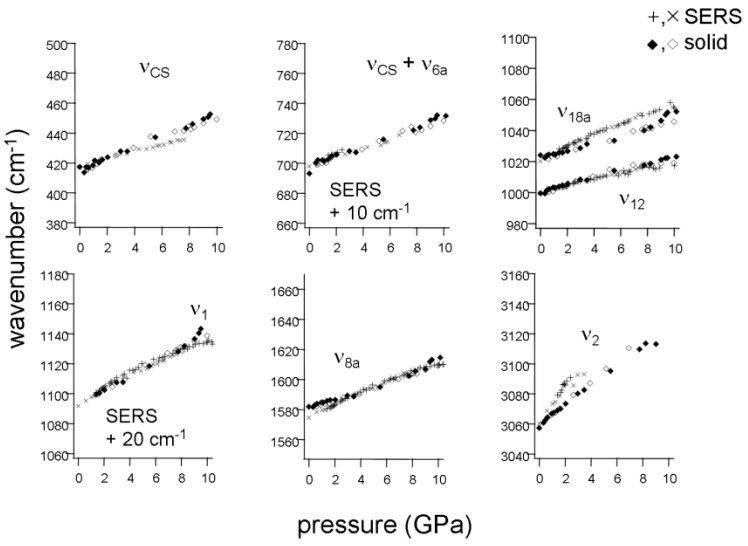

Figure 3.6: Comparison of pressure blueshifts of BMT as a SAM (SERS data) and a solid. The ν_2 (CH-stretch) data are of low quality, and differences between SAM and solid are not regarded as significant.

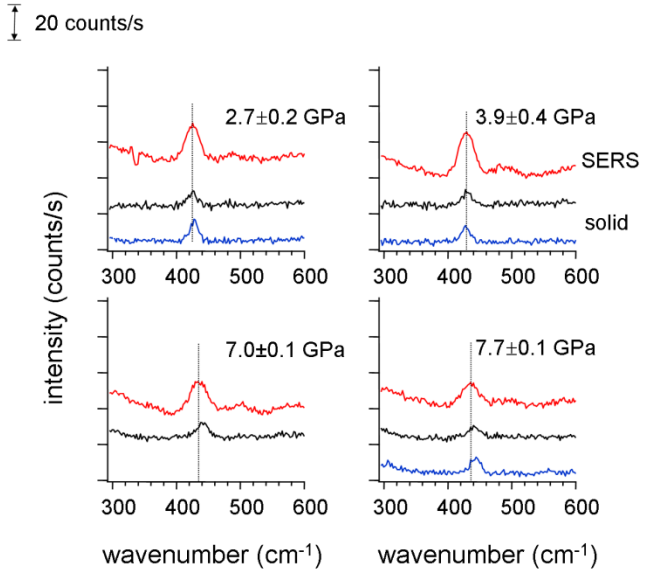

Figure 3.7: Lineshapes of the BT ν_{CS} transition at a few selected pressures as a SAM (SERS data) and a solid. The SAM and solid blueshift together up to ~4 GPa, then the SAM blueshift lags behind the solid.

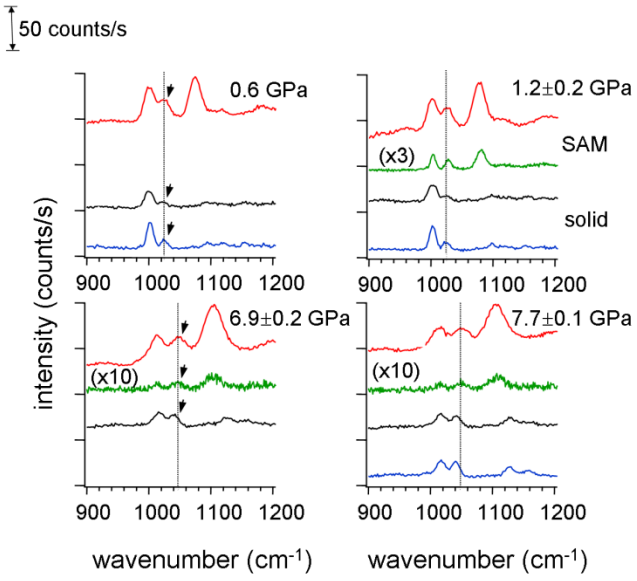

Figure 3.8: Lineshapes of the BT ν_{18a} transition, a symmetric in-plane CH bending mode, at a few selected pressures as a SAM (SERS data) and a solid. As pressure is increased, the SAM blueshift is greater than the solid.

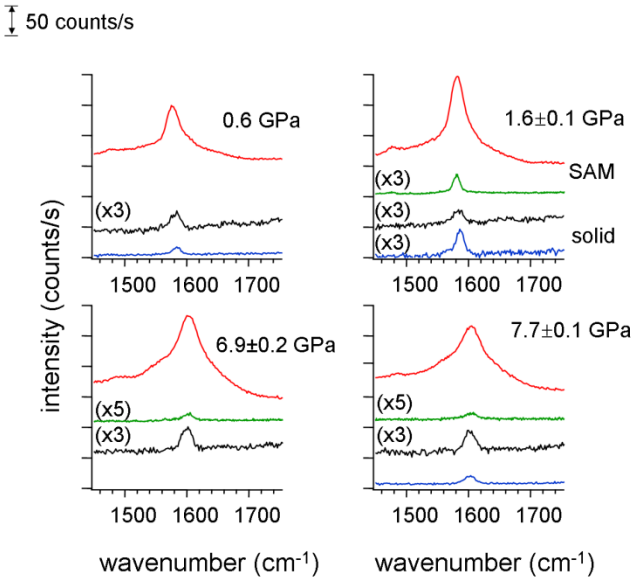

Figure 3.9: Lineshapes of the BT ν_{8a} transition at a few selected pressures as a SAM (SERS data) and a solid. As pressure is increased, the SAM transition broadens much more than the solid. The broadening is attributed to a Fermi resonance not occurring in the solid.

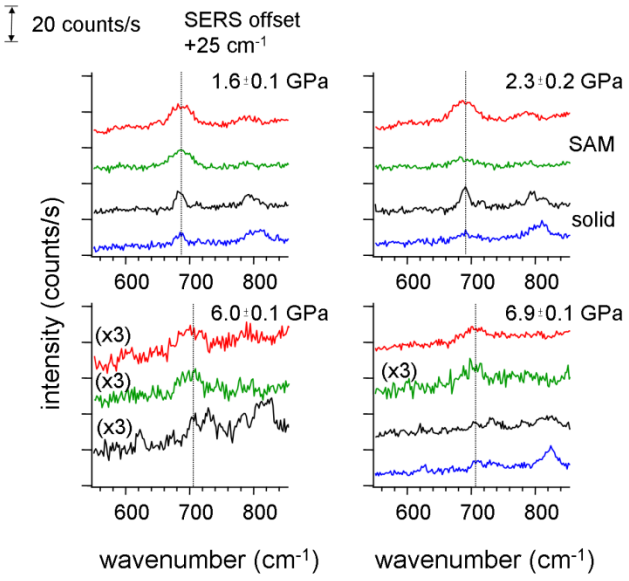

Figure 3.10: Lineshapes of the BMT ν_{CS} transition at a few selected pressures as a SAM (SERS data) and a solid. The ν_{CS} transition is redshifted 25 cm^{-1} in the SAM relative to the solid, so for comparison the SAM spectra above were blueshifted 25 cm^{-1}. In contrast to the BT data in Figure 3., in BMT the pressure blueshift in the SAM and solid are indistinguishable.

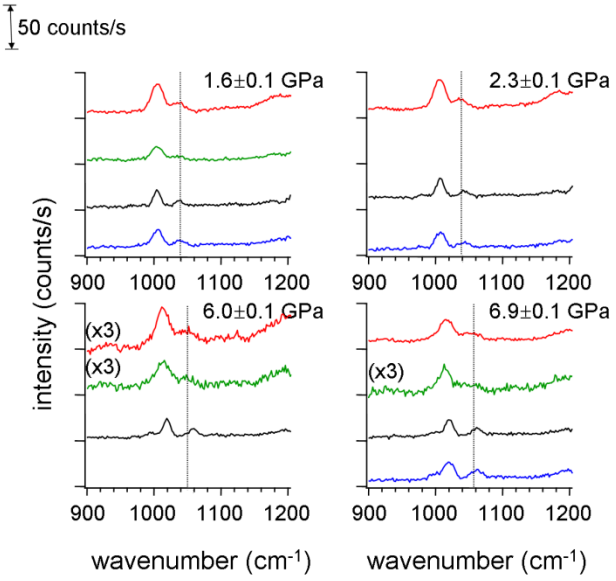

Figure 3.11: Lineshapes of the BMT ν_{18a} transition, a symmetric in-plane CH bending mode, at a few selected pressures as a SAM (SERS data) and a solid. As pressure is increased, the SAM blueshift is smaller than the solid.

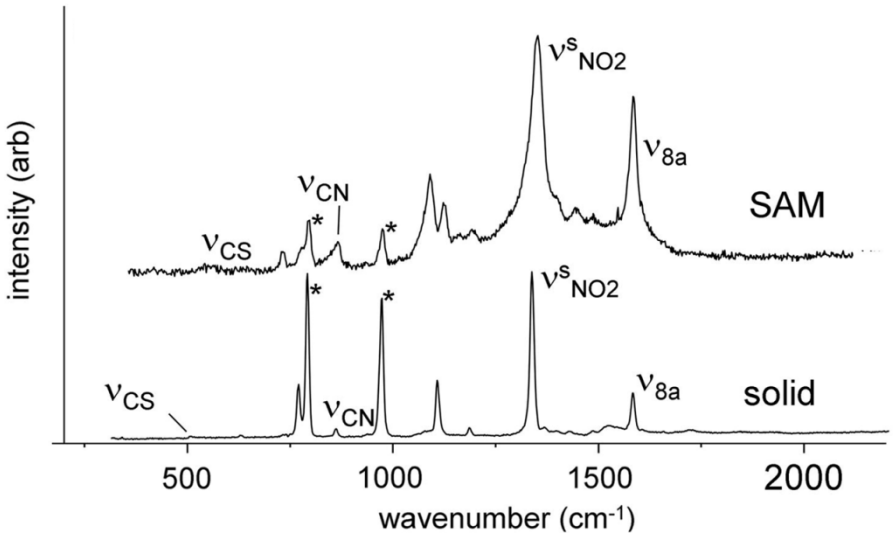

Figure 3.12: Raman spectra of NBT in the solid and as a SAM, at a lower pressure of ~0.2 GPa, with assignments of four prominent transitions. The * denote transitions of the SiC anvils. Courtesy of Yuanxi Fu.

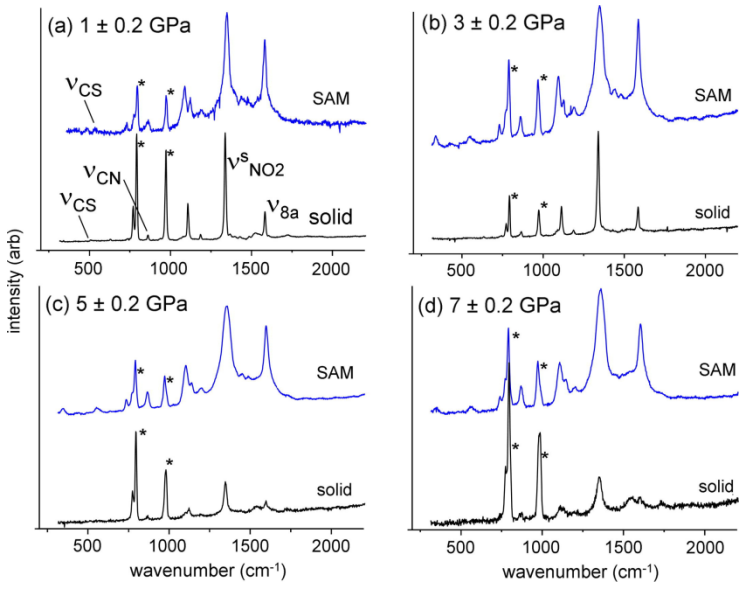

Figure 3.13: Raman spectra of NBT SAM on a photonic substrate with Ag(1 1 1) surface layer or as a neat solid. Transitions of the SiC anvil are indicated by *. Courtesy of Yuanxi Fu.

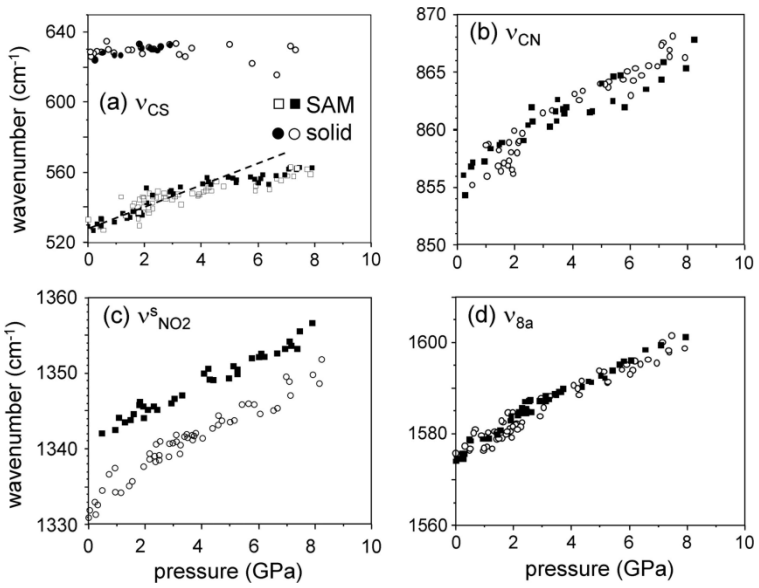

Figure 3.14: Pressure blueshifts of NBT SAM and solid for the four transitions indicated in Figure 3.. The line in (a) is a visual guide. Courtesy of Yuanxi Fu.

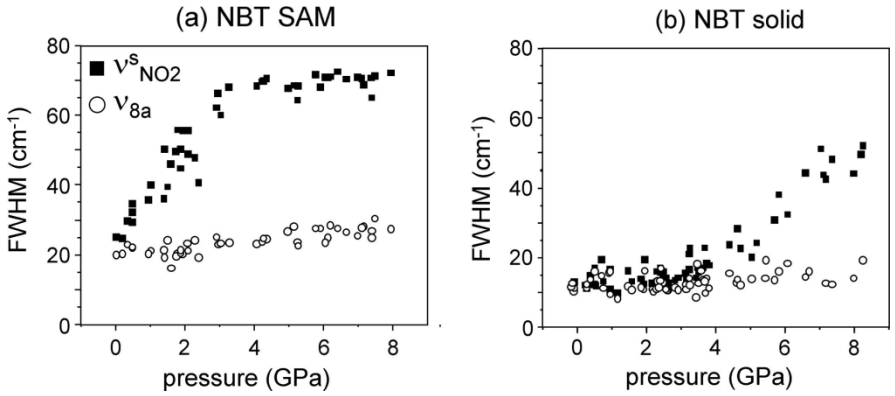

Figure 3.15: Pressure-dependent line broadening (FWHM) of the $\nu^s_{NO_2}$ and ν_{8a} transitions of NBT SAM and solid. Coutesy of Yuanxi Fu.

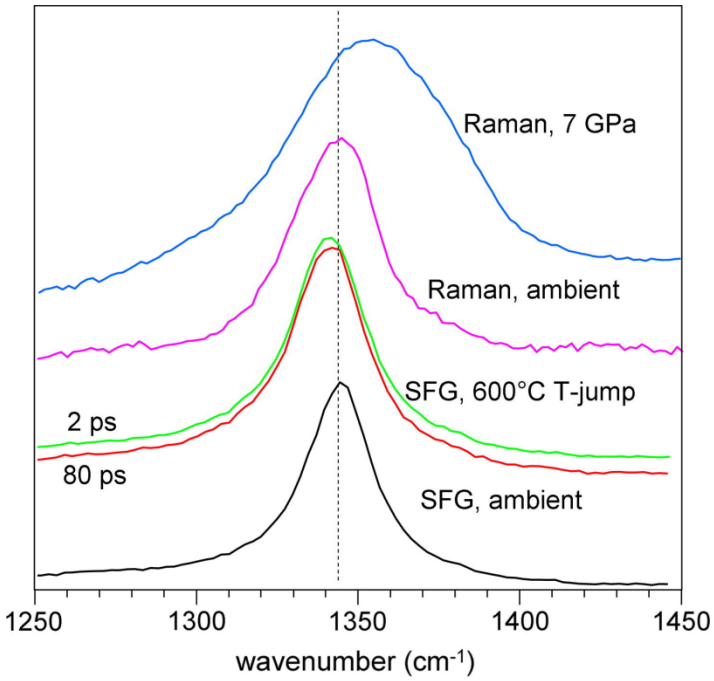

Figure 3.16: Spectra of $\nu^{s}_{NO_2}$ transition NBT SAM. Ambient spectra were obtained with both Raman and sum-frequency generation (SFG). With flash-heating a nonequilibrium population was observed at 2 ps. By 80 ps the SAM and surface are in equilibrium at 600 °C. The T-jump spectra, which are too fast for thermal decomposition or thermal expansion, show minimal redshift and broadening. At a high pressure of 7 GPa, the SAM shows a pressure blueshift and pressure broadening.

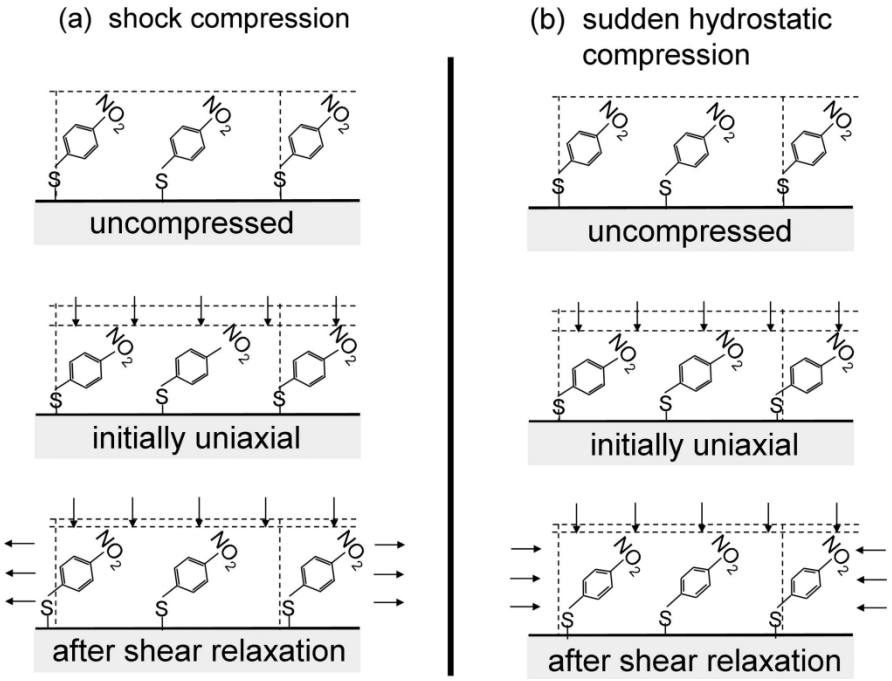

Figure 3.17: Schematic of the response of NBT SAM to (a) sudden shock and (b) sudden hydrostatic compression. Quasi 1D shock compression produces an initial state of uniaxial compression parallel to the surface normal. A subsequent shear relaxation can occur, caused by molecules moving outward parallel to the metal surface, converting part of the uniaxial strain to a transverse strain. Because the metal substrate is largely incompressible, a sudden hydrostatic compression also induced an initial uniaxial strain. A subsequent shear relaxation could result from molecules moving inward.

3.4 References

(1) Haynes, C. L.; Van Duyne, R. P. *J. Phys. Chem. B* **2001**, *105*, 5599.

(2) McFarland, A. D.; Young, M. A.; Dieringer, J. A.; Van Duyne, R. P. *J. Phys. Chem. B* **2005**, *109*, 11279.

(3) Mikulski, P. T.; Harrison, J. A. *J. Am. Chem. Soc.* **2002**, *123*, 6873.

(4) Brewer, N. J.; Foster, T. T.; Leggett, G. J.; Alexander, M. R.; McAlpine, E. *J. Phys. Chem. B* **2004**, *108*, 4723.

(5) Houston, J. E.; Doelling, C. M.; Vanderlick, T. K.; Hu, Y.; Scoles, G.; Wenzl, I.; Lee, T. R. *Langmuir* **2005**, *21*, 3926.

(6) Schreiber, F. *Prog. Surf. Sci.* **2000**, *65*, 151.

(7) Tao, Y.-T.; Wu, C.-C.; Eu, J.-Y.; Lin, W.-L.; Wu, J.-C.; Chen, C. *Langmuir* **1997**, *13*, 4018.

(8) Budzianowski, A.; Katrusiak, A. *Acta Crystallographica* **2006**, *B62*, 94.

(9) Ellenson, W. D.; Nicol, M. *J. Chem. Phys.* **1974**, *61*, 1380.

(10) Nicol, M.; Vernon, M.; Woo, J. T. *J. Chem. Phys.* **1975**, *63*, 1992.

(11) Zhao, L.; Baer, B. J.; Chronister, E. L. *J. Phys. Chem. A* **1999**, *103*, 1728.

(12) Vaidya, S. N.; Kennedy, G. C. *J. Chem. Phys.* **1971**, *55*, 987.

(13) El Hamamsy, M.; Elnahwy, S.; Damask, A. C.; Taub, H.; Daniels, W. B. *J. Chem Phys.* **1977**, *67*, 5501.

(14) Jordan, J. F. J.; Axmann, A.; Egger, H.; Kalus, J. *Phys. Status Solidi. A* **1982**, *71*, 457.

(15) Kitaigorodskii, A. I. *Molecular Crystals and Molecules*; Academic Press: New York, 1973.

(16) Jindal, V. K.; Dlott, D. D. *J. Appl. Phys.* **1998**, *83*, 5203.

(17) Siepmann, J. I.; McDonald, I. R. *Langmuir* **1993**, *9*, 2351.

(18) Varsányi, G. *Assignments for vibrational spectra of seven hundred benzene derivatives: Vol. 1.*; John Wiley and Sons: New York, 1974.

(19) Szafranski, C. A.; Tanner, W.; Laibinis, P.; Garrell, R. L. *Langmuir* **1998**, *14*, 3570.

(20) Joo, S.-W.; Kim, Y.-S. *Colloids and Surfaces A: Physicochem. Eng. Aspects* **2004**, *234*, 117.

(21) Joo, T. H.; Kim, M. S.; Kim, K. *J. Raman. Spectrosc.* **1987**, *18*, 57.

(22) Fang, Y.; Seong, N.-H.; Dlott, D. D. Measuring the distribution of Raman enhancements on a nanoparticle lattice. In *Proceedings of the XXIst International Conference on Raman Spectroscopy*; Withnall, R., Chowdhry, B. Z., Eds.; IM Publications LLP: Charlton, Chichester, 2008; p 469.

(23) Carpick, R. W.; Salmeron, M. *Chem. Rev.* **1997**, *97*, 1163.

(24) Grønbech-Jensen, N.; Parikh, A. N.; Beardmore, K. M.; Desai, R. C. *Langmuir* **2003**, *19*, 1474.

(25) Suo, Z.; Gao, Y. F.; Scoles, G. *J. Appl. Mech. Trans. Am. Soc. Mech. Engineer.* **2004**, *71*, 24.

(26) Fang, Y.; Seong, N.-H.; Dlott, D. D. *Science* **2008**, *321*, 388.

(27) Wilson, E. B.; Decius, J. C.; Cross, P. C. *Molecular vibrations: the theory of infrared and Raman vibrational spectra*; Dover: New York, 1980.

(28) Hare, D. E.; Franken, J.; Dlott, D. D. *J. Appl. Phys.* **1995,** *77*, 5950.

(29) Patterson, J. E.; Lagutchev, A.; Huang, W.; Dlott, D. D. *Phys. Rev. Lett.* **2005,** *94*, 015501.

(30) Lagutchev, A.; Hambir, S.A.; Dlott, D.D. *J. Phys. Chem. C* **2007,** *111*, 13645.

(31) Carter, J. A.; Wang, Z.; Dlott, D. D. *Acct. Chem. Res.* **2009,** *42*, 1343–1351.

(32) Carter, J. A.; Wang, Z.; Fujiwara, H.; Dlott, D. D. *J. Phys. Chem. A* **2009,** *113*, 12105–12114.

(33) Brown, K. E. and Dlott, D. D. *J. Phys. Chem. C* **2009,** *113,* 5751.

(34) Kozu, N.; Arai, M.; Tamura, M.; Fujihisa, H.; Aoki, K.; Yoshida, M. *Japan J. Appl. Phys.* **2000,** *39*, 4875.

(35) Evans, W.J.; Yoo, C.S.; Lee, G.W.; Cynn, H.; Lipp, M.J.; Visbeck, K. *Rev. Sci. Instrum.* **2007,** *78*, 073904.

(36) Tokmakoff, A.; Fayer, M.D.; Dlott, D. D. *J. Phys. Chem.* **1993,** *97,* 1901.

(37) Dlott, D.D., in: Politzer, P.; Murray, J.S. (Eds.), Energetic Materials: Initiation, Decomposition and Combustion, Part 2, Elsevier, New York, **2003**, p. 125.

(38) Bellows, J.C.; Prasad, P.N. *J. Chem. Phys.* **1979,** *70*, 1864.

(39) Shelby, R.M.; Harris,C.B.; Cornelius, P.A. *J. Chem. Phys.* **1979,** *70*, 34.

(40) Jung, D.R.; Czanderna, A.W. *Crit. Rev. Solid State Mater. Sci.* **1994,** *19,* 1.

(41) Zhu, Z; Daniel, T.A.; Maitani, M.; Cabarcos, O.M.; Allara, D.L.; Winograd, N. *J. Am. Chem. Soc.* **2006,** *128,*13710.

Chapter 4: Simplified Laser-Driven Flyer Plates for Shock Compression Science[1]

4.1 Introduction

Laser-launched flyer plates are a technology that brings shock compression science to the laboratory benchtop.[1-5] In this paper we describe a technology platform for launching flyer plates and monitoring their flight,[5] impact and effects on materials. We emphasize methods to simplify launch and flyer plate fabrication to free us to concentrate on novel materials and precision spectroscopic measurements. Laser-launched plates produce shocks with shorter durations than plates launched by more conventional gas guns. The duration of the fully-supported shock, τ_{sh}, is approximately the shock round-trip time in the plate,[6] which is about equal to the acoustic round-trip time. For Al flyers used here and in many other laboratories, the acoustic speed is 6.3 km/s. Although some laboratories launch very thin flyers (e.g. 2 μm[7] or 0.5 μm[8]) to achieve the greatest velocities, our goal was to launch flyers having high enough kinetic energies E_{kin} needed to trigger material transformations or to initiate energetic materials (EM), and that were thick enough to produce sustained steady planar 1D shocks. The longer these shocks persist, the easier it is to initiate EM[9,10] and to measure equations-of-state (EOS).[6] These goals require careful choices of flyer thickness, diameter and flight path. The considerations motivating these choices are discussed here. The launch, flight and impact events were monitored using photon Doppler velocimetry (PDV).[5,11,12] Highly-reproducible flyer plate velocities and highly-reproducible times-to-impact with the target achieved here are critically important for high-quality EOS measurements and for synchronization with high-speed detectors for time-resolved spectroscopy. We will illustrate the usefulness of this system with three

[1] This chapter has been submitted to *Rev. Sci. Instrum.* Authors are Brown, K. E.; Shaw, W. L.; Zheng, X. X.; Dlott, D. D. William Shaw was responsible for the PMMA Hugoniot measurements and shocked Al-Teflon measurements. Dr. Xianxu Zheng was responsible for the Raman measurements.

applications: Hugoniot EOS measurements of a polymer film, time-resolved emission from dye probes embedded in a shocked polymer film, and time-resolved emission of impact-initiated reactive nanomaterials (RM).

Reliable launching of flyer plates requires a high-energy pulsed laser that produces a uniform beam, ideally the "top hat" beam whose radial profile is a uniformly illuminated disk. If the launching beam were nonuniform, different parts of the flyer would travel at different velocities, the flyer could tear itself apart in flight,[7] and different parts of the flyer would impact the sample at different times. Since the literature includes a myriad of different launch systems and configurations, we propose that a useful way to compare different systems is by using the value of the maximum available laser fluence J (J cm^{-2}) at the flyer surface. If the flyer is bonded to a transparent substrate, optical damage may cause the fluence at the flyer surface to be considerably less than the incident fluence. Other factors such as maximum possible flyer plate speeds and kinetic energies are ultimately determined by this fluence, along with factors such as flyer plate diameter, thickness and the density of the flyer material. Another figure-of-merit that is widely cited is the efficiency[5,13] E_{kin}/E_p for converting laser pulse energy E_p into flyer kinetic energy E_{kin}. We find the conversion efficiency less useful for comparisons among systems. Although high fluences can be achieved simply by tight focusing of laser beams, the conditions needed for flyer launch to produce well-characterized planar shocks require beam diameters to exceed certain minimum values, so with a given pulse energy E_p, J cannot be increased without limit.

Laser-launched flyer plates have been developed in a number of laboratories, using a wide variety of different launch laser and flyer plate designs, depending on available technologies and research goals. To illustrate what we mean by "simplified" we briefly compare

two such designs. Sekine and co-workers[14,15] wished to produce tiny quantities of super hard materials for post-mortem analysis, such as six-coordinate diamond.[16] They needed extremely high impact velocities, and were not very concerned with a high level of shock planarity. They used an 8 ns, 100J laser to produce 1,000 J cm^{-2} fluence, to drive 10 μm Al foil to hypervelocities up to 14 km/s. The beam shaping optic was a lens that relayed a demagnified image of the final laser amplifier rod onto the foil. The foil was freestanding and the laser punched disks out of the foil. Tens of flyers could be shot from a single piece of foil. By contrast, Paisley and co-workers[3,4] wished to make precision EOS measurements, requiring extremely well-characterized impact conditions with minimal tilt and a long-duration shock lasting hundreds of ns generated by a thick (500 μm) large-diameter (8 mm) flyer plate. They used a large laser facility, the Trident Laser Facility at Los Alamos National Laboratory, having a master oscillator and a chain of Nd:Glass amplifiers producing 1000 J pulses with variable pulse durations from 0.1 to 1.0 μs. A custom-made holographic optical element was used to produce an 8 mm diameter pseudo-top hat beam consisting of a two-dimensional grid of minihotspots. The maximum fluence on target was 2000 J cm^{-2}. The flyer plate assembly had a transparent sapphire or glass substrate with a vapor-deposited coating consisting of a C layer said to help homogenize the drive plasma created by the minihotspots,[17] an Al layer, an Al_2O_3 layer and a final Al layer, to which an 8 mm diameter circular flyer plate was glued. This flyer assembly was sacrificial and could shoot only one flyer.

To produce a simplified flyer plate technology platform, we limited ourselves to "one box" commercial launch lasers, as opposed to the multiple-box 100J or 1 kJ lasers mentioned above. Here we will describe two laser launching systems. The first was a minimal system costing us about $25,000, based on a single-lamp, single-rod Q-switched Nd:YAG laser and a

commercially-available diffusive optical element that produced a top hat beam with grainy substructure. This type of YAG laser, producing 400 mJ in ~8 ns at 1.064 μm, is widely available and is possibly the most economical type of high-energy pulsed solid-state laser. With this system the maximum fluence J = 100 J cm^{-2}. The second was a more expensive but still single-box system costing us about $130,000, based on a multiple-lamp, multiple-rod YAG laser producing 2500 mJ in ~10 ns. With a commercial diffractive optic, we produced a highly uniform beam with maximum fluence J = 500 J cm^{-1}. We wanted to simplify flyer preparation by dispensing with multilayer coatings, single-use sacrificial assemblies, gluing small disks to substrates and so on. For this reason we investigated whether multiple absorption and ablation layers or glued disks were necessary or helpful. We wanted the ability to control shock durations and impact velocities. We wanted these capabilities to be routine so that we could focus our efforts on advanced sample fabrication and advanced spectroscopic techniques.

4.2 Flyer plate launch: basic considerations

The flyer system was designed to produce a nearly planar sustained shock within the probed region, because it is useful to treat the compression process as quasi one-dimensional.[18] To achieve this goal and to determine the required minimum flyer diameter, it is helpful to understand some fundamentals[1,19] of the launch process.

The configuration used for flyer experiments is depicted schematically in Fig. 4.1a. In the usual realization, the flyer is punched by the laser from Al foil glued to a glass window. The top hat launch beam is focused onto the flyer-glass interface, and it is a convergent beam that is somewhat larger at the input face. The flight path is set by a plastic spacer between the flyer surface and the sample surface. Although air resistance is negligible over a < 1 mm flight path,

we typically evacuate the gap because adiabatic compressional heating of air can create an unwanted light flash when the flyer strikes the sample.

The flyer is launched by the expansion of a plasma created at the flyer-glue interface. The plasma generating process has been treated in detail by other authors,[19] so just a bare outline is needed here. The Al foil is originally a mirror surface that reflects 92% of the laser beam. The remaining 8% is absorbed in a skin layer a few nm deep, but the actual depth of the laser-heated region with 10 ns pulses is determined by the distance[20] $\Lambda_{th} = (1/2)(2Dt)^{1/2}$. Heat diffuses during the pulse, where D, the thermal diffusivity of Al is ~1 $cm^2\ s^{-1}$ so $\Lambda_{th} \approx 0.7$ μm. The Al metal becomes an Al plasma when its temperature is ~10^4K,[19] and at that point the flyer plate surface transitions from highly reflective to highly absorbing.[19] Launch occurs when the plasma generates enough pressure to overcome the cohesive energy needed to punch out the Al disk. Because some of the foil is sacrificed to plasma, the flyer plate disk upon launching is 0.5 μm or more thinner than the original foil, and during flight the disk continues to thin due to plasma erosion.[21] The erosion problem makes it impossible to launch very thin flyers by direct laser drive. Researchers at Osaka University[8] developed a multilayer flyer with a sacrificial ablation layer that generates a shock to launch very thin 0.5 μm flyers which are never exposed to laser pulses. These ultrathin flyers could achieve more than 13 km s^{-1}.

The diagram in Fig. 4.1b is useful to understand the accelerated movement of the flyer plate. An important factor is the ratio of laser pulse duration t_p to τ_{sh}. When $t_p > \tau_{sh}$, the flyer plate is accelerated gradually, but when $t_p < \tau_{sh}$, the irradiated surface accelerates before the impact surface. This launches a shock wave in the disk that reverberates longitudinally between the two faces, causing a drumhead vibration. With this reverberation, it is difficult to know the state of the flyer plate face at the instant it impacts the sample.[3,4] The gradual acceleration

condition is met with 10 ns laser launch pulses when the Al foil is 25 μm or less in thickness. Thicker Al foils such as 50 μm or 75 μm can be launched with 10 ns pulses, but there will be reverberations. We want the flight path to be as short as possible to minimize impact time variations, but long enough to allow these reverberations to damp out.

Ultraconservative shock compression measurements require the shock to be "fully-supported". This means the material velocity U_p should remain constant as the shock front propagates through the sample. For example, with a 50 μm Al flyer where $\tau_{sh} \approx 16$ ns, in a material with a shock velocity $U_s = 4$ km s^{-1}, the sample thickness should not exceed 64 μm. Since it always takes some time for the rarefaction wave to catch up to the shock front, a somewhat greater thickness can be used without much of a sacrifice.

An important factor is plasma escape around the flyer edges during flight, as depicted in Fig. 4.1b. The plasma escape can be viewed as a rarefaction wave in the plasma propagating from the edge of the disk toward its center at the plasma acoustic velocity. This acoustic velocity at initial plasma density is a few km s^{-1} and it drops significantly as the plasma expands.[22] An estimate for the average during the flight is 1 km s^{-1}. Plasma escape reduces the acceleration of the disk edges, so the edges fall behind the center, as illustrated in Fig. 4.1b. For this reason it is important to probe only the flat central region of the disk that the plasma rarefaction waves have not yet reached. We found that the drumhead motions of the flyers damped out nicely after a 250 μm flight (*c.f.* Fig. 4.4). With a 170 ns flight time, for example (*c.f.* Fig. 4.10b), the diameter of the flat central region would be 340 μm smaller than the disk diameter.

But there is another factor at work, namely the need to probe a planar shock compression process. When the flyer impacts the sample, the shock in the sample will undergo transverse unloading caused by rarefaction waves moving inward from the edges, except in this case the

waves are moving through the condensed matter sample at speeds in the 4 km/s range. The longest-duration shocks generated in our apparatus are 25 ns, so the probed region should be more than 100 μm from the edges of the flyer plate planar region.

Based on these considerations, and given a flight path of 250 μm, the minimum flyer diameter should be no less than 540 μm plus the diameter of the probed region. Here the flyers were ~700 μm in diameter and the region of planar shock compression is estimated to be 160 μm in diameter. In our experiments we probed regions 100 μm or less in diameter.

This discussion also provides some insights into the conversion efficiency for flyer launch. Computing the flyer plate energy depends on knowledge of the flyer plate mass, and the mass erodes away during launch and during flight. Therefore it would be easy to overestimate the flyer mass with thin flyers. The efficiency would be expected to increase with increasing flyer diameter and flight paths.[23] The plasma takes longer to escape larger diameter flyers so it can continue to accelerate the flyer plate over a longer flight path.

4.3 Smaller laser launcher and diffusive beam shaping

The launch lasers have complex multimode beam shapes. An oversimplified but useful way of dealing with such beams is to define an M^2 parameter. If D is the diameter of the beam on a focusing lens and d is the focused beam diameter, then

$$d = 4M^2 f\lambda/\pi D \qquad (1)$$

For the lowest-order Gaussian beam, $M^2 = 1$, so M^2 can be thought of as the ratio of the multimode focused beam diameter to the diameter produced by a hypothetical perfect Gaussian beam. Lasers with large M^2 cannot be focused to small spots.

The smaller launch system, depicted schematically in Fig. 4.1c, consisted of a Continuum Surelite II-10 laser producing 400 mJ pulses, 8 ns in duration, at 10 Hz. The output beam (Fig. 4.2a) was described by the manufacturer as having a 30% deviation from Gaussian, and its diameter ($1/e^2$ points) was 6 mm. Our measurements, using beam profiling instrumentation from Spiricon, showed that $M^2 = 2.4$. The beam was shaped with an optical diffuser from Holo/Or Ltd., model RD-204-I-Y-A. As we understand it, this diffuser has a large number of small features that scatter tiny parts of the beam at small angles $\leq 2°$ such that the angular distribution is close to the Airy function needed to focus to a top hat beam. After the diffuser we used a bestform aspheric objective lens with a 7.5 cm focal length (CVI BFPL-25.4-75.0-C-1064) to produce a 700 μm spot. With this lens the maximum fluence available was ~100 J cm^{-2}. The focused beam diameter can be increased or decreased using longer or shorter focal length lenses, but a bestform aspheric objective lens is recommended. Figure 4.2b shows the top hat beam profile has sharp edges but a grainy speckle pattern with a depth of modulation of ~15%. The top hat shape was not very sensitive to the diffuser alignment, but by translating and rotating the diffuser the speckle pattern could be varied and made somewhat more uniform.

4.4 Larger launch laser and diffractive beam shaper

Working with the smaller laser, we began to understand that the speckle pattern could be smoother and less prominent if the beam had a larger M^2 value. We discussed this with the provider of our diffractive optic, Silios, Inc., and their data indicated that the smoothness of the focused beam would be greatly improved as M^2 increased. Our laser provider, Spectra-Physics, indicated to us that they could increase the M^2 of an oscillator/amplifier laser using a stable resonator rather than the usual unstable resonator. For the larger launch system depicted in Fig.

4.1d, we used a Quanta Ray Pro-350 laser with $M^2 = 30$. Due to the high energy of the system and the possibility that the flyer could reflect damaging beam energy back into the laser cavity, a 20 mm aperture Faraday Isolator (Electro Optics Technology, Inc.) was used. The laser stability degrades if the laser is not run constantly at 10 Hz, so a high-power shutter (NM laser LSTXYW8-1) was used that had a combined opening and closing time less than 0.1 s. The Silios diffractive optic was a thin silica disk 80 mm in diameter etched to produce many much smaller diffractive elements. Each element, when illuminated uniformly, was designed to produce a top hat shape in the first-order diffracted spot. The diffracted spots from each element would all overlap at a common location. When the entire disk was illuminated by a large diameter (60 mm) nonuniform beam, the beam at each small element would be approximately uniform, resulting in a large number of spatially-overlapping top hat beams at the flyer surface. With a laser of this type, the beam profile changes with time throughout the 10 ns pulse, but that simply causes a time-dependent redistribution of intensities among the small diffractive elements. As long as the beam on each element is approximately uniform, the final beam profile will remain a top hat at different times during the pulse.

To use this optic, the 12 mm output beam, which was nonuniform with two prominent hotspots (Fig. 4.2c), was expanded to 60 mm with a telescope composed of one concave lens and one 75 mm diameter convex lens. After the optic, the diffracted beam was focused on target with a 75 mm diameter aspheric objective lens having a focal length of 150 mm (Thorlabs AL75150), to produce a focused spot 700 μm in diameter shown in Fig. 4.2d. The focused top hat beam is highly uniform, to better than ±5%. As with the diffusive optic, the focused beam diameter can be varied with different focal length objective lenses, and aspheric objectives are

recommended. With this system we can put 500 J cm^{-2} on target, and in addition the drive beam has a high convergence angle, which as shown in Section 4.7 is a useful feature.

4.5 Photonic Doppler velocimetry

A PDV is an optical interferometer where the flyer plate is a moving mirror with a relatively low-quality reflective surface.[5,11,24] A flyer launch generates a time-dependent signal, or interferogram, due to optical interference between a reference beam and a Doppler-shifted reflection. With a 1.55 μm laser wavelength, the relationship between the optical beat frequency and velocity is,[12]

velocity (km/s) = 0.775 x frequency (GHz). (2)

The interferogram can be analyzed in several ways to obtain a velocity history. One common method is a moving-window Fourier transform to determine the beat frequency over a given time interval.[11] During flight, the reflectivity of the flyer can vary a great deal. The Fourier transform method of determining the frequency is relatively unaffected by amplitude variations caused by reflectivity variations.

Our fiberoptic 1.55 μm, 8 GHz PDV system, composed of mostly telecommunications components, has been described previously[25,26] and is depicted schematically in Fig. 4.3. It was based on the design of Weng et al.[12] We made two significant modifications to the Weng design. Instead of using a bare FC/APC fiber as the probe optic, we used a collimating lens and an objective lens[11] to focus the 1.55 μm laser light onto the flyer plate and to collect the reflected/scattered light. Following a suggestion of Weng,[12] we added a 17dBm C-Band in-line fiber amplifier (Optilab LLC, Phoenix, AZ, model AEDFA-C-17I-B) to increase the intensity of the Doppler-shifted signal, and a fiberoptic timing coil to approximately match the signal and

reference arms. Using an 8 GHz digital oscilloscope and 12 GHz photodetectors, the system bandwidth was 6.7 GHz, so velocities up to ~5 km/s can be measured.

The interferogram was recorded by a digital oscilloscope (Tektronix DPO70804) with a long (10MB) record length. Some example PDV interferograms and corresponding moving-window Fourier transforms are shown in Fig. 4.4. The flyers were 25 and 75 μm Al foils launched across an ~250 μm gap to impact a glass window. The PDV probe consisted of a collimating lens and a focusing lens that created a 100 μm diameter beam with a depth of focus (confocal parameter) of 1 cm. The flyers accelerate rapidly during the first 10 ns or so followed by a more gradual acceleration due to continued plasma expansion. The drumhead beating of the flyer surface is prominent with 75 μm foils. However with a 250 μm gap, the beating decays away prior to impact. At impact, there is a sudden deceleration. The magnitude of the velocity reduction is a function of the shock impedance of the flyer and target materials.[27] The reduced velocity is the velocity of the flyer plate/target interface, which is the so-called "particle velocity" U_p. The shock generated by flyer plate impact is viewed as steady as long as U_p remains constant. The duration of the steady shock is ~8 ns with the 25 μm foil, and about 25 ns with the 75 μm foil. At the end of the steady shock, the flyer, now deeply embedded in the glass window,[28] comes to a complete stop and sometimes bounces off the glass.

In Fig. 4.4a, the Fourier transform was performed with a 20 MHz bandwidth. This smoothes the velocity history at the cost of time resolution, but it gives the flyer velocity prior to impact with higher fidelity. In Fig. 4.4b, a 200 MHz bandwidth was used. The flight history is noisier but the impact deceleration and the steady progress at U_p are seen more accurately. Figure 4.4c shows the 200 MHz bandwidth trajectory of a 75 μm flyer that produces an ~25 ns steady shock.

For simultaneous PDV and spectroscopy measurements, we used a high numerical aperture microscope objective to collect light and focus the PDV probe light. We tried several microscope objectives, which collected visible light equally well but which gave varying results with the PDV. We had the most success with a Nikon LU Plan Fluor 10x/0.30 with a working distance of 17.5 mm. Figure 4.4d shows a PDV result with this objective. Because it focuses the PDV beam tightly, and the depth of focus is small, good signals are obtained over only ~1/3 of the flight path and the objective must be carefully focused onto the impact region.

4.6 Flyers with the smaller launch laser

The smaller laser was used to launch 700 μm diameter, 25 μm thick Al foils weighing 25 μg, glued with Eccobond 24 epoxy to 0.8 mm thick glass substrates. The results are shown in Fig. 4.5. The highest velocity we achieved was 1.8 km/s and disappointingly, above 50 J cm^{-2} the flyer velocities actually decreased. The 1.8 km/s flyer launched at 40 J cm^{-2} (E_p = 150 mJ) had a kinetic energy of ~40 mJ and the efficiency was 26%, or perhaps a bit less accounting for flyer erosion. In order to understand what was happening above 40 J cm^{-2}, we measured the ratio of fluence transmitted through the substrates versus input fluence, as shown in Fig. 4.6. Above 40 J cm^{-2} the ratio leveled off and became erratic. This phenomenon falls under the general rubric of "optical self-limiting". Examination of the windows revealed self-limiting was primarily the result of optical damage on the window output face (the face opposite the input face where the foil normally is attached). Nothing we tried allowed us to achieve a transmitted fluence much greater than 60 J cm^{-2} (230 mJ) at the flyer/substrate interface. We tried an extended laser cavity that stretched the pulses to 15 ns, and we tried a variety of different substrate materials, substrate thicknesses and focusing objectives, but without any noticeable

improvement. We could not launch these flyers above 1.8 km s^{-1}. However since the velocity stops increasing above 50 J cm^{-2}, and we had 100 J cm^{-1} available, we assume we could use a longer focal length objective to double the area of the focused spot, and launch flyers with √2 larger diameter and twice the kinetic energy.

4.7 Flyers with the larger laser launcher

While both laser launchers produced 700 μm spots at the flyer surface, the beam from the larger laser has fewer hot spots and a convergence angle (60 mm diameter, 150 mm focal length objective) that is five times greater than the beam from the smaller laser (6 mm diameter, 75 mm focal length objective). These different beam parameters and the thickness of the substrate should change the way the beam interacts with the easily-damaged output face. Figure 4.7 shows the results from launching 50 μm thick Al flyers with Eccobond 24 epoxy using the larger laser, with substrates 1.59 mm, 6.35 mm, and 16 mm thick, and the results are dramatic. The maximum velocity achievable with the 3.2 mm substrate was 1.2 km s^{-1}, 2.6 km s^{-1} with the 6.35 mm substrate, and 2.0 km s^{-1} with the 16 mm substrate. So subsequently we used only 6.35 mm thick substrates. At the highest fluences we could input, ~500 J/cm^2 (~2000 mJ pulses), the maximum transmitted fluence we could achieve with these substrates was 375 J cm^{-2} (1400 mJ).

The maximum attainable flyer speed with the larger laser varied from glass substrate to substrate in a seemingly random manner. It was probably variability in the glass and in the glue. With the 25 μm foils, the worst windows gave launch speeds up to 3.5 km s^{-1}, and in the best case we achieved 4.5 km s^{-1}. Results obtained in one of these "best cases" with the larger laser using 25, 50 and 75 μm Al foils are shown in Fig. 4.8. The 25 μm foils were accelerated to 4.5 km/s when J = 500 J cm^{-2}. The kinetic energy of these flyers was estimated to be 250 mJ. Since

the launch pulse energy was 1900 mJ, the efficiency was 13%. The reasons for this seemingly low efficiency are the laser energy lost by the self-limiting effect, and the relatively small flyer diameter and short flyer flight path.

One undesirable feature seen in Fig. 4.8 was our inability to launch the 25 μm flyers below 1.8 km/s. When the fluence was reduced below 50 J cm^{-2}, the flyers would not detach from the substrate. Presumably in this case the cohesive energy needed to punch out the flyer became comparable to the laser energy imparted to the flyer. To test this hypothesis, we launched 25 μm flyers that were 700 μm disks cut away from the surrounding foil. Although some researchers used foil disks glued to substrates,[3,23] making and gluing a number of 700 μm diameter foil disks seemed too complicated, so we devised a method that was simpler for us to implement. Starting from Al foil epoxied to glass, a computer-controlled Hansvelt wire electrical-discharge machining (EDM) system was used to erode an array of annular regions in the foil to create an array of 700 μm diameter Al reliefs, as shown in Fig. 4.9. At higher fluences > 100 J cm^{-2}, there was no difference between the foil and the reliefs, presumably because in this range the cohesive energy was inconsequential. However the reliefs were readily launched at low velocities down to 0.1 km s^{-1}. So the additional complexity of the EDM relief fab technique need be used only for lower-velocity impact experiments.

In order to test the consistency of the flyer launch, we launched 33 shots one afternoon from a 5 x 5 cm^2 substrate with 25 μm foil. We measured the flight time across a 250 μm gap and the velocity just prior to collision with a glass window. The flight time was measured with a photodiode to monitor the launching pulse and a photomultiplier to monitor the light flash caused by disk-window impact. The variance in flight time is a critical parameter needed to determine how well instrumentation such as streak cameras can be synchronized with flyer impacts. Figure

10 shows our results. Two shots were outliers whose speeds were ~5% below average, probably due to a tiny bubble in the epoxy. If we ignore these two shots, the velocity was 3.29 ± 0.02 km s^{-1} and the flight time was 168 ± 1.0 ns, where the error bounds were one standard deviation. These results provide support for a description of these methods as simplified, reliable and capable of launching tens of shots per day.

4.8 Effects of absorption and ablation layers

In the results reported above, the flyer plate assembly was simply a foil epoxied to a window. Other researchers have deployed more or less elaborate launching layers between the substrate and the flyer plate. Stahl and co-workers used a thin C layer.[17] The C was said to help homogenize the drive laser beam, and lighter C atoms may provide greater specific impulse than Al. Greenaway and co-workers[7] used an energetic ablation layer of unspecified composition that provided significant velocity increases at fluences near 5 J cm^{-2}. Bowden and co-workers[5] studied the effects of launching flyers with fluences in the 5-40 J cm^{-2} range having C or Ti absorption layers, and C, Mg, Ge, Al or Ti ablation layers. The best of these combinations was about 20% better than the worst.

We tried increasing the flyer laser absorption in two ways. We created a carbon black nitrocellulose layer that was strongly absorbing and energetic. We also evaporated a thin (100 nm) layer of Cr on the Al foil, since Cr absorbs nearly 50% of incident near-IR light compared to 8% for Al.[29] There was no noticeable improvement from these layers when flyers were launched with fluences >50 J cm^{-2}. This makes sense since with Al, the 10 ns fluence needed to produce an absorbing plasma is less than 1 J cm^{-2}, so absorbing layers are unlikely to significantly boost flyer kinetic energies except possibly at lower fluences in the 10 J cm^{-2} range.[5,30] We also

compared two low-viscosity glues that made thin strong bonds between metal and glass, the UV-curable acrylic adhesive Dymax 401 (Dymax) and a water-clear epoxy Eccobond 24 (Emerson and Cummings). Acrylic adhesives are known to significantly boost near-IR ablation processes even more so than nitrocellulose, at low fluences of ~0.5 J cm^{-2}.[31] As shown in Fig. 4.11 the launch at fluences >20 J cm^{-2} was no different with these two glues. Again this makes sense since there is simply not enough energy in glue to have much effect at these fluences. With a 700 μm diameter flyer plate and a 1 μm thick glue layer, the glue would be less than 1 μg. Even if the glue produced the energy of detonating TNT (8 kJ cm^{-3}), the extra energy would be just 3 mJ.

We concluded that with our launch system, absorber or ablation underlayers were ineffective in increasing launch kinetic energy and only added complexity. Whatever effects these layers may have in mitigating the problems associated with inhomogeneous laser beam profiles were minimal with the beams used here. We note that the cases where underlayers were reported to have significant effects involved flyers launched by beams homogenized in optical fibers.[5,7] Optical damage to the fiber surfaces limits the fluences to <40 J cm^{-2},[30] so added absorber or ablation underlayers appear to be useful only at lower launch fluences. We find it is helpful to use a glue with strong adhesion to the foil and substrate. Otherwise when a flyer is punched from the foil it will lift up some of the surrounding foil, which limits the number of flyers that can be launched from a given substrate. However glue adhesion should have no effect on the flyer launch because the launch laser vaporizes Al at the Al-glue interface, destroying the Al-glue adhesion. After working with the epoxy and acrylic adhesives for a while we decided that the epoxy ultimately seemed to produce better adhesion, a smoother layer and a stronger bond; however, the UV glue was simpler and quicker.

4.9 Hugoniot equation of state

Measuring equations of state is a challenge with laser-driven flyer plates[3] because the shock durations are short. Usually this problem is approached using large laser facilities such as the Trident laser,[3] that generate microsecond-duration kilojoule pulses. Using our smaller launch laser, we developed a method to measure EOS with thin transparent samples, and demonstrated the method with a solvent-cast poly-methyl methacrylate (PMMA) film,[26] where the shock duration was 8 ns and the particle velocity range was U_p = 0.4-1.0 km s^{-1}. The accuracy of the method improves with longer-duration shocks and a larger range of U_p. Here we present new data obtained using our larger launch laser, where the shock duration was 16 ns and the particle velocity range was U_p = 0.5-2.0 km s^{-1}.

A Hugoniot EOS for PMMA was previously obtained using a gas gun facility at Los Alamos,[32,33] but the EOS of a polymer may depend on the method of preparation and the shock duration. The Los Alamos measurements used a PMMA disk 16 cm in diameter and 2.5 cm thick that was cut from a commercially-available slab produced by polymerization of the monomer in a mold.[33] The measurements reported here used a film created by spin coating a PMMA solution, so the density, composition and polymer conformation may be different, and there might be trapped solvent. The polymer film EOS results support the spectroscopy results in the next section.

The principal Hugoniot of a material is described by the relationship between two parameters of single-stage shock compression.[32] The Rankine-Hugoniot equations show that any two of shock velocity, material velocity, pressure, density, energy or enthalpy could be used to characterize the Hugoniot. Frequently Hugoniot data is presented as a linear relation, U_s =

$mU_p + b$.[32] Measuring m and b allows us to determine the shock pressure and density from a PDV measurement of U_p.[32] Our method for measuring both U_s and U_p of materials that are reasonably transparent to near-IR 1.55 μm light used by PDV, which was designed to mitigate the short-duration shock problem, is described schematically in Fig. 4.12. Using PDV, we determined U_p as the speed of the flyer plate after it impacted PMMA, and U_s as the shock transit time across PMMA divided by the measured PMMA thickness d. The shock transit time was the time interval between the impact time t_1 and the shock arrival time t_2 at the semitransparent ultrathin Au mirror.

The accuracy of these measurements improves the more time we have to measure U_p and U_s. Additionally we want these measurements to result from "single-stage" shocks that are close to fully-supported. There could be significant shock reflections at a polymer/glass interface, so to achieve single-stage compression we delayed these reflections by ~20 ns by adding 30 μm cushion layers of poly-vinyl alcohol (PVA), a good impedance match to PMMA. The fully-supported condition with 50 μm Al flyers was realized with the d = 57 μm thickness used here when $U_s \geq 3.5$ km s^{-1}. A few of our measurements refer to $U_s \approx 3$ km/s, where the shock was quite close to being fully-supported.

The PVA layer was drop-coated onto glass from a 5% aqueous solution and then baked at 50°C to create cross-links. The ultrathin Au mirror was evaporated onto PVA by electron-beam deposition. The PMMA layer was spin-coated onto Au by dissolving PMMA (Aldrich MW > 1 million) in a mixture of ketones which does not readily dissolve cross-linked PVA. The PMMA thickness d was measured with a Dektak profilometer.

The most accurate velocities were obtained using information from both the interferogram and its Fourier transform,[26] as illustrated in Fig. 4.12b. PDV monitored the flyer

plate flights and impacts through the ultrathin mirror. The impact time t_1 was found from the sudden frequency decrease in the interferogram. The material velocity U_p was determined from the Fourier transform of the post-t_1 time interval where U_p remains steady. The shock emergence time t_2 was determined from the sudden increase in interferogram amplitude as the shock passes through the ultrathin mirror. The shock velocity is $U_s = d/(t_2-t_1)$. The process was repeated over a range of flyer impact velocities. The principal Hugoniot so obtained is shown in Fig. 4.13. Our previous results[26] in the 0.5-1 km s^{-1} range showed that our polymer film shock speeds seemed slightly but systematically lower than in the Los Alamos measurements. This is quite possibly caused by residual solvent in the polymer film. The data in Fig. 4.13 also show slightly smaller shock speeds in this lower U_p range, but at higher U_p in the 1-2 km s^{-1} range, our new results are in excellent agreement with the Los Alamos data. So if our supposition is correct, then the effects of residual solvent become less significant at higher impact velocities.

4.10 Time-resolved spectroscopy of dye-doped PMMA

The EOS measurements made with PDV described above provide information about the macroscopic states of shocked materials. Optical spectroscopy of probes embedded within the sample can provide complementary information about the microscopic states. This macro/micro probing method could be especially useful if a sample has microstructure, or if a sample undergoes physical or chemical transformations. In particular it would be useful to have the capabilities of probing local temperatures, pressures and compositions in inhomogeneous materials. We have developed the capabilities for simultaneous PDV and time-resolved spectroscopy, and illustrate them with the example of PMMA doped with rhodamine 640 dye aggregates (R640).[34,35] This dye was chosen because of its high radiative rate and the convenient

locations of its absorption (580 and 540 nm) and emission (615 nm) maxima. In related previous work, Shen and Gupta[36] studied the fluorescence of a similar dye, R6G, in liquid ethanol solution up to 2 GPa, with the intent of establishing dye emission as an internal optical pressure sensor. In the liquid, microstructure was not an issue. Lee and co-workers[35] used picosecond transient absorption spectroscopy to study R640 in PMMA compressed by 4 GPa ps-laser-driven shocks, with the intent of investigating dye multiphonon up-pumping.[37,38] In up-pumping, a steep shock front creates a nonequilibrium vibrational population that relaxes to a thermal distribution in 10-100 ps.[37] On the nanosecond time scale of the present measurements, up-pumping cannot be detected. Some preliminary measurements of dye emission obtained using the smaller launch laser were published previously, but here we present new and greatly-improved results obtained with the larger laser.

The experimental schematic is shown in Fig. 4.14. The samples were 8 μm thick PMMA with 20 mM R640 dye aggregates, and a 30 μm PVA cushion, on a glass substrate. Just prior to impact, the R640 was excited by 250 ns duration, 527 nm pulses from a Q-switched Nd:YLF laser. The excitation pulse intensity was approximately constant during the shock. An optical probe that transmitted the PDV beams and simultaneously collected dye emission was developed. The probe had two dichroic beamsplitters. The first reflected the 1.55 μm PDV light while transmitting the 527 nm excitation light and red dye emission light. The second reflected 527 nm excitation light and transmitted red emission. The dye emission was imaged on a spectrograph with a streak camera (Hamamatsu C4334-01). The vertical spectrograph entrance slit was 50 μm, the horizontal streak camera photocathode slit was 70 μm, the magnification of the relay optics was unity and the spectrograph magnification was 1.2, so the streak camera observed a 40 x 60 μm^2 region at the center of the impact region.[39] A small portion of the

emission was directed onto a photomultiplier (PMT) with subnanosecond response, in order to correlate the shock peak shift with shock intensity changes.

Although it seems reasonable to believe that abrupt changes in the dye emission are caused by flyer plate impact, it is useful to verify this is so. The flyer plate is a mirror with a fluctuating reflectivity that is rapidly approaching the sample, and it could possibly cause the collected emission intensity to vary prior to collision. The emission was detected by a PMT or a streak camera and the collision was detected by the PDV, and each element has its own characteristic optical and electronic delays. It is well known how to synchronize lasers and streak cameras. One simply superimposes a small part of the laser pulse on the same streak as the emission, so that will not be discussed here. To synchronize the PDV with the PMT, which are detected using a common oscilloscope, we used a "vanishing mirror" technique. We replaced the sample with a piece of polyester having a thin mirror Al coating (aluminized Mylar). We disconnected the reference leg of the PDV (Fig. 4.3) so the 1.55 μm beam from the PDV probe was reflected back into the fiberoptic, and was detected by a photodiode. A pulse from the launching laser was used to vaporize the mirror coating. This created a transient in the 1.55 μm beam, denoted "coating ablation" in Fig. 4.15, which occurred during the launch pulse. We inserted a frequency doubling crystal into the laser drive pulses to produce green light that the PMT can detect. The time delay introduced by this crystal was a few picoseconds and inconsequential. Then we synchronized the PMT and PDV by aligning the laser drive pulses with the coating ablation transients. As shown in Fig. 4.15, the PDV record of the moment of impact coincides very well with the onset of the dye emission drop from the sample.

Results from simultaneous PDV and dye emission measurements are summarized in Fig. 4.16. The flyer was 50 μm Al launched at 1.3 km s^{-1}. The value of U_p was 1.1 km s^{-1}, and using

the EOS measurements in the previous section, the pressure was P = 4.8 GPa and the density ρ = 1.63 g cm^{-3}. Increasing the density on solvated dye molecules typically results in redshifted absorption and emission spectra, because the excited state redshifts more than the ground state. When the flyer plate impacts, there is a sudden loss of intensity, as shown in Fig. 4.16, which we attribute to an unobserved redshift of the 540 nm dye absorption to longer wavelength, away from the 527 nm excitation laser. The risetime of this intensity shift, which is ~5 ns, was limited by a combination of the ~2 ns dye emission lifetime and the shock transit time across the sample. The time-dependent emission spectra from the streak camera were analyzed using the method of moments. If the spectrum at any time *t* is $I(\lambda,t)$, then the moments 0-2 are defined as,

$$M^{(0)}(t) = \int_0^\infty I(\lambda,t)d\lambda \quad (3a)$$

$$M^{(1)}(t) = \frac{1}{M^{(0)}(t)}\int_0^\infty \lambda I(\lambda,t)d\lambda \quad (3b)$$

$$M^{(2)}(t) = \left[\frac{1}{M^{(0)}(t)}\int_0^\infty \lambda^2 I(\lambda,t)d\lambda\right]^{\frac{1}{2}} \quad (3c)$$

where $M^{(0)}(t)$ is the instantaneous wavelength-integrated intensity, $M^{(1)}(t)$ is the instantaneous average wavelength, and $M^{(2)}(t)$ is an instantaneous spectral width. The values of these three moments are plotted in Figs. 4.16d-f. The $M^{(0)}$ data should be approximately identical, within a proportionality constant, with the PMT results in Fig. 4.16c, since the PMT observed a wavelength-integrated intensity. The value of $M^{(1)}$ shows an instantaneous shock redshift from 615 nm to 650 nm. The value of $M^{(2)}$ shows an instantaneous shock broadening from a width of 36 nm to 40 nm. Further research in this area will be directed toward interpreting these moments and to developing new spectral probes. It might be possible to relate $M^{(1)}$ to the local density and $M^{(2)}$ to the shock temperature increase.

4.11 Initiation of reactive materials

Previous studies showed that flyer plates could initiate explosive reactions in relatively sensitive energetic materials such as pentaerithritol tetranitrate (PETN)[12] and hexanitrostilbene (HNS).[40] Our intent was to develop a flyer plate system that could initiate less sensitive explosives, especially novel reactive materials (RM) created by nanotechnology,[23] which would let us analyze the spectral and temporal properties of the emission bursts that accompany the ignition process. Initiation refers to the onset of chemical reactivity and ignition to the onset of energy-producing reactions. In the cited prior studies, the emission from the explosives was not analyzed to reveal its spectral or temporal properties. Although there have been prior time-resolved spectroscopy studies of emission from explosive charges,[41-43] in those cases the duration of the emission bursts were determined by the size of the explosive charge and the rate that ignition reactions propagated through the charge. Our intent is to study ignition in the limit where the charge is so small, and the shock transit time so short, that the duration of the emission burst is limited by intrinsic microscopic mechanisms. Figure 4.17 presents an example of a study where the RM was a mixture of Al and Teflon nanoparticles. This is a highly energetic mixture that can produce up to three times as much energy as the equivalent amount of TNT.[39,44-48] In a bit of oversimplification, if Teflon is viewed as a polymer whose subunits are $-CF_2-$, then the energetic chemistry occurs by the reaction,

$$Al + 3/2CF_2 \rightarrow AlF_3 + 3/2C.$$

The Teflon and Al + Teflon samples on glass windows contained 10% PMMA binder. The Teflon samples shown in Figs. 4.17a,b were fabricated by suspending DuPont Zonyl MP1200 particles (mean diameter 3 μm) in a mixture of ketones and PMMA, shaking and sonicating the suspension and then spin coating the mixture on a window. The Teflon + Al

samples shown in Figs. 4.17c,d were fabricated the same way except 120 nm Al nanoparticles (Technanogy, Inc.) were added to the suspension in mass ratio Al:Teflon 1:3.

In using flyer impact for emission spectroscopy, we had several concerns. The Al of the flyer plate might react with the Teflon. Although our thermal diffusion calculations said otherwise, the flyer plate might conduct heat from the launch plasma to the sample, so the sample might experience a combination of impact and heating. The emission spectrum might be contaminated by launch plasma emission or emission from the flyer impact. With our flyer plate system, it is easy to protect against these eventualities. For instance we could place a heat insulating layer of thin polyethylene film over the sample (e.g. kitchen plastic wrap), or an opaque foil light guard such as 10 μm Al or Ta. However we found these measures were not needed when we made the samples thick enough to be opaque, since in that case only the sample-window interface was seen by the spectrometer.

As seen in Fig. 4.17b, after 25 μm flyers were shot at 3 km s^{-1} into Teflon (Fig. 4.17a), a depression surrounded by black material was produced. The black material is presumably C, and indicates extensive Teflon decomposition. After flyers were shot at 3 km s^{-1} into Al + Teflon (Fig. 4.17c), an audible explosion took place and larger craters and more damage to the surrounding material was seen (Fig. 4.17d). Figure 17e shows the time-dependent emission intensities created by the flyer impact, as detected by a PMT. The Teflon emission lasted ~100 ns. The Al + Teflon emission was much more intense, it had a prominent delayed emission burst, and it lasted ~3 μs. Figure 4.17f shows emission spectra obtained using a spectrograph and a gated CCD detector set to probe a 100 ns wide window near the time of the emission maxima. The emission was broad, and superimposed on the emission were some molecular emission and absorption bands that, due to their sharpness, probably originate from gas-phase

species such as C_2. These time-resolved spectra are consistent with the idea that impact ignition occurs by first decomposing the Teflon on the 100 ns time scale, and on the few microsecond time scale the fluorine from the decomposed polymer attacks the Al particles.

4.12 Summary and conclusions

The laser-driven flyer plate literature describes a variety of techniques, some using a laser the size of a shoebox, and some using a laser the size of a building, flyer plates launched from a bare piece of Al foil or multilayer assemblies with hand-made individual disks. In order to bring some clarity to the subject, we proposed that the most important factor is the laser fluence J on the flyer plate surface. Considerations related to plasma drive, launch instabilities, flight path and duration of the planar shock mandate a minimum value for the flight path and the flyer plate diameter. Given this minimum diameter, the available laser pulse energy E_p determines the maximum fluence at the target, and optical damage of the flyer plate substrate determines the maximum fluence on the flyer surface. With our system we have determined that a 250 μm flight path is enough for the flyer to stabilize during flight, and a 700 μm diameter flyer ($A = 4 \times 10^{-3}$ cm^2) will deliver a planar shock to a 100-200 μm diameter central region that can be conveniently probed by PDV or optical spectroscopy.

Here we described two laser launch systems, a smaller 400 mJ system, where the laser was 17 x 78 cm^2, producing a maximum fluence of 100 J cm^{-2}, and a maximum fluence on the flyer surface of 60 J cm^{-2}, and a larger 2500 mJ system where the laser was 20 x 117 cm^2, producing a maximum fluence of 500 J cm^{-2}, and a maximum fluence on the flyer surface of 375 J cm^{-2}. With the smaller system the maximum flyer kinetic energy was 40 mJ at a velocity of 1.8 km s^{-1}, but we believe that if we increased the laser energy to its maximum rated value (600 mJ)

and expanded the beam on the flyer surface, we could achieve 100 mJ flyer energies. With the larger system having a different convergence angle and a smoother profile with an optimized substrate thickness of 6.35 mm, the maximum flyer kinetic energy was 250 mJ at a velocity of 4.5 km s^{-1}.

It is possible to launch flyers at higher fluences by eliminating the substrate. The efficiency decreases because the substrate helps confine the plasma.[19] He et al. launched substrate-free 10 μm flyers at a fluence of 1 kJ cm^{-2} with a kinetic energy we estimate to be 5J, using 100J laser pulses, for a net efficiency of 5%.[14] Despite the undesirable optical self-limiting of the substrate, the substrate creates a flat, mechanically stable platform that a freestanding foil cannot, and we did not think we could accurately control the flight path and impact time using a freestanding thin foil.

With the larger launch laser and its diffractive optic, we generated an exceptionally smooth top hat beam with much greater fluences than are possible with fiberoptic[5,7,30,49] methods. We can launch tens of flyers from a single foil/substrate unit with high reproducibility. If we throw out the occasional (about 1 in 15) bad shot that is 5% below average, the fluctuation in velocity or arrival time was 0.5%, and the variance in arrival time, a critical factor in time-resolved spectroscopy measurements, was 1.0 ns.

The usefulness and potential of this system was demonstrated by measuring a Hugoniot EOS of a polymer film, measuring the time-dependent shocked emission of a dye in the polymer film, and measuring the time-dependent emission from an impact-initiated nanoparticle RM. Even a single shot emission measurement generated a significant amount of useful data regarding the shock-induced changes in intensity, peak shift and peak width, which were analyzed by the method of moments. These techniques should be extremely valuable for the

development of new optical diagnostics of microscopic states of shocked materials. The ability to shock-initiate and detect emission from nanoparticle RM should be extremely valuable for studies of fundamental mechanisms of these materials, which have generated a great deal of excitement in the energetic materials community, and which are available in a myriad of compositions and formulations.

4.13 Figures

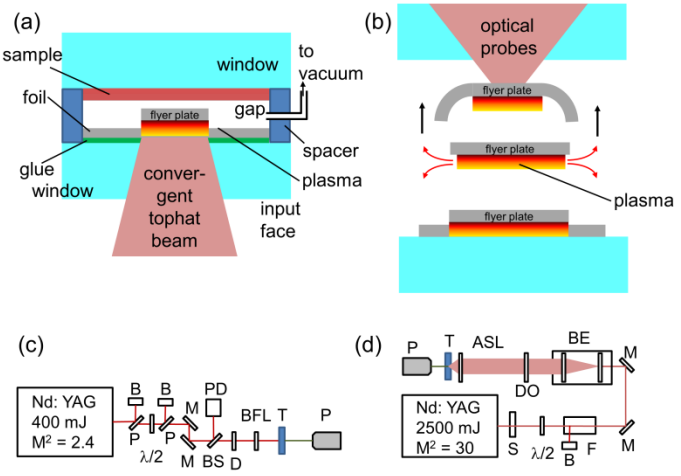

Figure 4.1: (a) Schematic of flyer assembly, not drawn to scale. The windows are 5 x 5 cm^2 and 6.35 mm thick, the foil is 25, 50 or 75 μm thick, the gap is 250 μm and the focused beam diameter is 700 μm. (b) During flight, the driving plasma leaks out from the edges causing the flyer plate edges to lag behind the plate center. Optical probes observe the flat, central 100-200 μm of the plate. (c) Schematic of smaller laser launcher. (d) Schematic of larger laser launcher. Key: S = shutter; P = polarizing beam splitter, λ/2 = half-wave plate, B = beam block; M = mirror, PD = photodiode, BS = beamsplitter, D = diffuser, BFL = best-form lens, T = target; P = probe, F = Faraday isolator, BE = beam expander, DO = diffractive optic, ASL = aspheric lens. Courtesy of Dana Dlott.

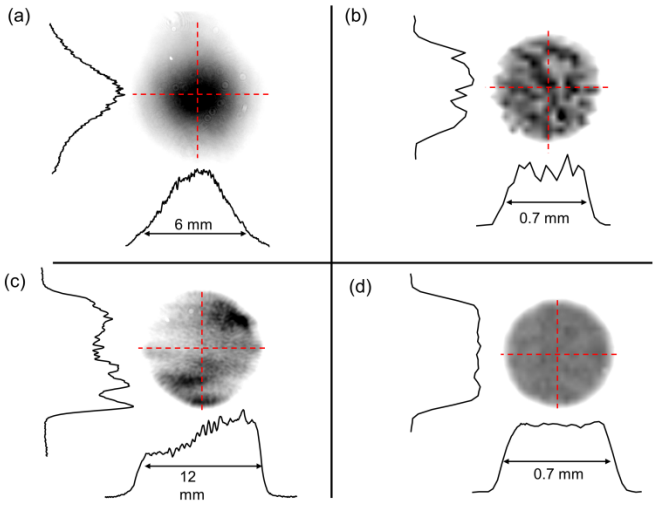

Figure 4.2: Beam profiles. (a) Smaller launch laser output "near-Gaussian" beam. (b) Smaller laser beam after diffuser and focusing objective. (c) Larger launch laser output. (d) Larger laser after diffractive optic and focusing objective.

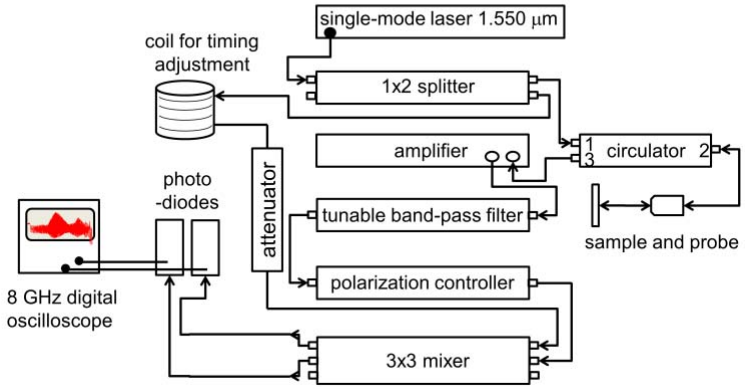

Figure 4.3: Schematic for Photonic Doppler Velocimeter (PDV). Courtesy of William Shaw.

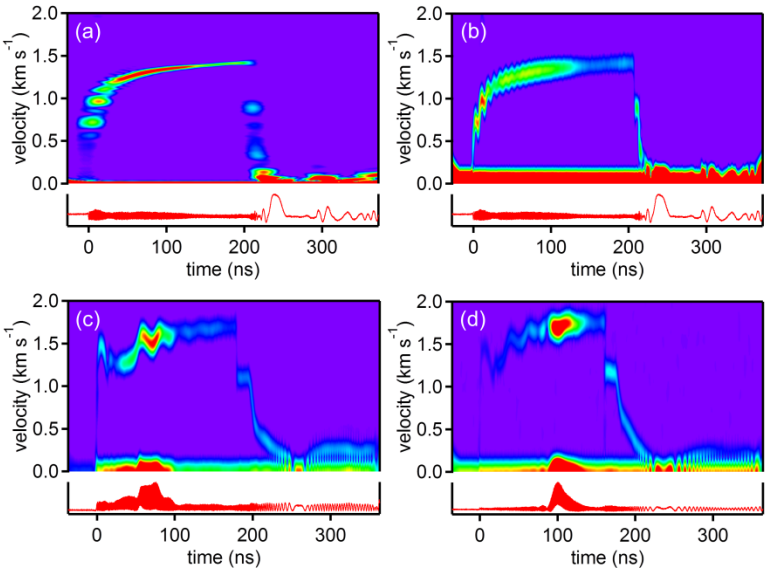

Figure 4.4: Velocity histories obtained by PDV for Al flyers launched by 10 ns pulses across a 250 μm gap onto a glass window. The bottom pane is the interferogram and the top pane the moving-window Fourier transform. The sudden acceleration coincides with the drive laser pulse, and the sudden deceleration with window impact. The brief period of constant velocity immediately after impact gives the material velocity U_p and the shock duration. (a) 25 μm thick with Fourier transform using a 20 MHz filter gives accurate flight velocity; (b) Same as (a) using a 200 MHz filter is noisier, but more accurately records the impact and the ~8 ns steady shock. (c) With a 75 μm thick flyer the drumhead ringing damps away prior to impact. (d) A 75 μm thick flyer observed with a microscope objective that permits simultaneous PDV and emission collection. The PDV beam has a shallow depth of focus, so the PDV signal is more intense as the flyer approaches the window. Courtesy of William Shaw.

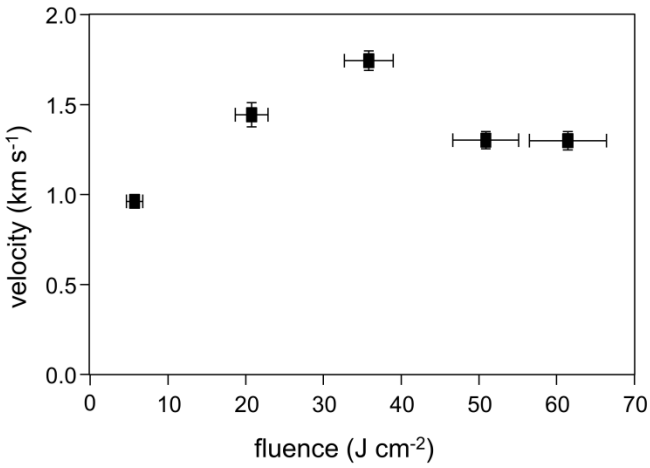

Figure 4.5: Velocities of 700 μm diameter, 25 μm thick Al flyers launched with the smaller laser. The velocity stops increasing above 40 J cm^{-2} due to optical damage on the output faces of the glass substrates.

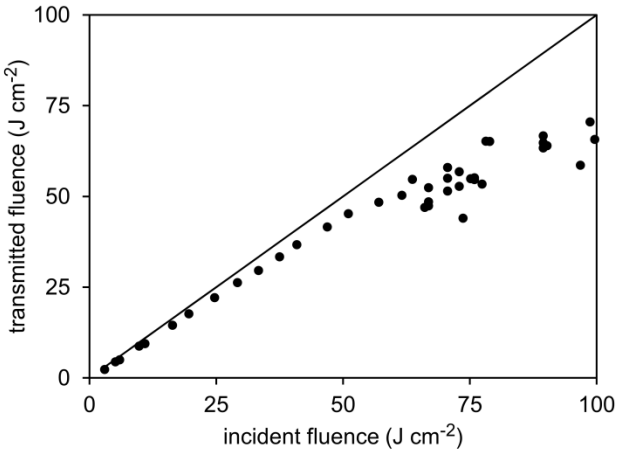

Figure 4.6: Ratio of laser pulse fluence incident on and transmitted by a 1.6 mm thick glass window using the smaller laser launcher. Above 40 J cm^{-2} the window transmission decreases due to optical damage. Courtesy of William Shaw.

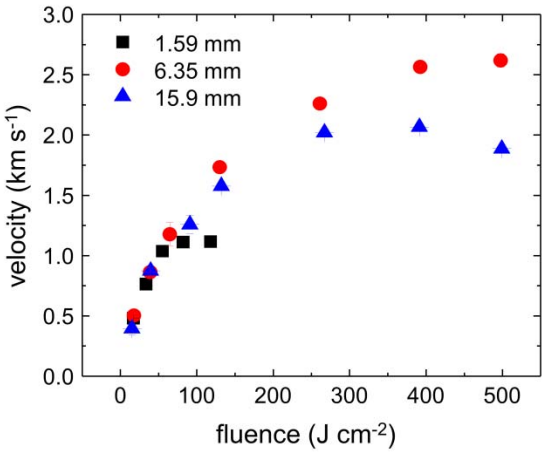

Figure 4.7: Velocities of 25 μm Al flyers using the larger launch laser with different glass substrate thicknesses. The 6.35 mm substrates gave the highest velocities. Courtesy of William Shaw.

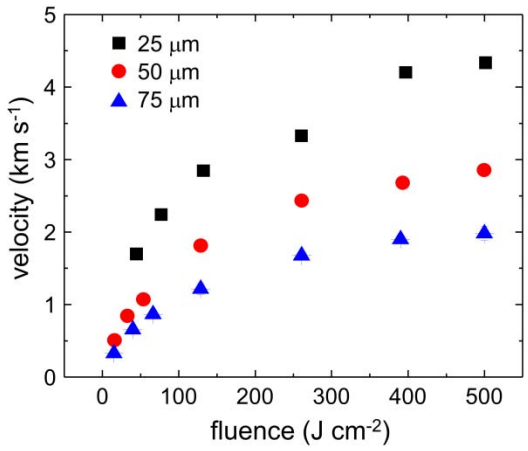

Figure 4.8: Velocities of different thickness Al flyers using the larger launch laser. At the highest incident fluence of 500 J cm^{-2}, the fluence transmitted through the 6.35 mm thick glass window was about 375 J cm^{-2}.

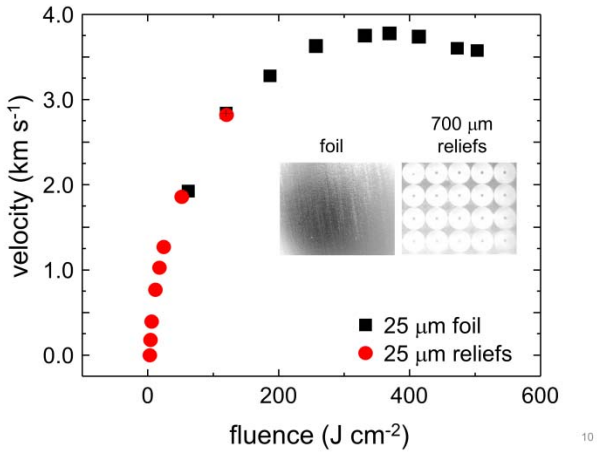

Figure 4.9: When 25 μm Al flyers were punched out of a foil by the laser pulses, the flyers did not detach or fly well below 2 km s^{-1}. When electrical-discharge machining (EDM) was used to etch away annual regions leaving behind discrete 700 μm flyer disks (reliefs), those disks could be launched at lower velocities. At higher velocities the foil punch-out and the reliefs worked equally well. Courtesy of William Shaw.

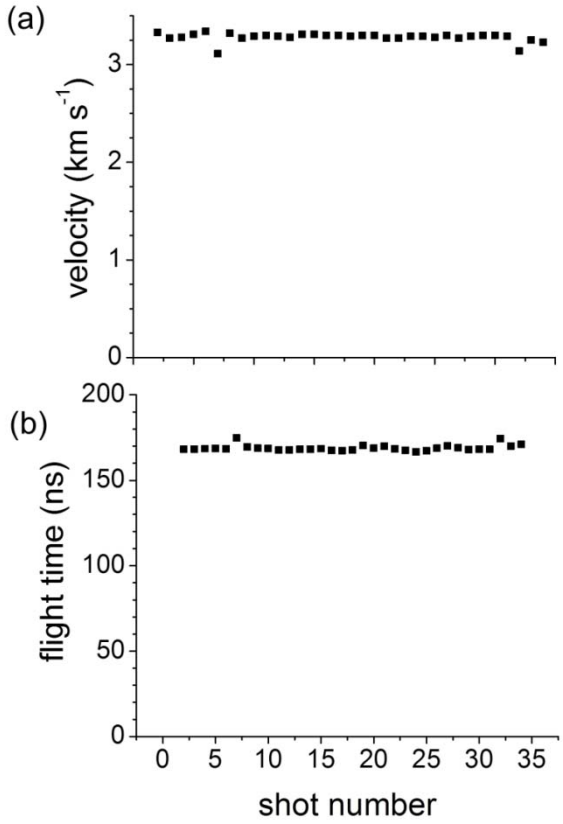

Figure 4.10: Results from a consistency test where 33 flyers were launched from a 25 μm Al foil epoxied to a 5 x 5 cm^2 glass substrate. (a) Velocity. (b) Flight time across a 250 μm gap, defined as the interval between the laser launch pulse and the flyer impact with a window. Two of the shots were 5% outliers, presumably due to small bubbles in the glue. With the remaining 31 shots, the average velocity was 3.29 ± 0.02 km s^{-1} and the flight time was 168 ± 1.0 ns, where the error bounds were one standard deviation. Courtesy of William Shaw

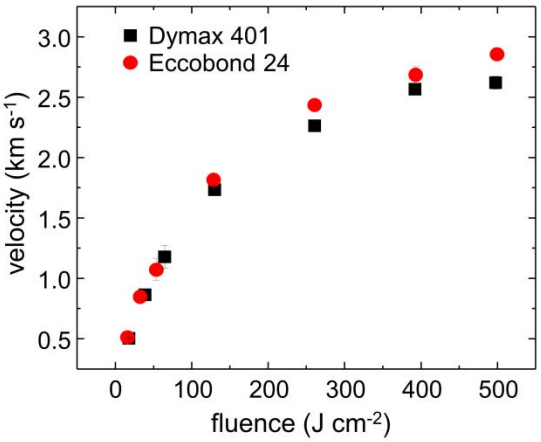

Figure 4.11: Two different kinds of glue, a UV-curable acrylic (Dymax 401) and a thermosetting epoxy (Eccobond 24) yielded the same 25 μm Al flyer launch results with the larger launch laser.

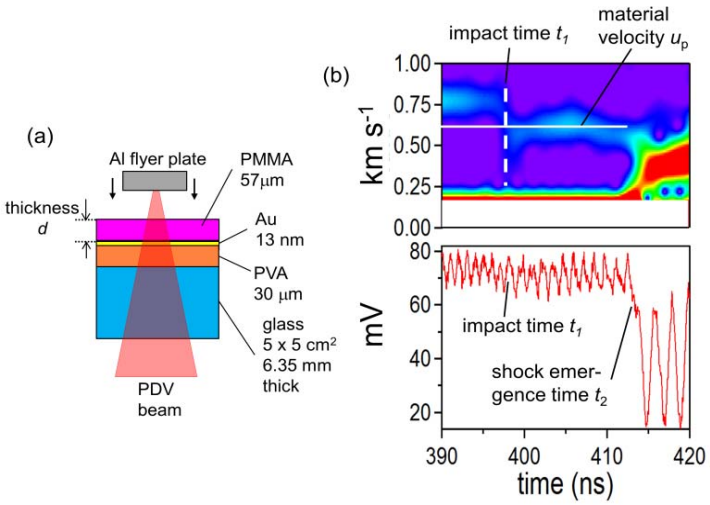

Figure 4.12: (a) Schematic of sample arrangement for PMMA Hugoniot measurements using the method of ref. 26. PVA is a cushion layer that prevents shock reflections from glass as the shock exits PMMA and passes through the semitransparent Au mirror. PDV monitors the flyer plate through the Au mirror to determine the flyer velocity after impact U_p, the flyer impact time t_1, and the shock front emergence time t_2. The shock velocity $U_s = (t_2\text{-}t_1)/d$. (b) PDV interferogram and its moving-window Fourier transform showing how the values of U_p, t_1 and t_2 were determined. Courtesy of William Shaw.

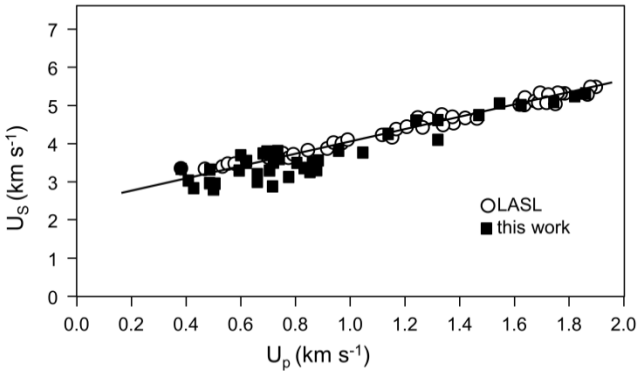

Figure 4.13: Hugoniot measurement for 57 μm thick solvent-cast PMMA using laser-driven flyer plates, compared to results from the Los Alamos (LASL) database. The line is a visual guide.

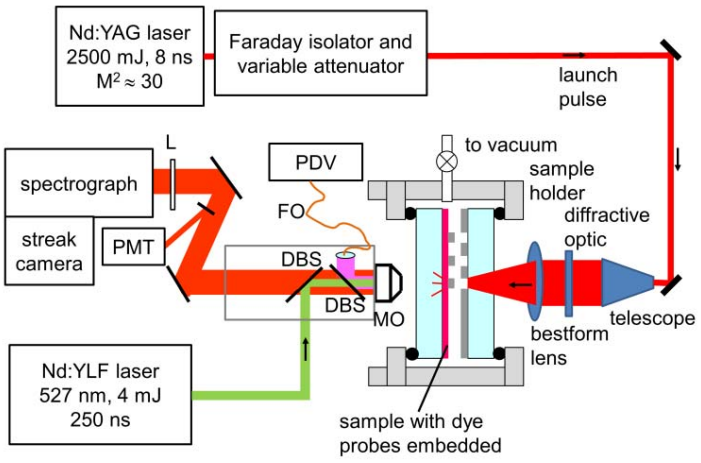

Figure 4.14: Schematic for simultaneous PDV measurement of flyer plate impact and observation of time-resolved emission of a dye embedded in a sample. Key: FO = fiberoptic cable; DBS = dichroic beam splitter; L = achromatic lens, MO = microscope objective; PMT = photomultiplier tube.

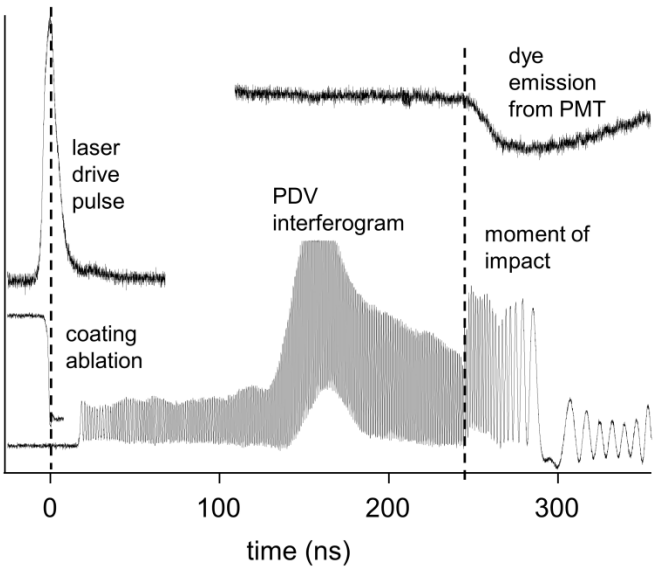

Figure 4.15: Timing diagram used to synchronize PDV and optical detectors. A second-harmonic crystal causing a negligible picosecond delay is inserted into the drive laser beam to generate a signal that can be seen by the PMT and the streak camera (not shown). A sample with a thin mirror is used to reflect the PDV beam back into the signal channel of the interferometer, with the reference beam blocked. A sudden drop in reflectivity denotes the arrival of the drive pulse, which ablates the reflective coating. This reflectivity drop is aligned with the laser drive pulses seen by the PMT and streak camera.

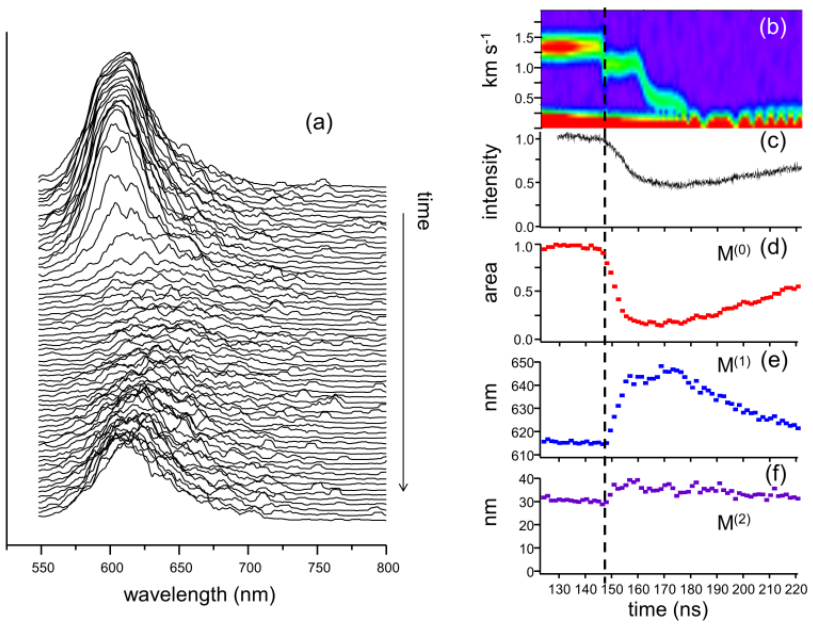

Figure 4.16: Time-dependent emission from R640 dye in PMMA pumped by a quasi-continuous 527 nm laser, subjected to a 1.3 km s^{-1} impact with a 50 μm Al foil that produces 4.8 GPa shock pressure. (a) Streak record. The sudden intensity drop is caused by shock redshift of the absorption away from exciting laser line. (b) PDV velocity history. The impact time is denoted by the dashed vertical line. (c) PMT measurement of wavelength-integrated intensity change. (d) Spectral moment 0 of the streak camera data, denoting instantaneous integrated intensity. (e) Spectral moment 1 denoting instantaneous averaged wavelength. (f) Spectral moment 2 denoting instantaneous spectral width.

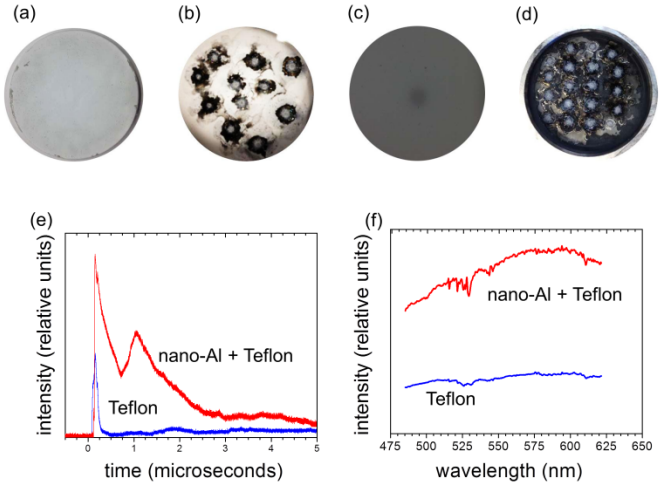

Figure 4.17: (a) Teflon 1 μm particles with 10% polymer binder. (b) Teflon after 3 km s^{-1} impacts. (c) nano-Al + Teflon and 10% polymer binder. (d) Al + Teflon after 3 km s^{-1} impacts. (e) Time-dependent wavelength-integrated emission intensities. (f) Spectra obtained near the emission peaks with a 100 ns time window. Courtesy of Xianxu Zheng.

4.14 References

(1) Trott, W. M. in *High-Pressure Science and Technology -- 1993*, edited by S. C. Schmidt, J. W. Shaner, G. A. Samara and M. Ross (American Institute of Physics, Woodbury, NY, 1993), 1655.

(2) Trott, W. M.; Setchell, R. E.; Farnsworth Jr., A. V. *AIP Conf. Proc.* **2002***, 620*, 1347.

(3) Swift, D. C.; Niemczura, J. G.; Paisley, D. L.; Johnson, R. P.; Luo, S.-N.; Tierney IV, T. E. *Rev. Sci. Instrum.* **2005***, 76*, 093907.

(4) Paisley, D. L.; Luo, S.-N.; Greenfield, S. R.; Koskelo, A. C. *Rev. Sci. Instrum.* **2008***, 79*, 023902.

(5) Bowden, M. D. and Knowles, S. L. in *Optical Technologies for Arming, Safing, Fuzing and Firing V*, edited by Dickey, F. M. and Beyer, R. A. (SPIE, Bellingham, WA, 2009), Vol. 7434, 743403.

(6) Paisley, D. L.; Swift, D. C.; Johnson, R. P.; Kopp, R. A.; Kyrala, G. A. *AIP Conf. Proc.* **2002***, 620*, 1343.

(7) Greenaway, M. W.; Proud, W. G.; Field, J. E.; Goveas, S. G. *Int. J. Impact. Eng.* **2003***, 29*, 317.

(8) Tanaka, K. A.; Hara, M.; Ozaki, N.; Sasatani, Y.; Kondo, K.; Nakano, M.; Nishihara, K.; Takenaka, H.; Yoshida, M.; Mima, K. *Phys. Plasma,* **2000,** *7*, 676.

(9) Walker, F. E. and Walsey, R. J. *Propell. Explos. Pyrotech.* **1976***, 1*, 73.

(10) Andersen, W. H. *Propellants, Explos., Pyrotech.* **1984***, 9*, 39.

(11) Strand, O. T.; Goosman, D. R.; Martinez, C.; Whitworth, T. L.; Kuhlow, W. W. *Rev. Sci. Instrum.* **2006***, 77*, 083108.

(12) Weng, J.; Wang, X. X.; Ma, Y.; Tan, H.; Cai, L.; Li, J.; Liu, C. *Rev. Sci. Instrum.* **2008***, 79*, 113101.

(13) Cogan, S.; Shirman, E.; Haas, Y. *J. Appl. Phys.* **2005***, 97*, 113508.

(14) He, H.; Kobayshi, T.; Sekine, T. *Rev. Sci. Instrum.* **2001***, 72*, 2032.

(15) He, H.; Sekine, T.; Kobayashi, T.; Kimoto, K. *Appl. Opt.* **2001***, 40*, 6327.

(16) He, H.; Sekine, T.; Kobayshi, T. *Appl. Phys. Lett.* **2002***, 81*, 610.

(17) Stahl, D. B. and Paisley, D. L. U.S. patent 5,301,612 (12 Apr 1994).

(18) Cagnoux, J.; Chartagnac, P.; Hereil, P.; Perez, M. *Ann. Phys. Fr.* **1987***, 12*, 451.

(19) Lawrence, R. J. and Trott, W. M. *Int. J. Impact. Eng.* **1993,** *14*, 439.

(20) Siegel, J.; Ettrich, K.; Welsch, E.; Matthias, E. *Appl. Phys. A* **1997***, 64*, 213.

(21) Watson, S. and Field, J. E. *J. Phys. D: Appl. Phys.* **2000***, 33*, 170.

(22) Balazs, L.; Gijbels, R.; Vertes, A. *Anal. Chem.* **1991***, 63*, 314.

(23) Kelly, S. C.; Barron, S.; Thadhani, N. N.; Weihs, T. P. *AIP Conf. Proc.* **2012***, 1426*, 599.

(24) Valenzuela, A. R.; Rodriguez, G.; Clarke, S. A.; Thomas, K. A. *Rev. Sci. Instrum.* **2007***, 78*, 013101.

(25) Fujiwara, H.; Brown, K. E.; Dlott, D. D. *AIP Conf. Proc.* **2010***, 1195*, 1317.

(26) Fujiwara, H.; Brown, K. E.; Dlott, D. D. *AIP Confer. Proc.* **2012***, 1426*, 382.

(27) Ito, K.; Aizawa, T.; Paisley, D. L. *Rev. High Pressure Sci. Technol.* **1998***, 7*, 876.

(28) Fujiwara, H.; Brown, K. E.; Dlott, D. D. *Appl. Opt.* **2010***, 49*, 3723.

(29) Ordal, M. A.; Long, L. L.; Bell, R. J.; Bell, S. E.; Bell, R. R.; Alexander Jr., R. W.; Ward, C. A. *Appl. Opt.* **1983***, 22*, 1099.

(30) Greenaway, M. W.; Proud, W. G.; Field, J. E.; Goveas, S. G. *Rev. Sci. Instrum.* **2002***, 73,* 2185.

(31) Koulikov, S. G. and Dlott, D. D. *J. Imag. Sci. Technol.* **2000***, 44*, 111.

(32) Marsh, S. P. *LASL Shock Hugoniot Data*. (University of California Press, Berkeley, CA, 1980).

(33) Barker, L. M. and Hollenbach, R. E. *J. Appl. Phys.* **1970***, 41*, 4208.

(34) Brown, K. E.; Conner, R.; Fu, Y.; Fujiwara, H.; Dlott, D. D. *AIP Confer. Proc.* **2012***, 1426*, 1593.

(35) Lee, I.-Y. S.; Hill, J. R.; Suzuki, H.; Baer, B. J.; Chronister, E. L.; Dlott, D. D. *J. Chem. Phys.* **1995***, 103*, 8313.

(36) Shen, X. A. and Gupta, Y. M. *J. Appl. Phys.* **1991,** *70*, 7549.

(37) Dlott, D. D. and Fayer, M. D. *J. Chem. Phys.* **1990***, 92*, 3798.

(38) Tokmakoff, A.; Fayer, M. D.; Dlott, D. D. *J. Phys. Chem.* **1993,** *97*, 1901.

(39) Conner, R. W. and Dlott, D. D. *J. Phys. Chem. A* **2010***, 114*, 6731.

(40) Greenaway, M. W.; Gifford, M. J.; Proud, W. G.; Field, J. E.; Goveas, S. G. *AIP Conf. Proc.* **2002***, 620*, 1035.

(41) Peuker, J. M.; Lynch, P; Krier, H.; Glumac, N. *Opt. Lasers. Eng.* **2009***, 47*, 1009.

(42) Carney, J. R.; Miller, J. S.; Gump, J. C.; Pangilinan, G. I. *Rev. Sci. Instrum.* **2006***, 77*, 063103.

(43) Moore, D. S.; Son, S. F.; Asay, B. W. *Propell. Explos. Pyrotech.* **2004***, 29*, 106.

(44) Conner, R. W. and Dlott, D. D. *J. Phys. Chem. C* **2012***, 116*, 2751.

(45) Dolgoborodov, A. Y.; Makhov, M. N.; Kolbanev, I. V.; Streletskii, A. N.; Fortov, V. E. *JETP Lett.* **2005***, 81*, 311.

(46) Parker, L. J.; Ladouceur, H. D.; Russell, T. P. *AIP Conf. Proc.* **2000***, 505*, 941.

(47) Zamkov, M. A.; Conner, R. W.; Dlott, D. D. *J. Phys. Chem. C* **2007***, 111*, 10278.

(48) Osborne, D. T. and Pantoya, M. L. *Combust. Sci. and Tech.* **2007***, 179*, 1467.

(49) Trott, W. M. and Meeks, K. D. *J. Appl. Phys.* **1990**, *67*, 3297.

Chapter 5: Spectroscopy of Shocked Materials

5.1 Introduction

Materials with microstructured inhomogeneities do not necessarily behave under shock compression as their macroscopic parameters, such as particle velocity, U_p, would suggest. Time-resolved emission of embedded nanoprobes can give insight into the local response of shocked mesoscale materials. Nanoprobes, including dyes and quantum dots, can be selectively attached to different constituents of mesoscale materials, such as molecular crystals (*e.g.* RDX), metal particles, or polymer binders (*e.g.* estane).

The idea of using fluorescence of an embedded chemical species to provide insight into the local environment of a shocked material goes back over 20 years. In 1989, Horn and Gupta reported monitoring the fluorescence of Cr^{3+} ions in the Al_2O_3 lattice of a ruby crystal shocked to 10 GPa along the crystal *c* axis.[1] Later, Kobayashi, *et. al.,* reported a similar experiment where the ruby crystal was shocked to beyond its elastic limit, up to 36 GPa.[2] The goals of these studies were specifically to examine the relation between fluorescence shift and states of stress and strain in shocked ruby, as ruby fluorescence is frequently used in hydrostatic experiments as a pressure gauge, and also to explore the possibility of using internal luminescent sensors as probes of the local lattice response to applied shock.

Wishing to expand upon these ideas, I used aggregates of the dye rhodamine 640 (R640, also called rhodamine 101) embedded in a matrix of *poly*(methyl methacrylate) (PMMA) as a model system. The static and shock stress-strain relationship of PMMA is well-established for large blocks, and we were able to measure our own Hugoniot for thin-film PMMA (chapter 4). Shen and Gupta reported on the shock-induced fluorescence shift of a related dye, rhodamine-6G

(R6G) in an ethanol solution up to 2 GPa.[3] They discovered that up to 1.6 GPa, the R6G fluorescence redshifted linearly with pressure, and then slightly blueshifted, attributed to shock-induced intermolecular interactions between the dye and ethanol that resulted in the formation of new polymers. One goal of this experiment was to determine if R6G could be used as an additional pressure sensor in hydrostatic pressure studies, and to the best of my knowledge, R6G nor any other dye have since been used as *in situ* sensors of local environments of solids.

In the following sections, I will describe a series of experiments in which I used embedded R640 dye aggregates in thin layers of PMMA as a model system to demonstrate our ability to simultaneously probe the global and local environments of a solid material when subjected to shock compression up to 15 GPa from laser-driven flyer plates.

5.2 Experimental

Laser-driven flyer plates

The flyer plate targets consisted of quarter-inch-thick glass substrates with 25 or 50 μm aluminum foil (Alufoil) bonded by a clear, low-viscosity UV-curable acrylic adhesive (Dymax Light-Weld 401). Prior to gluing, the foil was rolled out onto a large glass plate to be as smooth as possible. Several drops of the UV adhesive were applied to the center of the foil, and the glass substrate was pressed on top and held in place with clamps. The samples were placed under a UV lamp (Dymax) for 15 minutes, and the excess foil was trimmed off.

A high-power Nd:YAG (Spectra-Physics Quanta-Ray Pro-350) produced 10 ns duration pulses with energies up to 2.5 J. A Faraday Isolator (Electro-Optics Technology, Inc.) was used to prevent harmful back-reflections into the laser, as well as to provide a means of attenuation through its first polarizer when the half waveplate in the laser cavity was rotated. The minimum

energy/pulse obtained with this method was 250 mJ. Further attenuation was reached by use of high-energy dialectric filters. The drive laser pulses were transmitted through a diffractive beam homogenizer (Silios) and a 150 mm focal length aspheric lens to produce top-hat beam profiles 0.7 mm in diameter at the glass/flyer interfaces. The flyer plate substrates and targets were separated by polyimide spacers 125 μm thick and held under vacuum <300 mTorr.

Probe design and alignment.

The experimental schematic detailing the sample and collection optics is shown in Fig. 5.1. The probe consisted of a 10x microscope objective (Nikon LU Plan), a 1000 nm short-pass beamsplitter (Thor Labs) and a 532 nm dichroic beamsplitter (Semrock). The short-pass beamsplitter allowed the 1550 nm laser of the PDV to be reflected, while transmitting the visible wavelengths. The PDV laser was collimated to d=9.5 mm using a commercial fiber collimator from Oz Optics (f=50 mm). The 532 nm beamsplitter reflected the doubled Nd:YLF (527 nm) and transmitted the rest of the visible light. The probe was mounted in a cage system for 1-inch optics on a combination rotation and xyz translation stage.

Proper alignment of the optical probe was crucial to the success of these experiments. The 1550 nm laser needed to be aligned with the probe, and the probe needed to be aligned with the Nd:YAG laser. To align the 1550 nm laser, I removed the 10x objective from the end of the probe and replaced it with an SM1-threaded iris. Because the probe is on a cage system, I screwed on two extra cage rods to provide an extension of the cage. Using a hanging alignment guide affixed with an IR card, I adjusted the 1000 nm short-pass beamsplitter until the laser beam was centered along the entire path of the extra rods. The fiber optic coupler mount was also checked to ensure that the coupler was properly mounted; the coupler was mounted with three

screws and the angle at which the beam left the coupler strongly depended on how those screws were tightened.

To align the probe with the Nd:YAG laser, I used a 633 nm diode alignment laser (Meshtel). Using the same extra alignment rods and a hanging alignment guide, I ensured that the probe was in the correct xy position as well as the correct angle, parallel to the table. The probe was aligned in the z direction by setting the oscilloscope to 100 μs/division and finding the maximum reflection. This corresponded to the reflection off of the aluminum foil. In order to obtain satisfactory interferograms, the 1550 nm laser had to be focused near the impact, so the probe was moved away from the global maximum toward the next local maximum, where the 1550 nm laser was focused on the interior surface of the glass witness plate.

Because the PDV was highly sensitive to misalignment, I first checked that I was obtaining interferograms that clearly showed the launch and impact. Several iterations were often needed. The PDV seemed to be most sensitive to angle/tilt, so once the probe appeared to be properly aligned, if the interferograms were still not satisfactory I would check that the sample was perpendicular to the probe. This was accomplished by placing a fresh flyer plate substrate in the sample holder, and translating the sample from one edge to another and monitoring the intensity of the PDV signal, and adjusting the sample holder as needed so that the intensity remained constant over the sample.

Once the probe was properly aligned, the doubled Nd:YLF was aligned through the probe in a similar fashion, using two hanging alignment guides, a mirror that directed the green light into the probe, and the dichroic beamsplitter within the probe.

Fluorescence Measurements

The target samples consisted of 5 x 5 cm^2 6.35 mm-thick BK7 plates coated with 30-50 μm layers of PVA (5% Airvol 125 in water) and 8 μm layers of 20 mM R640 (Exciton) in PMMA. The aqueous PVA was drop-coated onto the glass substrates and air-dried. R640 and PMMA were dissolved in a solvent composed of methyl-ethyl ketone (50%), n-butyl acetate (15%), cyclohexanone (15%) and 2-pentanone (20%). The R640/PMMA solutions were spin-coated onto PVA/glass at 300 rpm for 2 minutes, and the thicknesses were confirmed by a Dektak profilometer. The PVA layers acted as impedance-matched cushions between the thin R640/PMMA layers and glass plates to prevent the shocks from directly reflecting off of the glass and back into the R640/PMMA layers.

Flyer plate velocity histories, including terminal impact velocity and particle velocities, U_p, were monitored using our PDV system, described in chapter 4. Interferograms were processed *via* moving-window Fourier transforms with 300 MHz filters. R640 was excited by 527 nm pulses from a Q-switched Nd:YLF laser (Quantronix). The pulse durations were 250 ns with ~50 μm beam diameter. The maximum available energy was 5 mJ per pulse; however, the energy was attenuated to less than 1 mJ to avoid excess blue-edge intensity caused by heating the samples.

The optical probe described earlier simultaneously monitored the flyer plate velocity histories *via* PDV and collected the red dye emission, which was directed to a streak camera (Hamamatsu C4334-01) and spectrograph (Oriel), as well as a photomultiplier tube (PMT) (Hamamatsu). Because the 10x objective lens had slightly different focal lengths for 1550 nm and visible light, the probe did not sufficiently collimate the dye emission, so two lenses were placed at the end of the probe. An achromatic lens imaged the dye emission into the

spectrograph/streak camera. The lens was aligned by setting the grating to 0 nm (reflection mode) and the streak camera into focus mode, and translating the lens in the z direction until the steak camera signal was as intense and as uniform as possible.

For the experiments, the streak camera was set to operate mode and the time window was 100 ns. The time resolution was 1.5 ns. The vertical spectrograph entrance slit was 50 μm, the horizontal streak camera photocathode slit was 70 μm, the magnification of the relay optics was unity and the spectrograph magnification was 1.2, so the streak camera observed a 40 x 60 μm^2 region at the center of the impact region.[4]

The Nd:YAG, Nd:YLF and streak camera were all externally triggered by a digital delay generator (DDG) (Stanford Research Systems). The PDV was triggered off of Nd:YAG pulses. Simultaneous detection was possible because PMMA, BK7 and PVA are transparent at the PDV and emission wavelengths. The densities of shocked PMMA were calculated from the Hugoniot for PMMA determined in our lab, using the flyer velocities following impact as the particle velocities U_p. The Rankine-Hugoniot equations used here that relate U_p to pressure, volume and density result from the conservation of mass and momentum across the shock front:

$$\frac{V}{V_0} = \frac{(U_s - U_p)}{U_s} \quad (1)$$

$$P - P_0 = \rho_0 U_s U_p \quad (2)$$

where U_s is the shock velocity, P is pressure, V is volume, ρ is density, and the initial states of the material at rest are indicated by subscript zeros.[5]

The streak camera data necessitated a significant amount of processing. The tilt of the streak camera was determined to be 8 pixels. Prior to further processing or analysis, each streak image file had the background subtracted to correct for the flat-field or "hot" pixels and was tilted. The wavelength was calibrated from matrices of calibration lamp emission (Newport: Ar,

HgNe, Kr), streaked over 2-5 ms. A calibrated blackbody, streaked over 2 ms, combined with grating and photocathode quantum efficiency curves corrected the streak camera/spectrograph detection system for spectral response. Intensity variations for each shot due to different gain settings were also accounted for, by the equation:

$$I = 1 + 2.936E^{-4} * G^{4.634} \quad (3)$$

where I is the corrected intensity and G is the gain setting used (1-16). The data were smoothed in both time and wavelength.

Due to noisy and somewhat ambiguous data, I wrote a Matlab program to calculate the zeroth, first and second moments of the obtained spectra ($M^{(0)}$, $M^{(1)}$ and $M^{(2)}$, respectively):

$$M^{(0)}(t) = \int_0^\infty I(\lambda, t)d\lambda \quad (4a)$$

$$M^{(1)}(t) = \frac{1}{M^{(0)}(t)} \int_0^\infty \lambda I(\lambda, t)d\lambda \quad (4b)$$

$$M^{(2)}(t) = \left[\frac{1}{M^{(0)}(t)} \int_0^\infty \lambda^2 I(\lambda, t)d\lambda\right]^{\frac{1}{2}} \quad (4c)$$

where the spectrum at any time t is defined as $I(\lambda,t)$. The zeroth moment, $M^{(0)}$, is the instantaneous wavelength-integrated area; the first moment, $M^{(1)}$, is approximately the instantaneous average wavelength and gives an estimation of the peak shift, and $M^{(2)}$ is related to the peak width. For a Gaussian, $M^{(1)}$ would be the peak position and $M^{(2)}$ would be the standard deviation, σ, related to the full width at half maximum (FWHM) as $FWHM = 2\sqrt{2\ln 2}\sigma$. The program also subtracts a user-defined baseline and applies limits of integration to prevent non-zero baselines or far-red noise from being included in the analyzed data. The code text is given in Appendix A.

Static Pressure Measurements

A Merrill-Bassett diamond anvil cell (DAC) with Ar hydrostatic pressure medium was used to study the emission of R640-doped PMMA. The DAC and detection system have been described previously.[6,7] The fluorescence was measured with a homemade apparatus, consisting of a coaxial white light video microscope and a 532 nm Raman and fluorescence microscope. A calibrated blackbody corrected the detection system. The fluorescence from ruby chips inside the sample chamber was the pressure calibrant, according to the well-known equation:[8]

$$P = \frac{A}{B}\left[\left(1 + \frac{\Delta\lambda}{\lambda}\right)^{B} - 1\right] \quad (5)$$

where P is the pressure in Mbar, λ is the wavelength of the ruby R1 line, A) 19.04 Mbar, B) 7.665. The pressures were converted into PMMA densities using a relation developed by Flores and Chronister,[9] based on data obtained by Bridgman.[10] The absorbance of R640/PMMA was measured with a UV-Vis spectrometer (Perkin Elmer).

Timing synchronization

The streak camera images and PMT traces were easily overlapped in time by obtaining the times that doubled Nd:YAG pulses arrived at each. A doubler crystal and heat absorbing filter was placed in front of the last lens in the YAG path. The sample was replaced with a lens tissue sandwiched between two glass plates to help scatter the green light. The PDV traces were overlapped with PMT and streak camera data using the ablation of aluminized Mylar. Aluminized Mylar was glued to a glass substrate with the UV-curable glue and placed in the sample holder at the sample position. The reference leg of the PDV was disconnected, and the PDV probe was adjusted for maximum reflection off of the aluminized Mylar. Nd:YAG pulses were incident onto the aluminized Mylar and ablated it, causing a sudden drop in reflectivity and

decreases in PDV signal. The times at which the sudden intensity decrease occurred were overlapped with the times that doubled Nd:YAG pulses arrived at the PMT and streak camera.

The streak camera delays needed to observe flyer plate impacts at each launch power were determined empirically. The doubled Nd:YAG had a consistent delay on the streak camera, so the Nd:YAG delay plus the impact time determined from an interferogram was a good initial estimation.

5.3 Results

Velocity history

Upon impact with the R640/PMMA layers, the flyer plates slowed to U_p and remained at U_p for about 15 ns (50 μm Al flyers) or 8 ns (25 μm Al flyers), then slowed to a stop.

The flyer plates were launched with Nd:YAG pulses between 50 mJ and 1 J. Flyers that were 50 μm thick reached minimum average velocities of 0.5 km/s, with particle velocities near 0.4 km/s and corresponding pressures of 1.6 GPa and densities of 1.4 g/mL. Maximum average velocities, obtained from 25 μm thick flyers, were 3.1 km/s with particle velocities of 2.3 km/s and corresponding pressures and densities of 14.9 GPa and 3.1 g/mL, respectively.

Timing

After adjusting both PMT and PDV traces so that the corresponding doubled Nd:YAG traces and the ablated aluminized Mylar peaks were at “time zero”, the decrease in fluorescence intensity (PMT) began when the flyer plate impacted the R640/PMMA, as shown in Fig. 5.2.

Static fluorescence measurements

The absorbance and emission spectra of R640/PMMA are depicted in Figure 5.3, with an arrow denoting our 527 nm excitation source. Fluorescence spectra of a chip of R640/PMMA

were obtained in a DAC at various pressures up to 10 GPa. Representative spectra are shown in Fig. 5.4. The first and second moments were calculated and were compared to their respective pressures and calculated densities. There was a spectral shift and broadening associated with initial applied pressure (first and second moments, respectively), after which the spectra continued to shift but ceased to broaden significantly with additional pressure.

Shock fluorescence measurements

Figure 5.5 shows two examples of spectra taken from a streak image of shocked R640/PMMA over 100 ns. Figure 5.5a depicts spectra from R640/PMMA shocked with a 50 μm flyer plate launched with 50 mJ, and Fig. 5.5b depicts R640/PMMA fluorescence from a layer shocked with a 50 μm flyer plate launched with 300 mJ. The fluorescence from material shocked with Al launched with higher energy red-shifts more and has a larger intensity decrease. Figure 5.2 depicts the timing of the intensity decrease; as the flyer plate impacted the R640/PMMA layer, the intensity began to decrease, and didn't reach its minimum intensity until the end of the shock duration. Figure 5.6 compares the intensities (PMT), $M^{(0)}$, $M^{(1)}$, and $M^{(2)}$ for the material shocked at three different pressures: 1.5 GPa (Fig. 6a), 4.8 GPa (Fig. 5.6b) and 7.1 GPa (Fig 5.6c). During the shock, the fluorescence intensity and $M^{(0)}$ decreased (Fig. 5.6, first row), and the first and second moments increased. There is a much larger difference in all four parameters between the lowest and middle pressure than there is between the middle and highest pressure; the intensities and widths, $M^{(1)}$ and $M^{(2)}$, only slightly changed between the material shocked with 4.8 and 7.1 GPa.

The average first and second moments of each shock experiment were compared to their calculated global pressures and densities from their particle velocities, U_p, and the PMMA Hugoniot determined in this lab and plotted alongside the static DAC data (Figure 5.7). When

either shock or static pressure was applied, the fluorescence red-shifted and broadened as indicated by the first and second moments. However, in the DAC the first moment continued to increase with applied pressure, and in the shock experiments, the fluorescence stopped shifting after approximately 7 GPa or 1.7 g/mL. In both the static and shocked-compressed R640/PMMA, the second moments initially increased and then tapered off at higher applied pressure.

5.4 Discussion

Absorption and emission wavelengths of solvated dyes are the function of intermolecular potentials and distances between the solvent (here, PMMA) and the solute (R640) molecules. Upon an increase in density from applied pressure, the intermolecular distance decreases, and the polarization of both the solvent and the dye increase. This leads to higher solubility and lower solvent-solute intermolecular potentials and thus a decrease, or red-shift, in emission frequency.[11]

The clearest difference between the emission from the statically compressed R640/PMMA and the shock-compressed material is that the statically compressed material emission continues to red-shift with applied pressure and increased density, and the emission from the shock-compressed material reaches a maximum red-shift around 7 GPa and 1.7 g/mL, as demonstrated by the $M^{(1)}$ data shown in Fig. 5.7. There are three fundamental differences between the static and shock experiments:

1) The static experiments are hydrostatic in nature, while the shock imparts uniaxial stresses.
2) Static compression is isothermal, while shock compression is adiabatic.

3) The statically compressed material had several minutes to equilibrate, while the shock waves only lasted for 8-15 ns.

Of these three, only the last sufficiently explains why the emission of the shock-compressed material did not continue to increase with increased shock pressure.

In the first case, consider the following example: A material that was hydrostatically compressed 30% would essentially be compressed 10% in each dimension. The same material that was uniaxially compressed 30% would be compressed 30% in one direction. In the latter situation, the emission would be expected to red-shift more than in the former.

Because shock compression is adiabatic, the polymer heats up when shocked. This can be seen spectroscopically by an increase in blue-edge emission due to the Franck-Condon principle. Increased temperature causes more, higher energy vibrational states in the first excited electronic state to be available, broadening the fluorescence emission on the higher energy, blue, edge. It is feasible that the emission in the shocked material shifted similarly to the statically compressed material, but that the increased blue intensity canceled out the red-shift, giving the appearance that the fluorescence shift no longer increased with increased pressure. As shown in the bottom row of Fig. 5.7, the second moment, $M^{(2)}$, of the statically compressed material increased with initial pressure (due to inhomogeneous pressure broadening) and stopped increasing with additional pressure. If case (2) were to fully explain our result, we would expect to see greater broadening, or a higher $M^{(2)}$, in the shocked material. However, as evidenced in Fig. 5.7, the $M^{(2)}$ of the emission from the shock-compressed material also appears to reach a maximum with increased pressure.

The deformation of polymers can be described with an energy landscape model.[12,13] Upon slow isothermal compression, as is the case of hydrostatically compressed PMMA, the

ambient landscape gradually evolves into a new, compressed landscape. As compression drives material to states of increased density, the new polymer chain structures reflect changes in the local minima of the compressed, densified state. However, a shock-compressed polymer does not have the time to adjust and reach the maximum density, and its chain structures can instead be thought of as having large amplitude mechanical distortions in the otherwise ambient landscape. Likewise, it has been demonstrated that for similar applied pressure, shock-compressed PMMA reaches a higher volume, lower-density state than hydrostatically compressed PMMA.[14] Because the emission wavelength of a solvated dye is dependent on the density, it is reasonable then that the inability of the R640/PMMA to reach a higher density state explains why the emission shift, characterized by $M^{(1)}$, does not increase after a certain point (7 GPa) with further applied pressure.

5.5 Conclusions

I have demonstrated a rapid throughput technique for simultaneously monitoring the global and local environments of imhomogeneous materials shocked up to 15 GPa with laser driven flyer plates. By using a probe that contained appropriate beamsplitters and collection optics, I was able to monitor the particle velocity, U_p, and time-resolved fluorescence emission spectroscopy of a model system, aggregates of rhodamine 640 in a PMMA matrix. Even in the model system, where the inhomogeneities were on the nanoscale, fluorescence spectroscopy yielded more information about the local environment of the system than the global PDV data gave. The emission peak shift, characterized by the first moment, stopped increasing with increased applied pressure, and the width, characterized by the second moment, also did not shift much following initial applied pressure. These results are different from what would be expected

from the global dynamics alone. This technique can be expanded to examine mesoscale inhomogeneous materials with embedded nanoprobes in each component, such as the crystalline molecular explosive with a polymer binder in a plastic bonded explosive, embedded with different quantum dots.

5.6 Figures

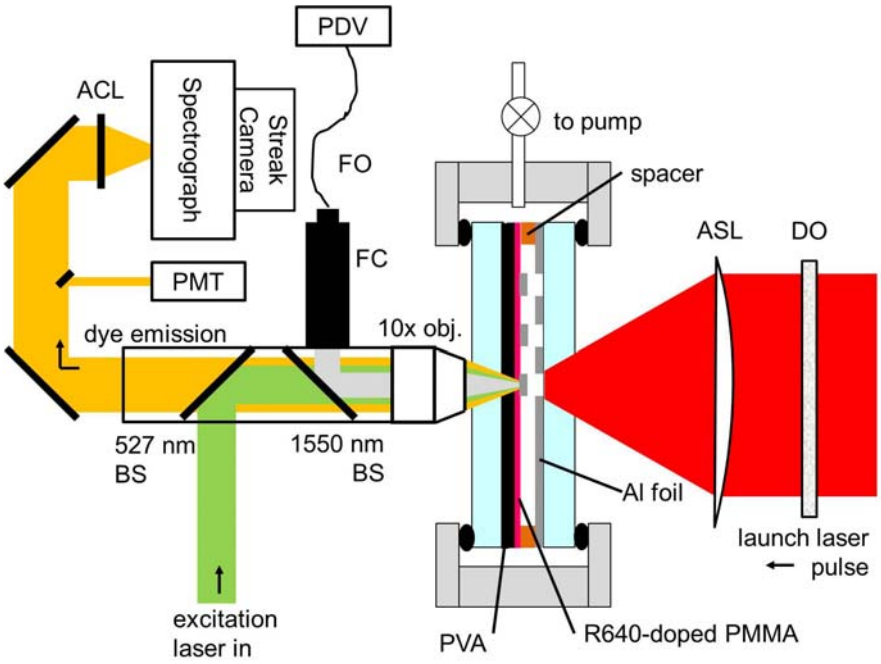

Figure 5.1: Schematic of launch apparatus, sample and collection optics. Key: DO= diffractive optic; ASL= aspheric lens; BS= beamsplitter; FC= fiber collimator; FO= fiber optic; PDV=photon Dopple velocimeter; PMT=photomultiplier tube; ACL= achromatic lens.

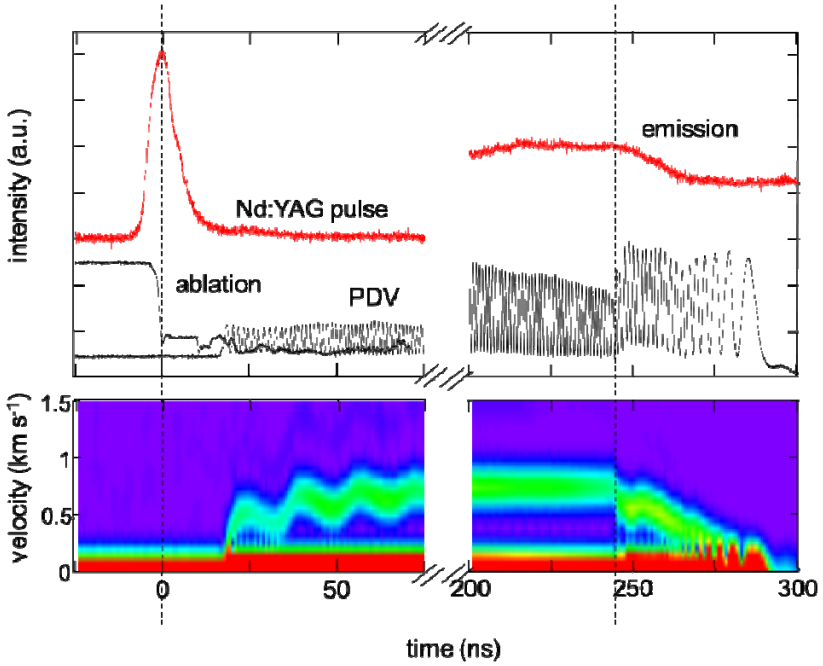

Figure 5.2: Timing diagram used to synchronize PDV and optical detectors. A second-harmonic crystal causing a negligible picosecond delay is inserted into the drive laser beam to generate a signal that can be seen by the PMT (top left) and the streak camera (not shown). Aluminized Mylar, a thin mirror, is used to reflect the PDV beam back into the signal channel of the interferometer, with the reference beam blocked. A sudden drop in reflectivity denotes the arrival of the drive pulse, which ablates the reflective coating. This reflectivity drop is aligned with the laser drive pulses seen by the PMT and streak camera. Fluorescence emission starts decreasing as the flyer plate impacts the R640/PMMA.

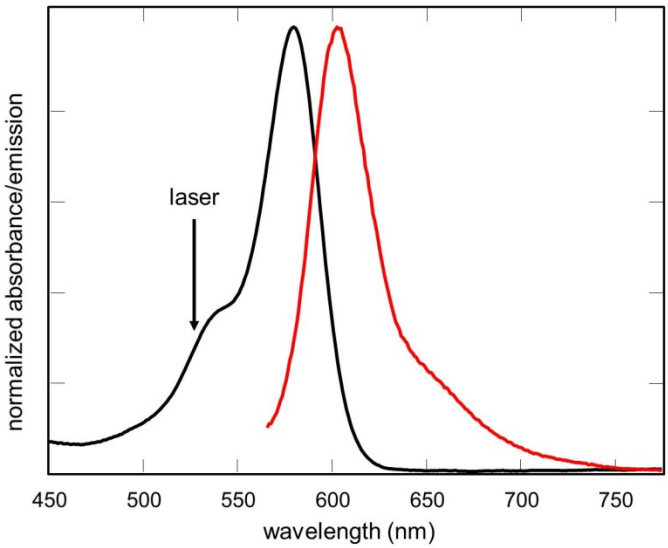

Figure 5.3: Absorbance (left) and emission (right) at atmospheric pressure of R640/PMMA. Arrow denotes excitation wavelength (527 nm).

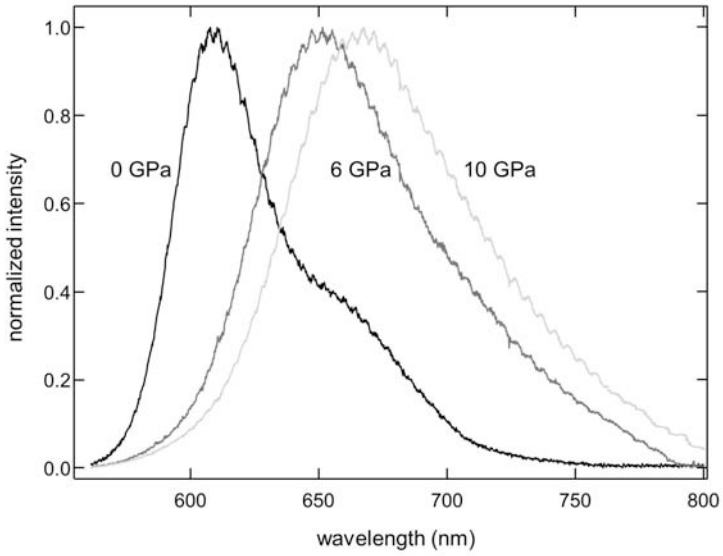

Figure 5.4: Fluorescence of statically compressed R640/PMMA in a DAC at atmospheric pressure (left), 6 GPa (middle) and 10 GPa (right).

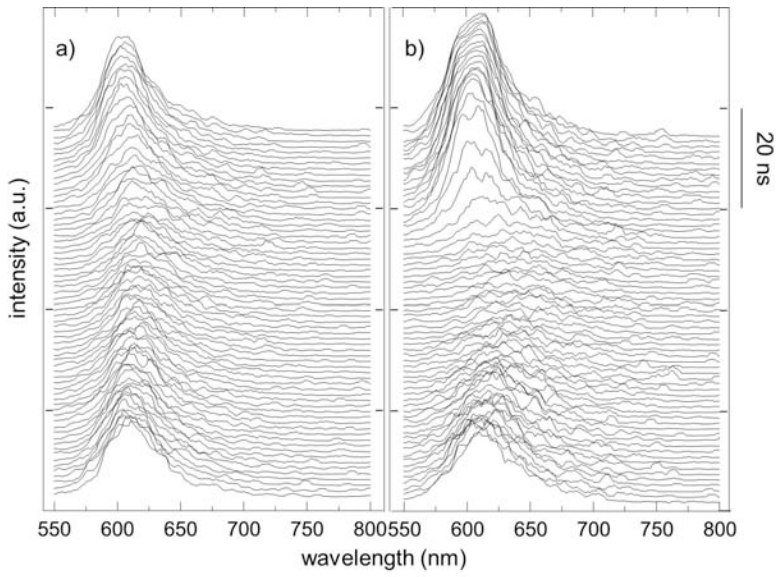

Figure 5.5: Linescans from streak images of R640 emission at two different impact pressures; a) 1.5 GPa (1.37 g/mL) b) 4.8 GPa (1.63 g/mL). Temporal evolution is from top to bottom.

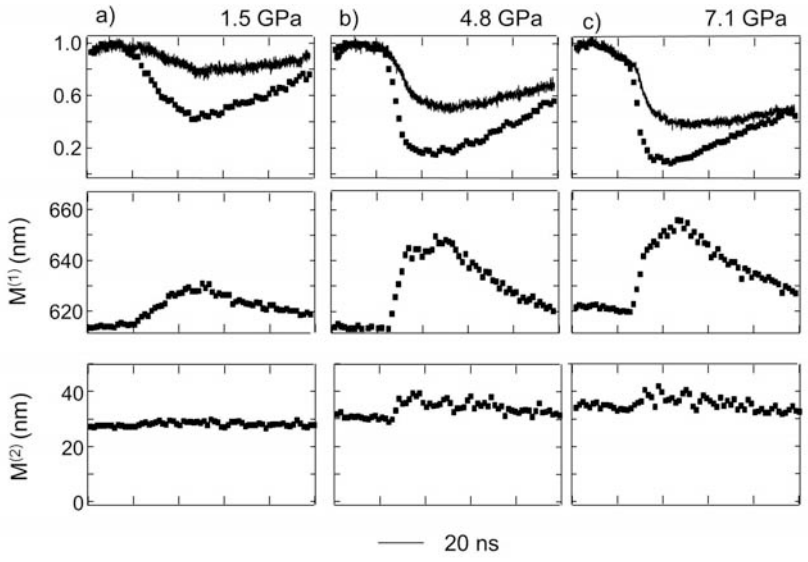

Figure 5.6: Comparison of emission intensity (solid line, top row) and $M^{(0)}$ (dotted line, top row), $M^{(1)}$ (middle row) and $M^{(2)}$ (bottom row) at three different impact pressures: column a) 1.5 GPa; column b) 4.8 GPa; column c) 7.1 GPa. The baselines in column c) are offset from columns a) and b) due to saturation of the streak camera prior to impact. The change in all parameters between low and medium-pressure impacts is much greater than the change between medium and high-pressure impacts.

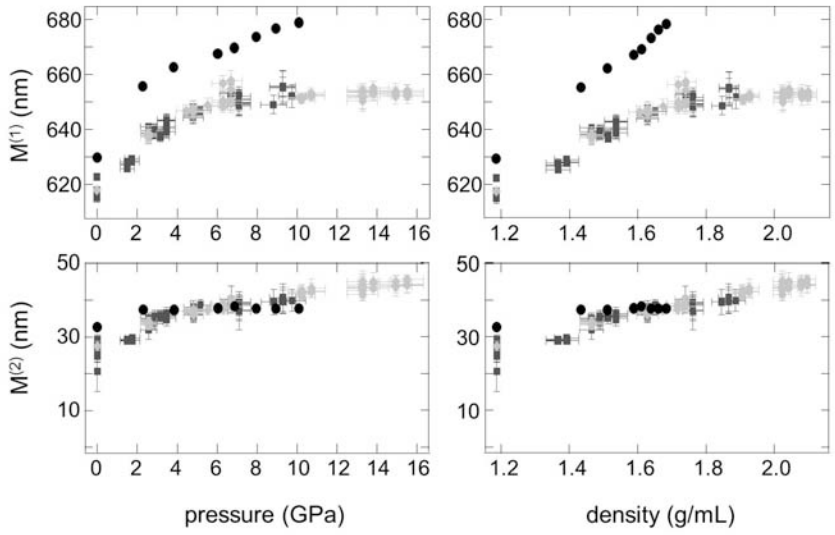

Figure 5.7: $M^{(1)}$ (top row) and $M^{(2)}$ (bottom row) shifts with pressure (left column) and density (right column) for statically compressed R640/PMMA (black dots) and shock compressed R640/PMMA. The dark grey squares denote samples impacted with 50 μm-thick Al flyers and the light grey diamonds denote samples impacted with 25 μm-thick Al flyers. The $M^{(1)}$ shifts of the statically compressed material continue to increase with increased pressure and density, while the spectral shifts of the shocked material levels out.

5.7 References

(1) Horn, P. D. and Gupta, Y. M. *Phys. Rev. B.***1989,** *39,* 973.

(2) Kobayashi, T.; Sekine, T.; Li, X.; Yamashita, Y. *Phys. Rev. B.* **2004,** *69,* 054108.

(3) Shen, X. A. and Gupta, Y. M. *J. Appl. Phys.* **1991,** *70,* 7549.

(4) Conner, R. W. and Dlott, D. D. *J. Phys. Chem. A* **2010**, *114*, 6731.

(5) Marsh, S. P. *LASL Shock Hugoniot Data* (University of California at Berkeley, Berkeley, CA, 1980).

(6) Brown, K. E. and Dlott, D. D. *J. Phys. Chem. C,* **2009,** *113,* 5751-5757.

(7) Fu, Yuanxi; Friedman, Elizabeth A.; Brown, Kathryn E.; Dlott, Dana D. *Chem. Phys. Lett,* **2011,** *501,* 369-374.

(8) Mao, H. K.; Xu, J.; Bell, P. M. *J. Geophys. Res.* **1986**, *91*, 4673.

(9) Flores, J. J.; Chronister, E. L. *J Raman Spectrosc,* **1996,** *27,* 149-153.

(10) Bridgman, P.W. *Proc. Am. Acad. Arts Sci.* **1948,** *76,* 71.

(11) Zhang, B.; Chandrasekhar, M.; Chandrasekhar, H. R. *Appl. Opt.* **1985,** *24,* 2779.

(12) Kim, H.; Hambir, S. A.; Dlott, D. D. *Phys. Rev. Lett.* **1999,** *83,* 5034.

(13) Kim, H.; Hambir, S. A.; Dlott, D. D. *J. Phys. Chem B* **2000,** *104,* 4239.

(14) Gupta, Y. M. *J. Appl. Phys.* **1980,** *51,* 5352.

Chapter 6: Concluding Remarks

In this thesis, I have presented two new techniques for spectroscopically investigating materials under high static or shock pressure. I was the first to utilize surface-enhanced Raman to characterize self-assembled monolayers under static pressure up to 10 GPa, having applications in molecular-level lubrication and as models of energetic materials. In addition, I have devised a method to simultaneously measure the global and local environments of mesoscale inhomogeneous materials shocked to 15 GPa with simplified laser-driven flyer plates. These relatively low-cost and high through-put, simultaneous measurements represent a new way of approaching shock-wave chemistry.

I have laid the groundwork for the spectroscopic study of more materials under high static and shock pressure. In this laboratory, research is being performed and planned to use the shock system to mechanically shock nanoenergetic materials (including aluminum-Teflon and nanothermites) and observe the time-resolved atomic emission and Raman spectra. Additionally, work is currently being performed to characterize solvated quantum dots under pressure. Quantum dots have the benefit over dyes such as R640 in that their spectral widths are much narrower, and so embedding multiple of these sensors in inhomogeneous materials to probe multiple local environments is feasible.

One characteristic of the shocked R640/PMMA that I did not examine in depth was the temperature increase associated with shock compression. Because shock compression is adiabatic, the sample is heated when it is shocked, spectroscopically characterized by a width increase on the blue edge. Beyond the qualitative measurements of the spectral width *via* second moment calculations, quantitative temperature measurements can be made but are quite complicated. Heating a material inside a diamond anvil cell at a known pressure to a known

temperature could provide calibrated P/T spectral widths that could be used as an estimation for shock temperatures. Additionally, the ratios of Stokes and anti-Stokes peaks from SERS of a shocked SAM would provide well-defined shock temperatures.

Appendix A: Data Processing Code

Total dye work-up Matlab program is given here.

```
function [y,b,output]=total_dye(x,y1,lim1,lim2,base1,base2,base3,base4)

% x should be a single column

% y1 should be your corrected and smoothed data in a matrix,
%    where the rows are time and the columns are wavelength

% lim1 is the pixel number where you want to start integration
% lim2 is the pixel number where you want to stop integration
% They are both optional. HOWEVER if you want to use the
%     baseline corrections, you MUST input lim1 and lim2.

% base1-4 are for the baseline corrections.
% For example, if you want your baseline to take into account
%     pixels 1-200 and 500-629,
%     base1=1, base2=200, base3=500, base4=629.
% These are all optional,
%     HOWEVER if you input base1 you must input base2
%     and if you input base3 you must input base4.

% The y output will give you transposed data with every 7 time
%     points chosen

% The b output will give you the same data as y, but with the
%     baseline correction

% "output" will give you the moment information:
% [M0 M1 M2 M2(red) M2(blue)]


%transpose corrected and smoothed data;
%pick out every 7 time points
transposed_data=transpose(y1);
[m,n1]=size(transposed_data);
y=ones(m,floor(n1/7));
for j=1:floor(n1/7)
   y(1:m,j)=transposed_data(1:m,(1+(j-1)*7));
end

%redefine matrix of interest, y
[m,n]=size(y);
```

```
%baseline correction
if ~exist('base1','var')&& ~exist('base2','var')
   b=y;
else
a=mean(y(base1:base2,1:n));

if ~exist('base3','var')&& ~exist('base4','var')
   repA=repmat(a,m,1);
   b=y-repA;


else c=mean(y(base3:base4,1:n));
    d=vertcat(a,c);
    g=mean(d);
    repG=repmat(g,m,1);
    b=y-repG;

end
end
% You can plot the b matrix to see if the baseline is where
%   you want it.
%plot(b);

if ~exist ('lim1','var') && ~exist('lim2','var')
   lim1=1;
   lim2=m;
end

l=(lim2-lim1)+1;

%computes the normalized 0th moment of b with time,
%and puts it in the first column
r=abs(trapz(x(lim1:lim2),b(lim1:lim2,:)));
M0=transpose(r./max(r));
output(:,1)=M0;

%computes the normalized 1st moment of b with time,
%and puts it in the second column
repXo=repmat(x,1,n);
repX=repmat(x(lim1:lim2),1,n);
%x1=repX(:,1); %make as output to check pixels
p=(repX.*b(lim1:lim2,:));
q=abs(trapz(x(lim1:lim2,1),p))./r;
M1=transpose(q);
output(:,2)=M1;
repM1=repmat(q,l,1); %makes M1 the same size as x and b
```

```
repM1ex=repmat(q,m,1); %makes an expanded M1 to be the same size as repXo

%computes the total 2nd moment of b centered around M1,
%and puts it in the third column
s=((repX-repM1).^2).*b(lim1:lim2,:);
u=sqrt(abs(trapz(x(lim1:lim2,1),s))./r);
M2=transpose(u);
output(:,3)=M2;

%computes 'half' of the second moment of b.
% For data where the x axis is reversed, this gives the 'red' side.
% Code may need adjustment for other situations.
f=zeros(1,n);
g=zeros(1,n);
for j=1:n
   f(j)=find(repX(:,j)>repM1(:,j),1,'last');
   g(j)=find(repXo(:,j)>repM1ex(:,j),1,'last');
   %output(j,6)=f(j); %just a check, no useful data
   %output(j,7)=g(j); %just a check, no useful data
   h=((repX(1:f(j),:)-repM1(1:f(j),:)).^2).*b(lim1:g(j),:);
   v=sqrt(abs(trapz(x(lim1:g(j),1),h))./r);
   rM2=transpose(v);
   output(j,4)=rM2(j);

%computes the other 'half' of the 2nd moment of b.
% For data where the x axis is reversed, this gives the 'blue' side.
% Code may need adjustment for other situations.
   h2=((repX((f(j)+1):l,:)-repM1((f(j)+1):l,:)).^2).*b((g(j)+1):lim2,:);
   w=sqrt(abs(trapz(x((g(j)+1):lim2,1),h2))./r);
   bM2=transpose(w);
   output(j,5)=bM2(j);
end
```